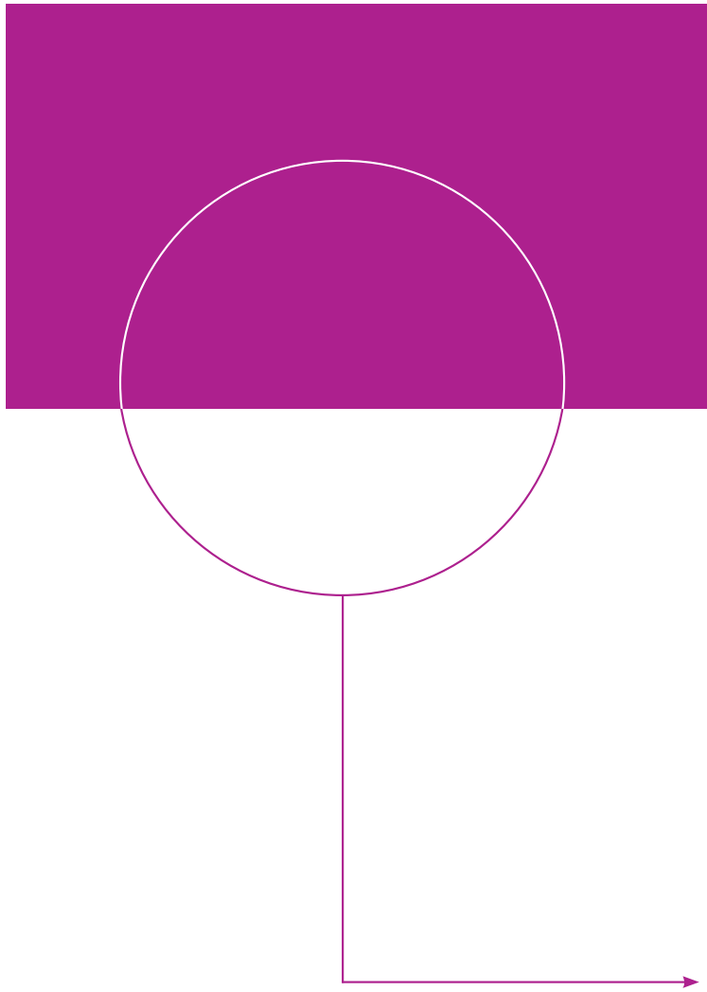

Master's thesis

2021

Morten Fosstveit

NTNU
Norwegian University of
Science and Technology
Faculty of Engineering
Department of Energy and Process Engineering

Master's thesis

Morten Fosstveit

Optimization of hydrogen liquefaction process with mixed refrigerant precooling

June 2021

NTNU
Norwegian University of
Science and Technology

NTNU
Norwegian University of
Science and Technology

NTNU
Norwegian University of
Science and Technology

Optimization of hydrogen liquefaction process with mixed refrigerant precooling

Morten Fosstveit

Master's thesis: Energy and the Environment
Submission date: June 2021
Supervisor: Bjørn Austbø
Co-supervisor: Sayed Ebrahim Hashemi

Norwegian University of Science and Technology
Department of Energy and Process Engineering

Preface

This master's thesis is the final part of the 2 year MSc program, Energy and the Environment at the Department of Energy and Process Engineering, Norwegian University of Science and Technology (NTNU).

The project description was developed in cooperation with the supervisors at NTNU, where the overlaying intention of this master's thesis is to investigate the optimal precooling temperature in a hydrogen liquefaction process.

I would like to express my sincere gratitude to the internal supervisors at NTNU, Professor Bjørn Austbø, and Ph.D. candidate Sayed Ebrahim Hashemi, for their weekly guidance and abundant supply of information.

Trondheim, June 11th 2021

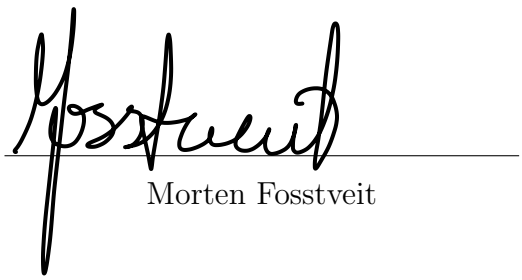

Morten Fosstveit

Abstract

The main objective of this Master thesis is to find an optimal precooling temperature in between 80-120 K for an optimized 100 tdp hydrogen liquefaction process utilizing an MR precooling cycle and to perform an exergy analysis on the optimal configuration in order to assess for improvements in further work.

Optimization of decoupled SMR precooling cycle and a hydrogen Claude cycle has been conducted with a precooling temperature step size of 10 K over the temperature span from 80 K to 120 K. Two configurations of the SMR precooling concept have been optimized that differentiate in the degree of phase separation between high- and low-boilers in order to reduce the refrigerant freeze-out probability.

By analyzing the SEC of the precooling cycle in context to the hydrogen Claude cycle indicates an optimal precooling temperature at 90 K. The SMR cycle configuration utilizing a high degree of phase separation has indicated a reasonably low probability of refrigerant freeze-out, with low efficiency compromise. Optimized result shows an SMR precooling cycle SEC and exergy efficiency of 1.27 kWh/kg_{LH_2} and 42.77%. For the hydrogen Claude cycle, the SEC and exergy efficiency is 5.76 kWh/kg_{LH_2} and 35.62%, respectfully. With a total hydrogen liquefaction SEC and exergy efficiency of 6.52 kWh/kg_{LH_2} and 37.01%, if 100% of the turbine expander work is recovered in the compressors.

Based on analyzing the exergy losses in the 90 K SMR precooling cycles, it has been found that there is minor room for improvements while maintaining a relatively low number of components. However, the SMR cycle configuration with a low degree of phase separation has been found to have slightly improved SEC and exergy efficiency. So, a better prediction of the mixed refrigerant freeze-out estimation is required in order to find the optimum efficiency for a SMR cycle configuration.

80% of the total exergy losses are attributed to the hydrogen Claude cycle. Exergy analysis has indicated that there is room for improvements by rearranging the refrigerant cycle configuration and replacing the throttling valves with a dense phase expander. Small variations in the estimated equilibrium hydrogen estimation model-fitting have indicated to have a significant impact on the efficiency and the exothermic ortho-para conversion.

Sammendrag

Hovedmålet med denne masteroppgaven er å finne en optimal for-kjølingstemperatur mellom 80-120 K for en optimalisert 100 tdp flytende hydrogenprosess ved å bruke MR for-kjølingssyklus, og å utføre en eksergianalyse på den optimale konfigurasjonen for å vurdere for forbedringer i videre arbeid.

Optimalisering av separat SMR-forkjøling og en hydrogen Claude-syklus har blitt utført med en steg-størrelse på 10 K, over temperaturområdet fra 80 K til 120 K. To konfigurasjoner for for-kjølingssyklusen er optimalisert som skilles i forhold til separasjonsgrad mellom komponenter som har høye og lave kokepunkt for å redusere muligheten for frysing av kjølemediet.

Ved å analysere SEC i for-kjølingssyklusen i sammenheng med hydrogen Claude-syklusen indikerer det en optimal forkjølingstemperatur ved 90 K. SMR-sykluskonfigurasjonen som bruker en høy grad av faseseparasjon har indikert en rimelig lav sannsynlighet for frysing av kjølemiddel, med lavt effektivitetskompromiss. Optimalisert resultat viser en SMR for-kjølingssyklus SEC og eksergieffektivitet, henholdsvis på 1,27 kWh/kg_{LH_2} og 42,77 %. For hydrogen-Claude-syklusen er SEC og eksergieffektivitet henholdsvis på 5,76 kWh/kg_{LH_2} og 35,62 %. For den totale kondenserings prosessen viser en SEC og eksergieffektivitet på henholdsvis 6,52 kWh/kg_{LH_2} og 37,01 %, hvis 100 % av turbinarbeidet blir gjenvunnet i kompressorene.

Basert på å analysere eksergitapene i 90 K SMR for-kjølingssyklusene, har det blitt funnet at det er mindre rom for forbedringer mens det opprettholdes et relativt lavt antall komponenter. Imidlertid har SMR-sykluskonfigurasjonen med en lav grad av faseseparasjon blitt funnet å ha litt bedre SEC og eksergieffektivitet. Så det kreves bedre beregning av frysepunktet for blandet kjølemedium for å finne den optimale SMR-sykluskonfigurasjonen.

80 % av de totale eksergitapene tilskrives hydrogen Claude-syklusen. Eksergianalyse har indikert at det er rom for forbedringer ved å omorganisere konfigurasjonen av kjølemediesyklusen og erstatte strupeventilene med en tett faseutvidelse. Små variasjoner i modelltilpasning av den estimerte likevekts hydrogen modellen har indikert å ha en betydelig innvirkning på effektiviteten og den eksoterme ortho-parakonvertering.

Contents

Nomenclature

Ex_{loss}	$[\frac{kJ}{s}]$	Exergy loss
ex	$[\frac{kJ}{kmol}]$	Molar specific exergy
$\bar{e}^0$	$[\frac{kJ}{kmol}]$	Standard chemical exergy
Δex	$[\frac{kJ}{kmol}]$	Molar specific exergy loss
η_{ex}		Exergy efficiency
$\bar{h}$	$[\frac{kJ}{kmol}]$	Molar specific enthalpy
i		Component
$\dot{m}$	$[\frac{kg}{s}]$	Mass flow rate
μ_{JT}	$[\frac{K}{bar}]$	Joule-Thomson coefficient
$\dot{n}$	$[\frac{kmol}{s}]$	Molar flow rate
n_c		Number of compressors
P_0	$[bar]$	Ambient pressure
P_H	$[bar]$	High pressure
P_M	$[bar]$	Medium pressure
P_L	$[bar]$	Lower pressure
$\dot{Q}$	$[kW]$	Heat flow
SEC	$[\frac{kWh}{kg}]$	Specific energy consumption
$\bar{s}$	$[\frac{kJ}{kmolK}]$	Molar specific entropy
tdp	$[\frac{1000kg}{day}]$	Tonnes per day
T_0	$[K]$	Ambient temperature
$\dot{W}$	$[kW]$	Work
x		Molar fraction

Abbreviations

C1	Methane
C2	Ethane
C3	Propane
C4	Butane
C3MR	Propane precooled mixed refrigerant
DMR	Dual mixed refrigerant
EC	European Commission
eH_2	Equilibrium hydrogen
EOS	Equation of state
EU	European Union
GHG	Greenhouse gas
HB	Higher boundaries
HX	Heat exchanger
H_2	Hydrogen
JT	Joule-Thomson
LB	Lower boundaries
LCA	Life cycle assessment
LH_2	Liquid hydrogen
LMTD	Logarithmic mean temperature difference
LNG	Liquid natural gas
MFC	Mixed fluid cascade
MR	Mixed refrigerant
MTA	Minimum temperature approach
N_2	Nitrogen
oH_2	Orthohydrogen
pH_2	Parahydrogen
PL	Pressure level
PR	Pressure ratio
PSO	Particle swarm optimizer
SMR	Single mixed refrigerant
STP	Standard temperature and pressure

List of Figures

List of Tables

Introduction

The following section in this chapter aims to provide the background and motivation for selecting optimization of liquid hydrogen production as a master's thesis subject. Consecutively, the research objectives and the structure of this thesis are presented.

1 Background and motivation

The attention towards hydrogen as an energy carrier is, renewed and in rapid growth, around the world due to hydrogen's possibility to decarbonize industry, transport, and power sectors [1]. A life-cycle assessment (LCA) of future hydrogen decarbonization pathways has been performed by The Hydrogen Council, indicating that the future for hydrogen has great decarbonization potential if derived from renewable energy-assisted water electrolysis, where the highest potential is indicated when energy is supplied from wind- or hydropower [2].

Hydrogen (H_2) has the highest gravimetric energy density of any fuel [3], at 120.0 MJ/kg (LHV) [4]. The high gravimetric energy density could be beneficial for decarbonization purposes, as the utilization of hydrogen does not emit CO_2 [5]. However, 96% of Europe's produced hydrogen is derived from the CO_2 intensive steam methane reforming process, called grey hydrogen [6]. For hydrogen to be more environmentally friendly the reforming process should include carbon capture and storage, called blue hydrogen [2]. Another hydrogen production option is to supply energy harnessed by renewable energy to water electrolysis cells, producing green hydrogen [2]. At standard temperature and pressure (STP), hydrogen has a density of 0.09 kg/m^3, thus is the volumetric energy density low compared to commonly used fossil fuels [4]. By pressurizing (350 or 700 bar) or liquefying hydrogen (LH_2) the volumetric energy density is greatly improved relative to hydrogen at STP, as depicted in figure 1.1. [5] [4]

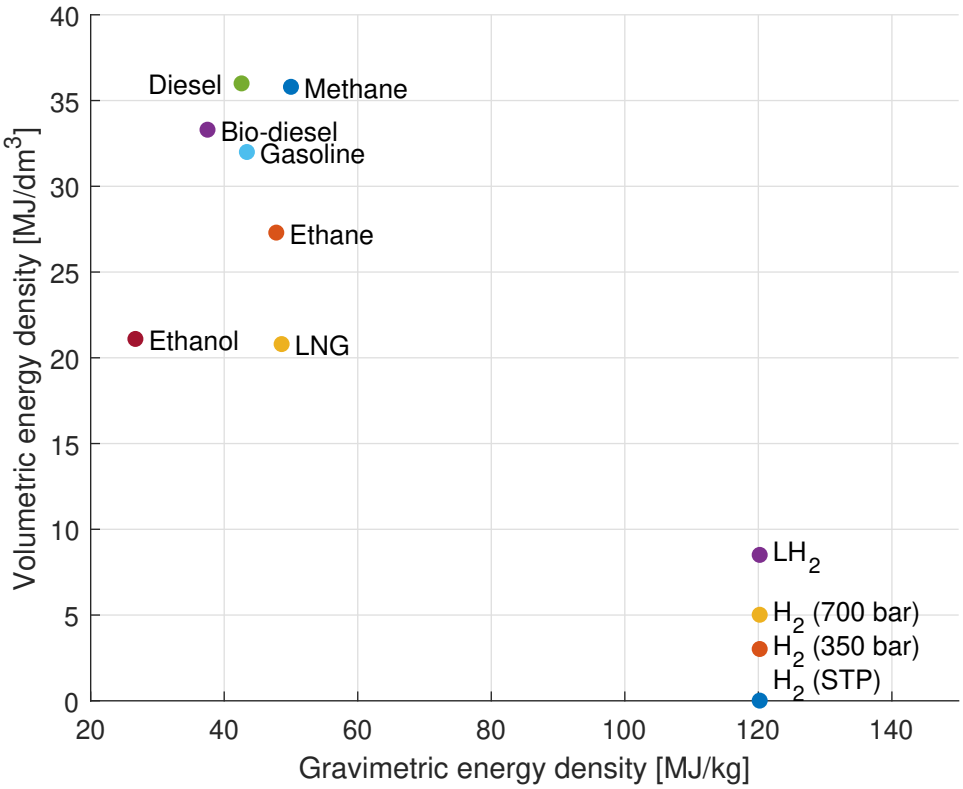

Figure 1.1: *A comparison of the energy densities for different fuels (LHV). [4]*

Hydropower is Norway's main energy source with an installed capacity of 33 003 MW, and new hydro plants emerging every year [7]. Also, Norway has one of the best wind resources available in Europe [8]. As of 2013, only 1% of Norway's energy production originated from wind power [8]. From 2013 to 2020, installed wind power capacity has experienced rapid growth from 1.9 TWh to 9.9 TWh, equating to approximately 6% of Norway's total energy production [9]. The Norwegian science institute SINTEF, is working on the possibility to combine hydrogen production with remotely installed onshore wind energy at Raggovidda in Finnmark [10]. Offshore wind has the potential to bring a new era of wind energy production, due to high wind energy potential in waters deeper than 60 meters [11]. The technical feasibility for offshore wind power has been proven successful with the Hywind project developed by the Norwegian firm, Equinor [11]. The Danish firm Ørsted aims to develop a pilot project in order to produce about 1000 kg of green hydrogen using 2 MW of energy harnessed by offshore wind turbines, production start is aimed at the end of 2021 [12]. ERM, a UK-based consultancy firm has been awarded £3 million in government funding for their Dolphyn project which aims to be "world's first" to establish a design concept for an integrated system producing green hydrogen from offshore wind [13]. As wind power energy share increases, the potential of surplus energy production might become larger due to the intermittent nature of wind. Hydrogen energy

storage could be a good solution to reduce potential surplus energy production from wind power and other renewable energy sources [10].

As of 2018, half of the 330 global hydrogen refueling stations were located in the USA and Japan, with the other half mostly concentrated in Central Europe [14]. The Hydrogen Council has targeted 3000 refueling stations globally by 2025 [14]. The Norwegian hydrogen infrastructure is limited [14]. However, Norled is building the world's first hydrogen ferry which could potentially pave the way for future hydrogen infrastructure in Norway. [14][15] In September 2020, Airbus unveiled their new liquid hydrogen aircraft concepts as a solution to decarbonize the aviation industry, these aircrafts could potentially be in service by 2035 [16].

Norway is a country with large renewable energy potential that could influence the growth of the hydrogen economy [7][9]. However, Norway's geographic location is relatively distant from a well-established hydrogen infrastructure [14], indicating that the economics of transportation is of relative importance. Ishimoto et al. [17] performed a value chain analysis comparing transportation of liquid hydrogen and ammonia as energy carriers to Rotterdam and Japan. They showed that the levelized cost and CO_2 footprint for liquid hydrogen were lower than for ammonia when delivered to Rotterdam, and with optimistic assumptions, the two energy carriers showed equal levelized cost if delivered to Japan[17].

In the the past 50 years of commercialized hydrogen liquefaction plants there has been little improvement [18]. Krasae-in et al. [18] found that every liquid hydrogen production site is based on precooling hydrogen down to 80 K with nitrogen, and from 80 K to approximately 20 K utilizing a hydrogen Claude cycle. They reported that for installed LH_2 plants in the USA, developed by Praxair, Air Products, and Air Liquids, specific energy consumption (SEC) is found to be between 12-15 kWh/kg_{LH_2}. Also, they reported that the best SEC for an LH_2 plant in the USA is at 10 kWh/kg_{LH_2} but the location and developer are unknown [18]. Aasadnia et al.[19] reported SEC and exergy efficiency for Praxair plants ranging between 12.5-15 kWh/kg_{LH_2} and 23.1-19.3%, respectively. And, the German LH_2 plant in Ingolstadt developed by Linde kryotechnik AG, the SEC and exergy efficiency is reported to be between 13-15 kWh/kg_{LH_2} and 22.2-19.3% [19].

For liquid hydrogen to be a viable means to assist the future of decarbonization the efficiency needs to be improved [19]. Several publications has been released over the last years assessing the use of mixed refrigerant (MR) precooling cycle in hydrogen liquefaction processes, which has been in widespread use for liquefaction of natural gas due to its superior efficiencies relative to pure refrigerant cycles [[20],[21],[22],[23]]. A SEC long-term target for hydrogen liquefaction is at

approximately 6.0 kWh/kg$_{LH_2}$ and is predicted to be in reach by utilizing current technologies. [24]

Based on the research Berstad et al. [23] did on a 114 K SMR precooled hydrogen Claude cycle, they suggested to develop a MR precooling cycle which can reach lower precooling temperatures, in order to shift the cooling load from the low exergy efficient hydrogen Claude cycle, towards a more efficient precooling cycle [23]. In response, this thesis will perform optimization of liquid hydrogen production with the overlaying intention to find the optimal precooling temperature in between 80 K-120 K.

1.1 Research objectives

This master's thesis will emphasize modeling of MR precooling cycles, using the hydrogen Claude cycle presented by Berstad et al. [23] in order to create a hydrogen liquefaction process. The main objective of the master's thesis is to find a optimal precooling temperature, for a mixed refrigerant precooled hydrogen Claude cycle. The research objectives are presented below:

- Literature review on LH_2 processes.
- Creating and implementing a thermodynamic model in to Aspen HYSYS to estimate the behavior of equilibrium hydrogen.
- LH_2 process modeling of MR precooling cycles and a hydrogen Claude refrigeration cycle in Aspen HYSYS.
- Optimization of selected process layouts for the LH_2 liquefaction cycle in the range 80-120 K, with the intention of finding the optimal precooling temperature.
- Perform an overall and component-based exergy analysis for the optimal precooling temperature configuration in order to assess the process performance.

1.2 The master's thesis structure

A general overview of the master's thesis structure is presented below.

Introduction: The introduction explains the background of how, and why the subject of optimizing a liquid hydrogen production process was selected for this master's thesis.

Literature Review The Literature review presents the concept of hydrogen liquefaction process. Consecutively, an introduction for the basics related to MR refrigeration/liquefaction concepts and state-of-art research of optimized MR precooled hydrogen liquefaction processes.

Methodology: The methodology chapter presents the method for: creating an estimated thermodynamic model for equilibrium hydrogen; how the hydrogen equilibrium model was implemented into Aspen HYSYS; and a description of how the equilibrium model was validated. In addition the chapter includes: the methodology for obtaining the MR precooling cycle's configurations; an explanation of the different refrigeration/liquefaction cycles; how the processes were optimized; and a short presentation of the exergy analysis equations utilized.

Results & Discussion: In this chapter, the optimized results for the SMR precooling- and hydrogen Claude cycle will be presented and discussed. Consecutively, an exergy analysis for the optimal precooling temperature will be presented and discussed which will serve as the basis for the conclusion, and indicate possible improvements for further work. Lastly, a brief sensitivity analysis of the equilibrium hydrogen model-fitting will be discussed.

Conclusion: Here the final conclusion will be presented along with the proposal for further work.

Literature Review

This chapter will present the concept and theory for the hydrogen liquefaction process, and present different MR refrigeration concepts. Lastly, state-of-art hydrogen liquefaction processes is presented.

2 Hydrogen liquefaction

The concept of hydrogen liquefaction is depicted in figure 2.1 and can be divided into four individual steps as suggested by Walnum et al. [25]:

- Pre-compression
- Precooling
- Cryogenic cooling
- Liquefaction

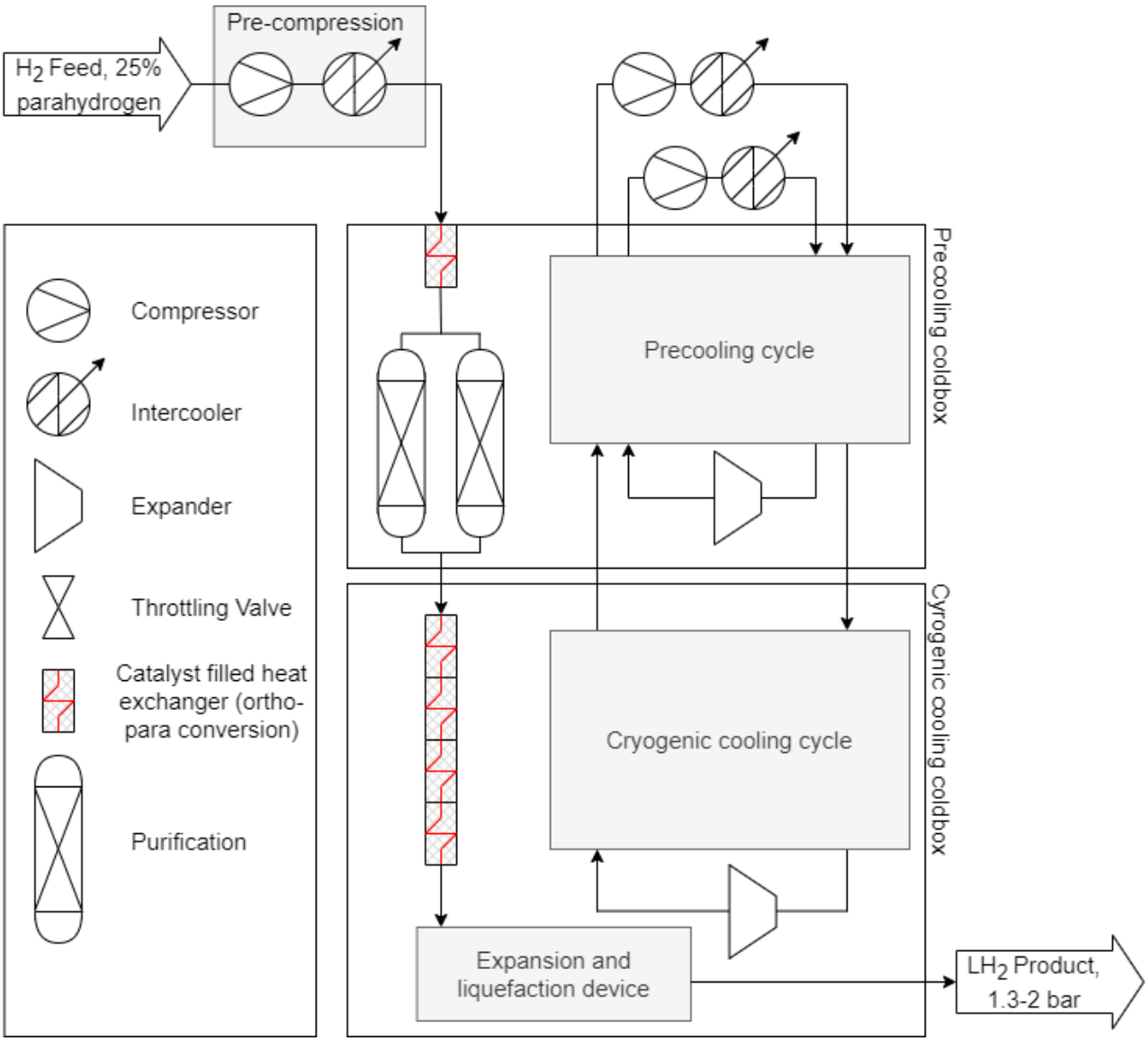

Figure 2.1: *A flowsheet of a hydrogen liquefaction concept. [25]*

2.1 Pre-compression

Pre-compressed hydrogen feed requires less refrigerant compressor work compared at STP [25]. Hydrogen feed at 20 bar requires approximately 35% less refrigerant exergy input than at STP [25]. There is a pressure limit for heat exchangers which has been found to have an upper limit to 75 bar [26]. Also, hydrogen compression is difficult and energy-intensive due to the low molecular weight of hydrogen, and the maximum compression ratio for turbomachinery is found to be limited to 1.2, suggesting a large number of compressors are required to achieve

high hydrogen feed pressure [25]. Normally, hydrogen compression utilizes piston or screw compressors which do not have the same limitation, however, they are usually less energy efficient compared to turbo compressors [25].

2.2 Precooling

The most common precooling process utilized in established hydrogen liquefaction plants is liquid nitrogen vaporization which is often supplied by an on-site air separation unit, cooling the hydrogen feed from ambient temperature to about 80 K [18]. The production capacity of the established liquefaction processes is found to be between 0.3-34 tpd [18]. In order to increase liquid hydrogen production capacity new concepts for precooling are required, due to the limitation of liquid nitrogen supplied by an air separation process [18]. Several conceptualized studies have been conducted in order to increase the efficiency of hydrogen liquefaction by adopting refrigerant cycles commonly used for liquid natural gas (LNG) processes [23]. The majority of the processes obtained in the literature, which is presented later in this thesis, have been based on the single mixed refrigerant (SMR) cycles. MR cycles are generally more efficient than pure refrigerant cycles, however, the precooling temperature required for hydrogen is usually lower than in natural gas liquefaction, hence new challenges arises [25]. One of the challenges related to adopting MR cycles for precooling hydrogen to approximately 80 K is to find an optimal refrigerant-mixture and -cycle which do not possess the risk of refrigerant freeze-out which can result in clogging the refrigerant cycle [25]. Berstad et al. [23] suggested to replace the SMR cycle with a dual mixed refrigerant (DMR) or auto cascade refrigeration cycle, in order to achieve lower precooling temperatures with high efficiency and to limit the risk of refrigerant freeze out [23]. [25]

2.3 Cryocooling

Equilibrium Hydrogen has a variable heat capacity in the cryogenic region for, as is depicted in figure 2.2 [27]. One of the challenging parts of hydrogen liquefaction is to achieve a close temperature match of the different streams within the heat exchangers [25]. The temperature match can be improved by, increasing the hydrogen feed pressure, or using overlapping expander stages to adjust the refrigeration duty at different temperature levels [25].

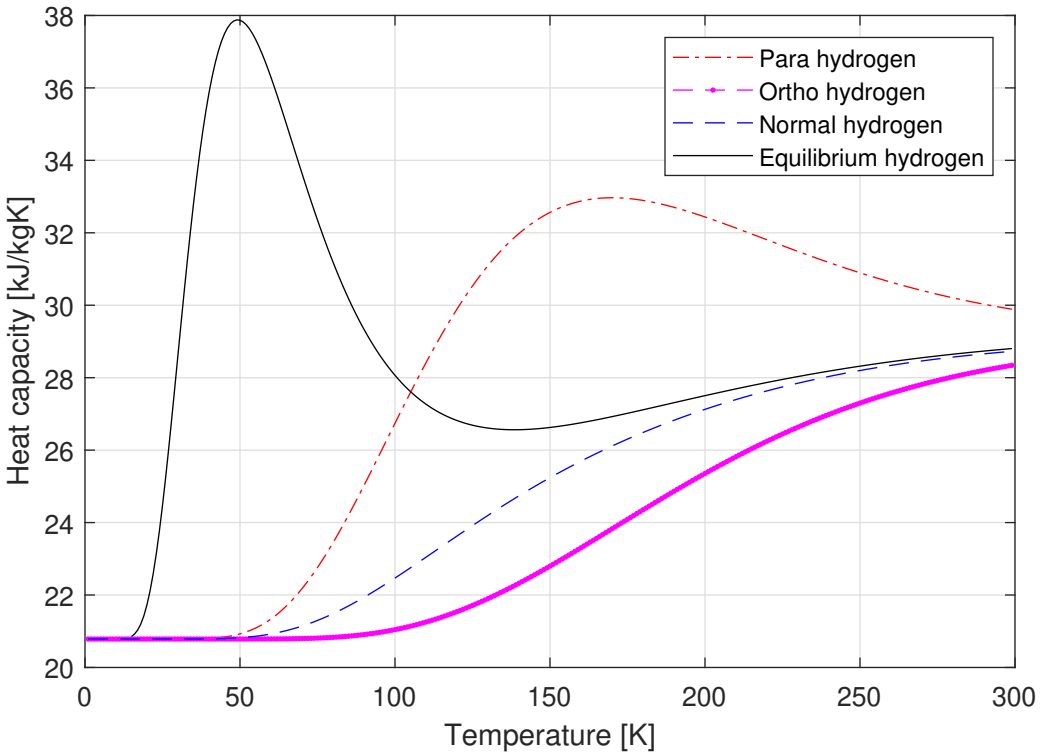

Figure 2.2: *The ideal heat capacity for the different hydrogen quantum states. [27]*

2.4 Liquefaction

The hydrogen liquefaction stage is commonly done by throttling the high-pressure hydrogen feed down to storage pressure [25]. The low-pressure two-phased hydrogen feed is then fully saturate within the last heat exchanger before entering the storage tank at a pressure between 1.3-2 bar [25]. Hydrogen has two quantum states called orthohydrogen (oH_2) and parahydrogen (pH_2), which is defined based on the direction of the proton spin [28]. For orthohydrogen, the atoms spin in the parallel direction and are at a higher energy level than parahydrogen, where the atoms spin in an anti-parallel direction, as depicted in figure 2.3. At room temperature, the concentration of parahydrogen is approximately 25% and 75% orthohydrogen, and is defined as normal hydrogen. [28]

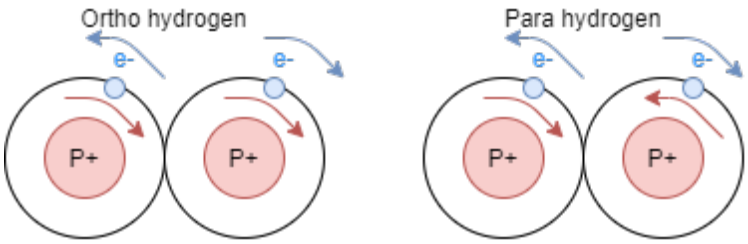

Figure 2.3: *Spin configuration for ortho- and parahydrogen [28].*

As gaseous hydrogen is cooled from 298 K, the concentration of parahydrogen increases, but the spontaneous conversion rate is slow [29]. Unlike gaseous hydrogen, the spontaneous ortho-para conversion of liquid hydrogen is greatly improved, this can cause vaporization of the liquid hydrogen due to the exothermic process of ortho-para conversion [29]. In order to increase the gaseous conversion rate, heat exchangers are commonly filled with a catalyst so that the hydrogen reaches an equilibrium state of ortho- and parahydrogen content at temperature T, denoted equilibrium hydrogen (eH_2) [29]. The latent heat between liquid and vapor of normal hydrogen is approximately 454 kJ/kg_{H_2}, which is less than the exothermic heat released by the ortho-para conversion throughout the liquefaction process, at approximately 527 kJ/kg_{H_2} [30]. In order to minimize boil-off gases, the parahydrogen content should be $> 98\%$ before it enters the liquid hydrogen storage tank [25]. The estimated ortho- and parahydrogen concentration at temperature T is presented in figure 2.4.

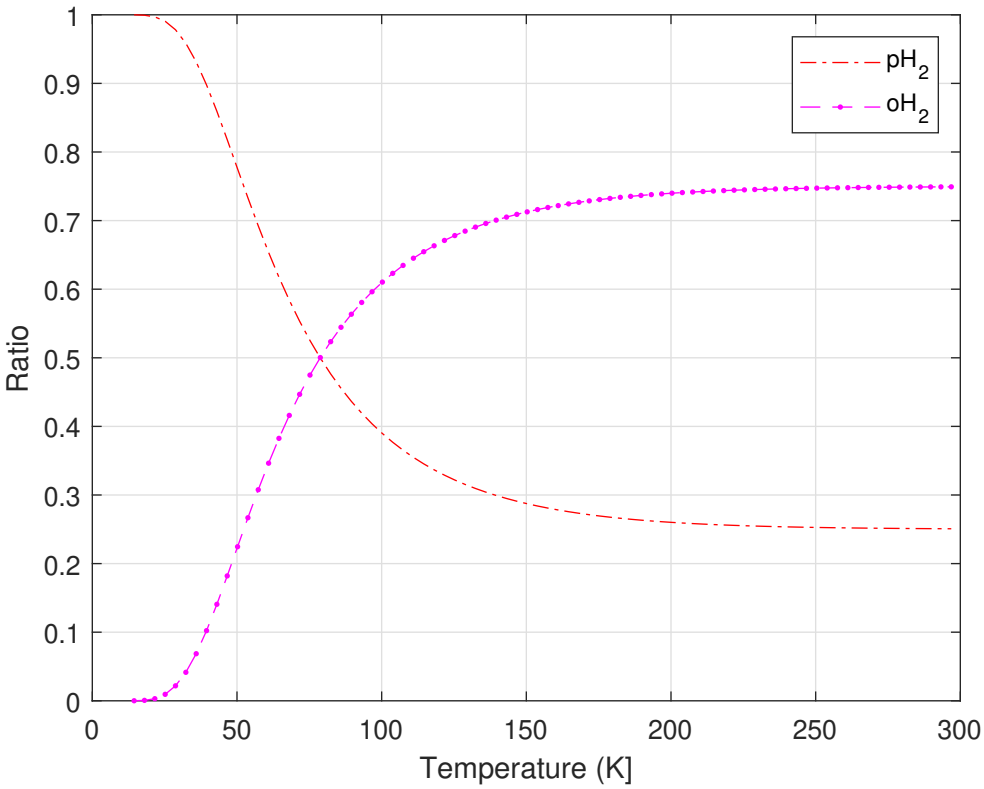

Figure 2.4: *The estimated ortho- and parahydrogen concentration at different temperature. Calculated with equation 4.4 and 4.5 in the methodology section.*

There are various solids that are used as catalysts for the ortho-parahydrogen conversion, such as ferric oxides; chromium; copper; and silver [29]. The conversion reaction is mostly related to the magnetic properties of a material, as the conversion occurs in the presence of an external inhomogeneous magnetic field [29]. The conversion reaction is induced by the Fermi contact interaction and magnetic dipole interaction [29].

3 Refrigeration

The working principle of a gas cooling- and liquefaction-cycle is to reject heat ($\dot{Q}$) from the product ($\dot{n}_1$) to a working fluid (refrigerant) circulating within a refrigeration cycle [31]. Consecutively, the refrigerant is compressed and cooled, rejecting heat ($-\dot{Q}_o$) to the ambient temperature (T_o) before it is expanded, completing the cycle with a sufficiently low-temperature refrigerant entering the heat exchanger. [31] The process described is depicted on the left-hand side of figure 3.1, the figure on the right-hand side is equivalent to a real life process.

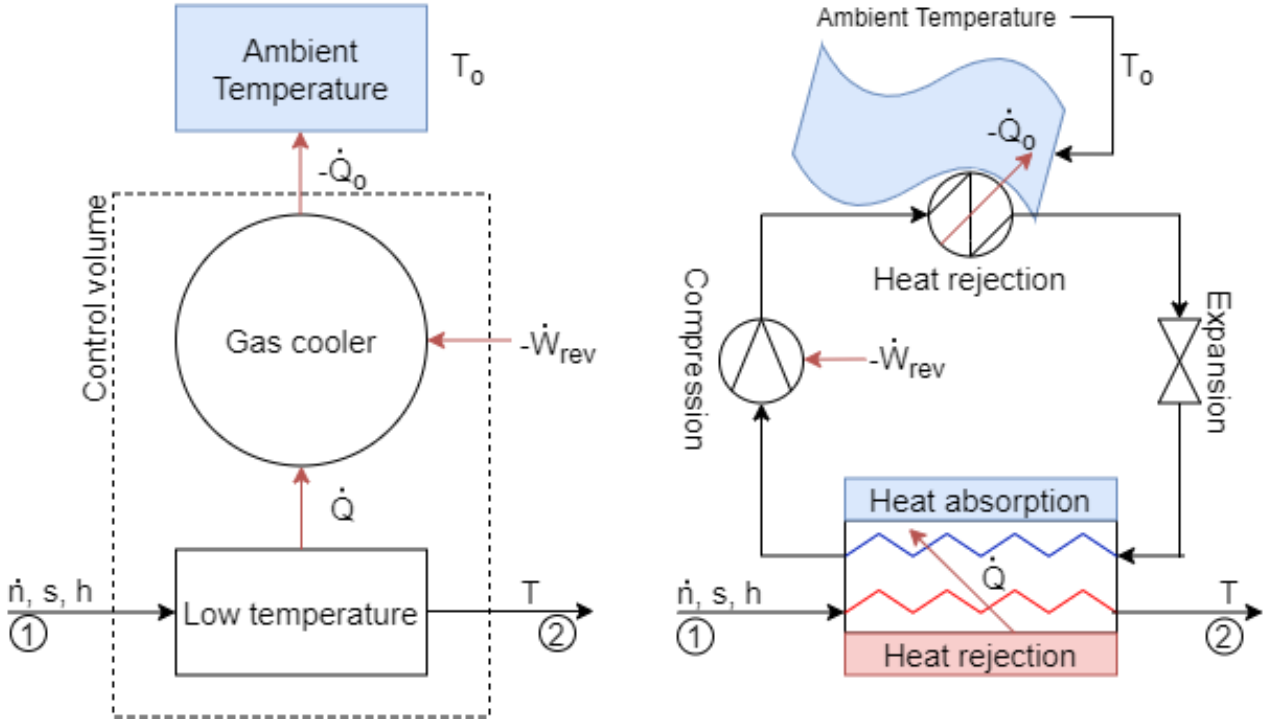

Figure 3.1: *The working principle of gas cooling/liquefaction. [31]*

By applying the first (equation 3.1) and second (equation 3.2) law of thermodynamics to the control volume in figure 3.1, substituting equation 3.2 into equation 3.1 results in equation 3.3 [31]. This defines the amount of reversible work (W_{rev}) obtained by the product stream ($\dot{n}_2$) relative to stream 1. This is also often denoted as minimum or ideal work. [31]

$$\dot{W}_{rev} = \dot{Q} + \dot{Q}_o = \dot{n}(h_1 - h_2) + \dot{Q}_o \tag{3.1}$$

$$\dot{n}(s_1 - s_2) + \frac{\dot{Q}_o}{T_o} = 0 \tag{3.2}$$

$$\dot{W}_{rev} = \dot{n}[(h_1 - h_2) - T_0(s_1 - s_2)] \tag{3.3}$$

$\dot{n}$ = Molar flow $[\frac{kmol}{s}]$
h = Molar specific enthalpy $[\frac{kJ}{kmol}]$
s = Molar specific entropy $[\frac{kJ}{kmolK}]$
$\dot{W}$ = Work input $[kW]$
$\dot{Q}$ = Heat flow $[kW]$

3.1 Exergy

The maximum reversible work obtainable in a gas and liquid is denoted exergy and is the difference between the useful energy of the product relative to the ambient temperature and pressure, also called the dead state (state o) [31]. The specific exergy is described by equation 3.4 [31].

$$ex_{tm} = \frac{\dot{W}_{rev}}{\dot{n}} = (h - h_0) - T_0(s - s_0) \tag{3.4}$$

ex_{tm} = Thermomechanical exergy $[\frac{kJ}{kmol}]$

For systems where the chemical composition changes, chemical exergy must be taken into consideration in order to obtain the correct exergy balance [23]. This is the case for MR systems utilizing mixers and separators [23]. The chemical exergy is calculated with equation 3.5. [23]

$$ex_{ch} = \sum_i x_i \bar{e}_i^0 + \left(\bar{h}_0 - \sum_i x_i \bar{h}_{0,i} - T_0\left(\bar{s}_0 - \sum_i x_i \bar{s}_{0,i}\right)\right) \tag{3.5}$$

ex_{ch} = Specific chemical exergy $[\frac{kJ}{kmol}]$
x = Molar fraction
$\bar{e}^0$ = Standard chemical exergy $[\frac{kJ}{kmol}]$
i = Refrigerant component

Applying equation 3.6 reveals the exergy losses over the system boundaries, exergy loss is also commonly denoted as irreversibility. [31]

$$Ex_{loss} = \sum_{in} \dot{n}(ex_{tm} + ex_{ch}) - \sum_{out} \dot{n}(ex_{tm} + ex_{ch}) + \sum(-\dot{W}) + \sum \dot{Q}\left(1 - \frac{T_0}{T}\right) \tag{3.6}$$

Ex_{loss} = Exergy loss $[kW]$

The exergy efficiency of system boundaries with work interaction such as a gas cooler and liquefier, compressor, and turbines, exergy efficiency can be calculated with equation 3.7. [31]

$$\eta_{ex} = \frac{\text{minimum power required by a reversible system}}{\text{actual power supplied}} \tag{3.7}$$

3.2 Refrigeration cycles

There are several basic refrigeration cycles used in LNG and bio-methane liquefaction, which is reported by Capra et al. [32]. Reverse-Brayton and -Rankine cycle, Linde cycle, open- and closed-Claude cycle, and cryogenic liquid vaporization. The main difference between these cycles is how they produce the cooling duty. The reverse Brayton cycle produces the cooling effect by expanding gas through a turbine without condensation. Joule-Thomson (JT) throttling (Rankine and Linde cycle) is an isenthalpic expansion process, these are often used where the refrigerant is expanded into the two-phase region, and for low production capacities, due to simple design and lower cost. However, the Rankine cycle is also arranged into a cascade system such as propane precooled mixed refrigerant (C3MR) and dual mixed refrigerant (DMR) cycles for large LNG plants. The Claude cycle produces the cooling effect by partially expanding the refrigerant flow in an expansion turbine and throttling valve. Claude cycle is usually adopted for large-scale production due to high capital cost and complexity. Cryogenic liquid evaporation provides the cooling duty from the cryogenic liquid which is often supplied from an air separation unit in the proximity of the liquefaction process. The basic layout of some BM cycles is depicted in figure 3.2. [32]

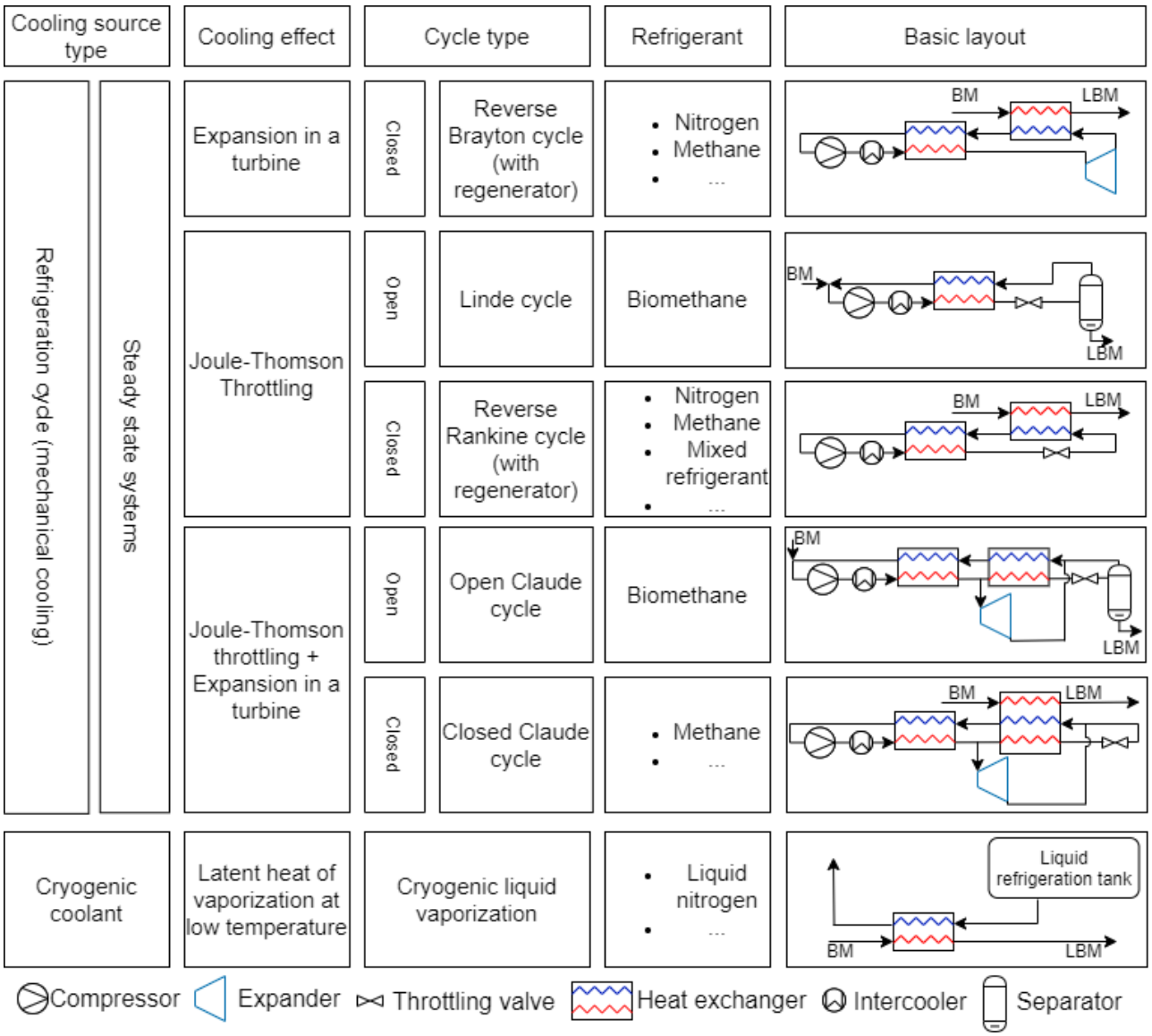

Figure 3.2: *The basic layout for different refrigeration cycles, where bio-methane has been used as a reference product. [32]*

This thesis will focus on the MR reverse Rankine cycle to precool hydrogen prior to the cryogenic refrigeration cycle. There are several MR refrigeration cycles utilized for LNG processes e.g. SMR, and MFC such as C3MR and DMR [33] [34].

3.2.1 SMR

The SMR cycle is a process consisting of a single closed loop mixed refrigerant cycle. Examples of the SMR cycles is the Kleemenko- and PRICO-process [31]. Kleemenko was the

first to suggest utilizing a refrigerant mixture to liquefy natural gas. This process can use one phase separator or more at the consecutive temperature levels in order to reduce the amount of high boilers reaching low temperatures, thereby reducing the risk of refrigerant freeze-out. A simple Kleemenko process is illustrated in figure 3.3 [31].

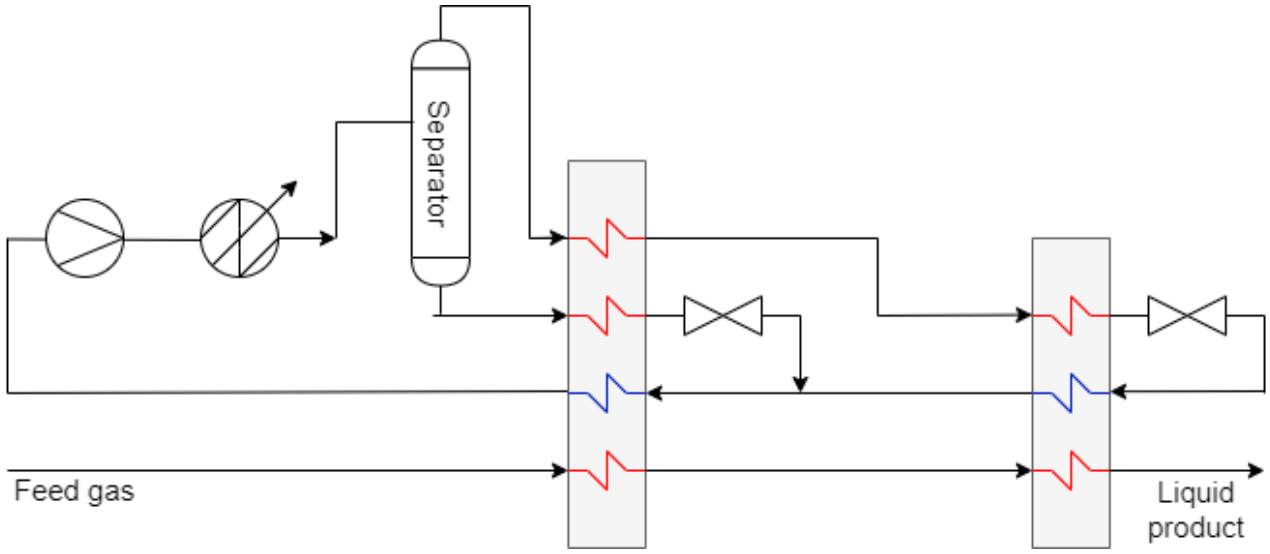

Figure 3.3: *A simplified flowsheet of a Kleemenko refrigeration cycle, with one phase separator.[31]*

The PRICO process is a simple MR cycle and was developed by Black & Veatch [35]. The PRICO process is popular for peak-shaving, due to: rapid startup, reliability, and flexibility. Also, it has the advantages: to be a proven process, simple operation, consisting of a relatively low number of equipment, and has low capital- and operational-cost. A flowsheet of the basic PRICO process can be seen in figure 3.4. [35]

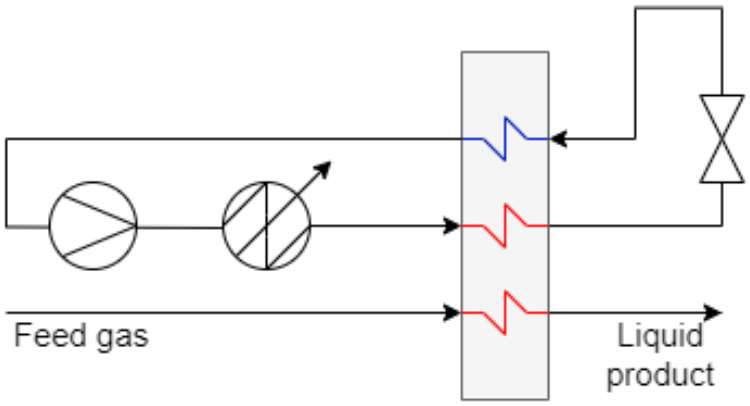

Figure 3.4: *A simplified flowsheet of the PRICO refrigeration cycle.[36]*

3.2.2 MFC

Unlike SMR, the mixed fluid cascade (MFC) consists of two or more closed-loop refrigeration cycles, such as the C3MR and dual DMR cycles [37] [31]. C3MR and DMR cycles dominate the commercialized mid-scale baseload LNG plants. As of 2014, the C3MR process had a market share of about 80% for LNG liquefaction processes. C3MR process is licensed by Air Products and Chemical Inc. (APCI), and the DMR process is patented by Shell. The C3MR and DMR processes are composed of two closed-loop refrigeration cycles, as illustrated in figure 3.5. By definition, they can be divided into a precooling cycle and a subcooling cycle, where the subcooling cycle consisting of a process similar to SMR. The main difference between C3MR and DMR is the refrigerant component(s). The C3MR uses pure propane (C3) refrigerant in the precooling cycle, whereas the DMR generally utilizes a refrigerant mixture that is less volatile relative to the mixture in the subcooling cycle. Generally, an efficient C3MR process consists of more equipment relative to the DMR cycle, due to the need of several pressure and temperature levels in order to better match the heat exchanger composite curves. [37] [31]

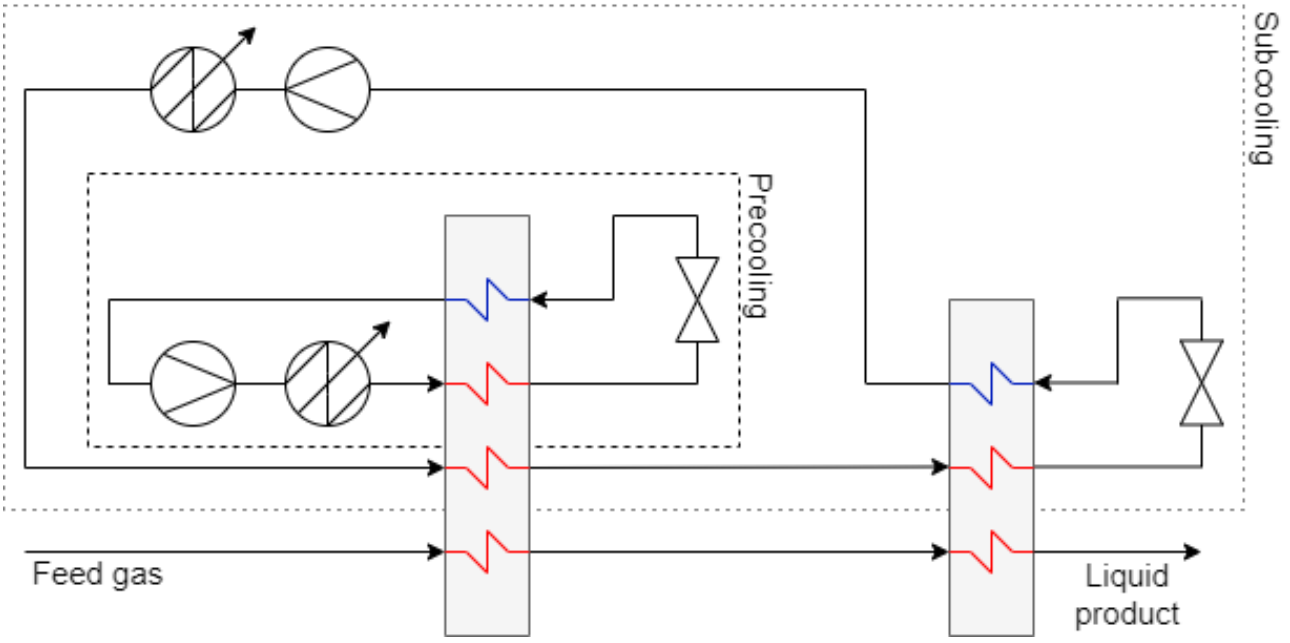

Figure 3.5: *A simplified flowsheet of a two closed loop (MFC) refrigeration cycle. [37]*

3.3 Refrigerant

The refrigerant components used in MR LNG cycles often consist of nitrogen (N_2) and the lightest hydrocarbons: methane (C1), ethane (C2), propane (C3), butane (C4), etc [38]. By using a refrigerant mixture, the working fluid experience a gliding temperature profile throughout the heat absorption, compared to a pure refrigerant, which has a distinct difference between the isothermal latent heat and non-isothermal sensible heat. This effect is illustrated in figure 3.6. Closely matched composite curves can be achieved with the correct refrigerant composition, resulting in reduced irreversibilities within the heat exchangers. [38]

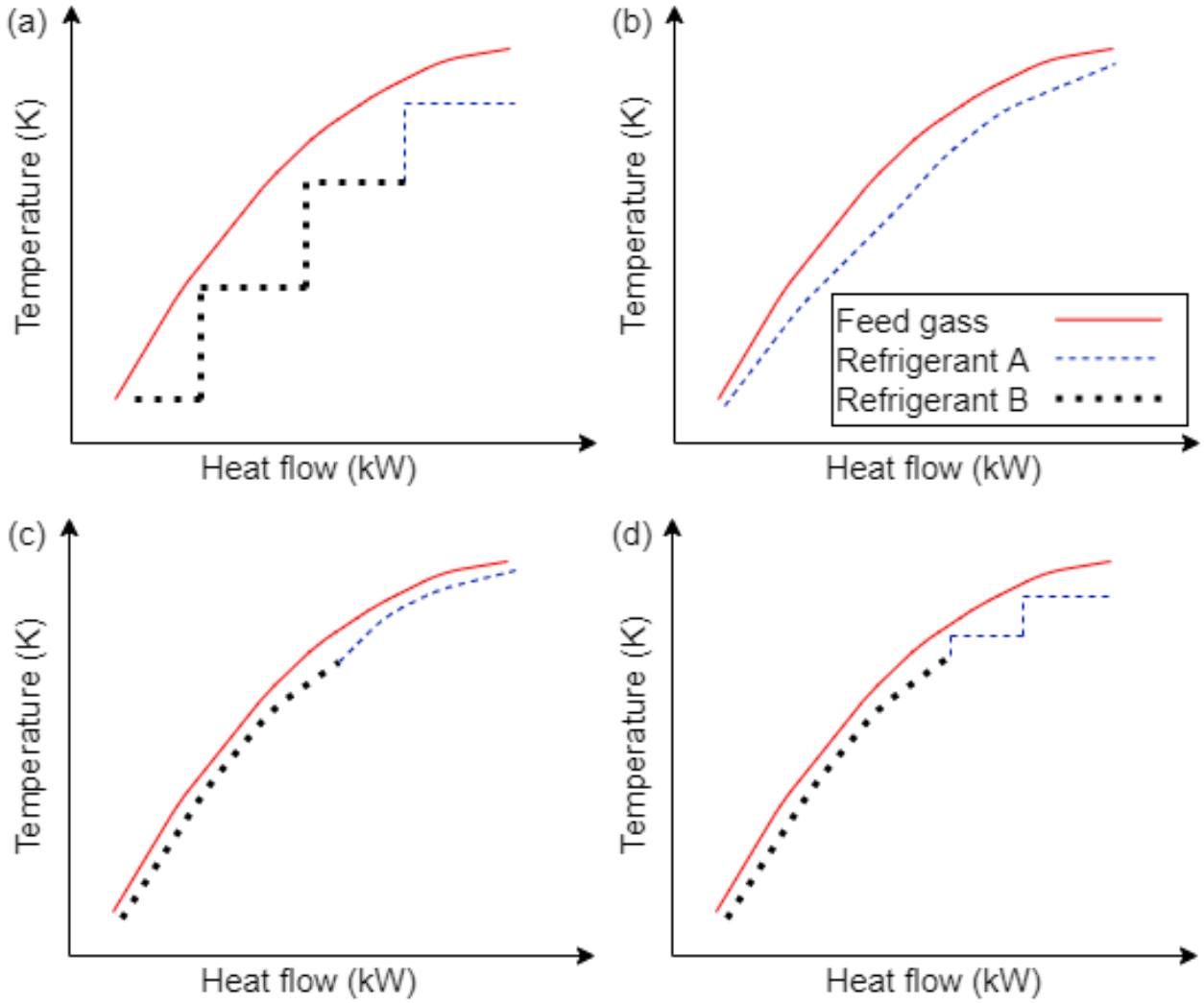

Figure 3.6: *Typical heat exchanger composite curves for: (a) pure fluid cascade; (b) SMR; (c) DMR; (d) C3MR. [38]*

Optimization of the refrigerant mixture is crucial in order to match the heat capacities

between high- and low-pressure streams within the heat exchangers [39]. An advanced MR cycle is the standard cycle for most of the base-load LNG plants, and can achieve an exergy efficiency of approximately 50%. MR cycles that contains additional neon and helium in the refrigerant mixture usually shows low efficiency above 80 K due to their negative JT coefficient at ambient temperature. [39] The properties of high boiling point components (e.g. C1-C4) are: large cooling capacity, reduced flow rate and supply pressure, but cannot achieve low temperatures, and possess the risk of refrigerant freeze-out at low temperatures. Morosuk et al. [35] optimized a small-scale LNG process using the PRICO refrigeration cycle, they cooled LNG down to -162 °C (111 K) using a refrigerant mixture of: 0.15%mole nitrogen, 0.3%mole methane, 0.3%mole ethane, and 0.25%mole butane. 45% of the irreversibilities were attributed to the heat exchanger, and they stated that there was little potential to increase the efficiency as long as the refrigerant composition remained fixed. [35] The determination of refrigerant constituents for an MR cycle, such as the reverse Rankine cycle, is an essential part of the operation and optimization of MR cycles [40].

3.3.1 Solid-liquid equilibrium

The freezing point of a refrigerant mixture is an important parameter to prevent clogging, thereby ensuring reliable operation [25]. A general rule for designing a refrigerant mixture is that the individual freezing points should be higher than the cold end temperature [40]. Hwang et al. [40] used equation 3.8 in order to estimate the average freezing point of a refrigerant mixture. However, this estimation was stated to be conservative as the estimated freezing temperature was found to be at 90 K for a mixture of 50% N_2, 1% R14 (CF_4), and 49% R23 (CHF_3). In reality, they reported that this mixture would freeze at 118 K, as there is little liquid nitrogen to resolve the R23, implying the solubility factors are important in order to estimate the freezing point of a refrigerant mixture. [40]

$$T_f = \sum x_i T_{f,i} \tag{3.8}$$

T_f = Freezing point temperature [K]
x = Molar fraction
i = Refrigerant component

They found that utilizing a hydrofluorocarbon (HFC) mixture, the solubility for R23 and R32 is low below 90 K and freezing can be problematic. In comparison, it was found that a

mixture of: 50% N_2, 25% C1, 20% C2, and 5% C3, rarely would freeze above 85 K, implying that C1 and C2 are presumed to act as a solute in the C3 solvent. [40] Boiling point and melting point for the refrigerant constituents used in this thesis are presented in table 3.1 [4].

Table 3.1: *Boiling and freezing points for the refrigerant components used in this thesis. [4]*

Substance	**Boiling point**		**Freezing point**	
	[K]	[$^{\circ}C$]	[K]	[$^{\circ}C$]
Hydrogen	20.3	-252.9	13.9	-259.2
Neon	27.1	-246.1	24.6	-248.6
Nitrogen	77.4	-195.8	63.1	-210.0
Methane (C1)	111.2	-162.0	90.7	-182.5
Ethane (C2)	184.6	-88.5	90.4	-182.8
Propane (C3)	231.2	-42.0	85.5	-187.7
Butane (C4)	272.7	-0.5	134.8	-138.33

3.3.2 Joule-Thomson coefficient

The JT coefficient (μ_{JT}) is related to the temperature change as a gas undergoes isenthalpic expansion over a throttling valve [31], which is the case for reverse Rankine MR cycles. μ_{JT} is defined by the partial differential equation 3.9, and is dependent on both temperature and pressure. [31]

$$\mu_{JT} = \left(\frac{\partial T}{\partial p}\right)_h \tag{3.9}$$

Most gases experience temperature decrease while throttled at atmospheric conditions, however, neon, hydrogen, and helium increase their temperature [31]. The temperature of a gas will: decrease with a positive μ_{JT}; increase with a negative μ_{JT}; remain constant as $\mu_{JT} = 0$, which is denoted the inversion curve [41]. The effect can also be seen in relationship to the slope sign, from left to right, while measuring the change in entropy during an isenthalpic expansion as depicted in figure 3.7, or, the change in exergy as the throttling process is isenthalpic. [41] [31]

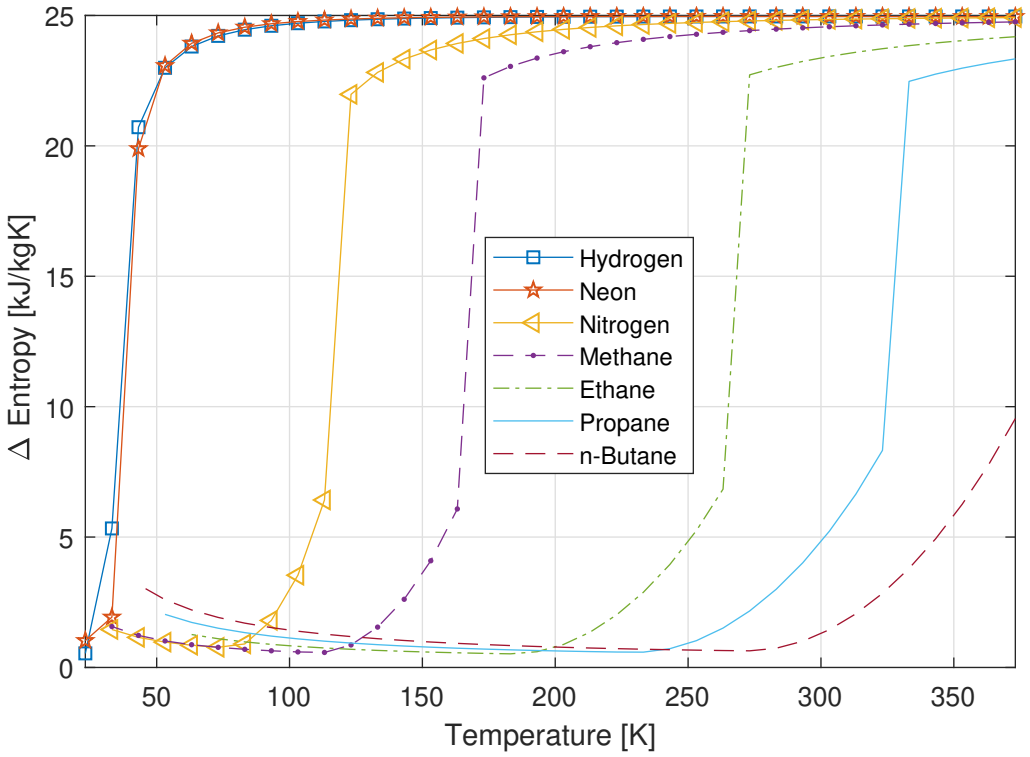

Figure 3.7: *Joule-Thomson effect for different substances during isenthalpic expansion from 20 bar to 1 bar. (figure is created in HYSYS)*

3.4 Commercialized hydrogen liquefaction plants

The hydrogen liquefaction plant in Ingolstadt, Germany, is the only existing plant found to have a detailed description of the liquefaction process [42]. The facility has an approximated production capacity of 4.4 tdp. The plant is fed with hydrogen-rich raw gas supplied from a steam methane reforming process, with a hydrogen concentration of approximately 86%, mainly containing hydrocarbon impurities (C1-C6). The feed gas is supplied at approximately 20 bar to a pressure swing adsorption (PSA) process in order to decrease the impurity levels to about 4 ppm, and further reduce impurities to <1 ppm with low-temperature adsorption. The purified hydrogen feed is then precooled to 80 K with liquid nitrogen (LIN) supplied from an air separation unit. A hydrogen Claude cycle reduces the hydrogen feed temperature from 80 K to 30 K over four temperature levels, and a throttling valve expands the hydrogen feed from approximately 20 bar to 1.3 bar reducing the temperature from 30 K to 20 K. Continuous ortho-para conversion is conducted over four temperature levels using $Fe(OH)_3$ as catalysts, resulting in a parahydrogen content of $\geq$ 95%, delivered to the hydrogen storage tank. The storage tank is multilayered and vacuum insulated in order to have a sufficiently low evaporation

rate, 0.3% per day is reported. The displacement gas and flash gas from the storage tank is fed back into the cold end of the Claude cycle in order to utilize the cold gas enthalpy. Within the Claude cycle, the JT valve throttle the hydrogen refrigerant from 21 bar to 1.2 bar and the expanders between 22 bar and 3 bar. The compression train consists of two intercooled dry piston compressors. The specific liquefaction energy is presented to be 0.95 kWh/l (approx. 13.4 kWh/kg_{H_2} (density = 71 kg/m^3)), with a thermodynamic efficiency of 33%. [42] It is pointed out by Krasae-in et al. [18] that the Leuna plant (2007) is more efficient relative to the Ingolstadt plant, as the former included the ortho-para conversion within the heat exchangers and there is no recycled hydrogen. The process flowsheet of the liquid nitrogen precooled hydrogen Claude cycle in Lenua, Germany, is depicted in figure 3.8 [18].

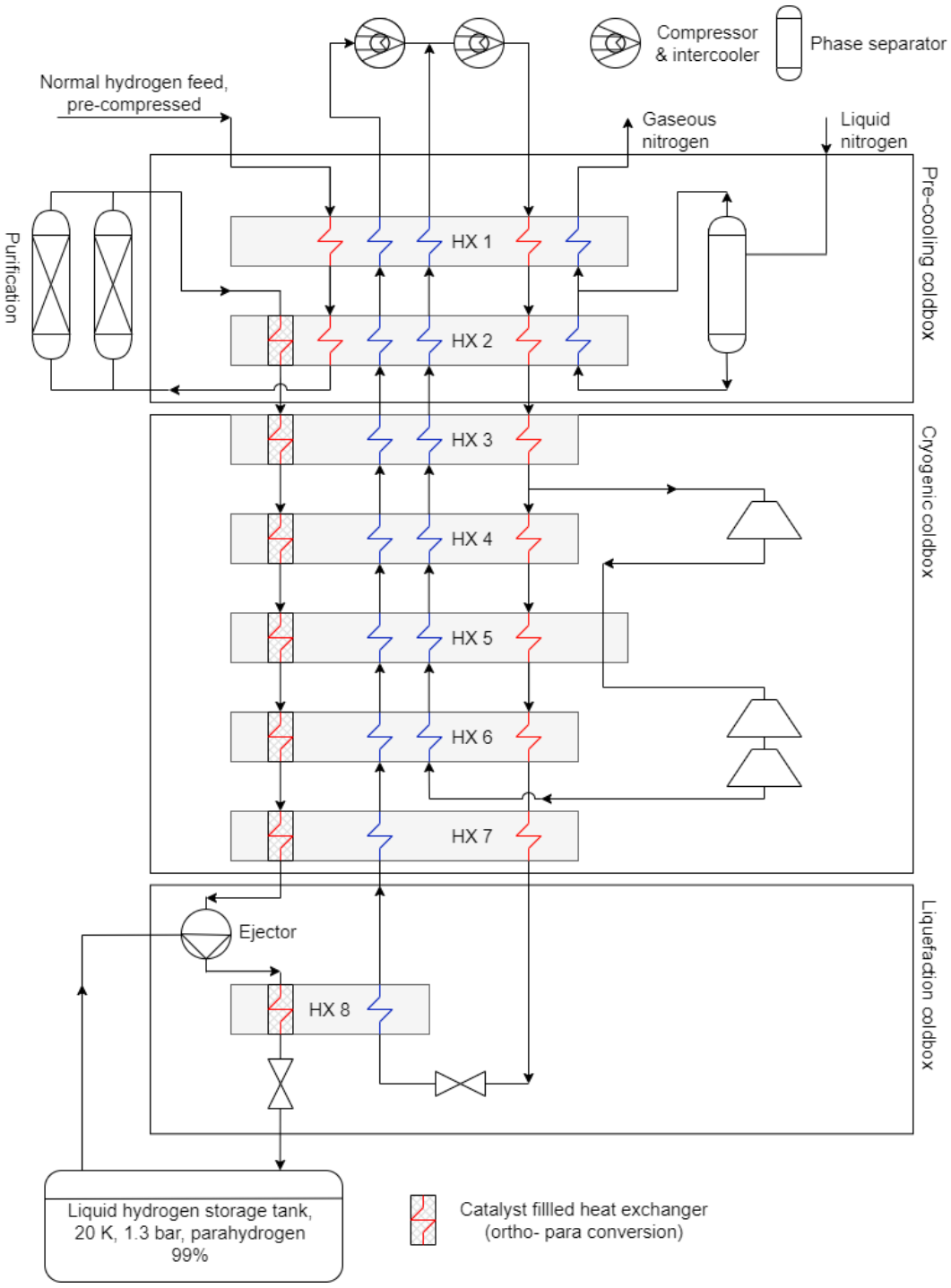

Figure 3.8: *A process flowsheet of the liquid nitrogen precooled hydrogen Claude cycle in Lenua. [18]*

3.5 Conceptualized hydrogen liquefaction plants

In recent years, there have been several publications assessing closed-loop precooled hydrogen liquefaction processes. Berstad et al. [23] did an exergy analysis of a scaled-up SMR precooled hydrogen Claude cycle. By precooling a hydrogen feed of 125 tdp, 20 bar, and 298 K down to 114 K, their optimized result for the precooling cycle showed an exergy efficiency and SEC of 42.5% and 0.786 kWh/kg_{LH_2}, respectfully. It is worth noting that the temperature into the hydrogen Claude cycle was increase from 114 K to 117.9 K, in order to account for the ortho-para conversion. For the precooling cycle, the highest irreversibilities were found within the heat exchanger at 25.7% of the total precooling irreversibilities. The optimized hydrogen Claude cycle had an exergy efficiency and SEC of 38.4% and 6.304 kWh/kg_{LH_2}. The majority of irreversibilities were related to the hydrogen compression and intercooling (39%), heat exchangers (21%), turbine brakes (15%), and turbines (13%). For the overall liquefaction cycle, the pressure drop accounted for approximately 8% of the total irreversibilities and was mostly related to the heat exchangers. About 90% of the total process irreversibilities are attributed to the hydrogen Claude cycle. The boil-off and displacement gases in the liquid hydrogen storage tank were recycled into the throttled hydrogen feed, result in a 0.085 kWh/kg_{LH_2} loss. At the lowest temperature level they included two-step expansion, consisting of a dense-phase expander and a throttling valve, in order to fully expand the hydrogen refrigerant. Also, a phase separator was included, in order to keep the heat exchanger before the storage tank flooded with liquid hydrogen. The heat exchanger in the precooling cycle did not contain any catalyst as the exothermic effect of ortho-para hydrogen conversion is limited down to the 114 K precooling temperature. Also, the impurities in the hydrogen feed can be absorbed in the catalyst, resulting in performance degradation. [23]

Cardella et al. [20] performed process optimization of a 100 tdp hydrogen liquefier. They investigated two precooling concepts, SMR- and DMR-cycle, combined with a hydrogen Claude cycle. The SMR used a four-component mixed refrigerant, which was composed of nitrogen and up to three of the C1-C5 hydrocarbons, but the composition was not mentioned. The lower temperature cycle of the DMR contained a refrigerant mixture of hydrogen and neon. Overall, the SMR precooler showed improved SEC relative to the DMR. Both concepts were energy optimized with fixed pressure at 25 bar, and a variable feed pressure, between 25-80 bar. In addition, a cost optimization with reduced heat exchanger size was also included for the fixed pressure. For both concepts, the optimized results show that the increased feed pressure at 80 bar, was a marginally better solution in terms of SEC, however, the specific liquefaction cost (SLC) did not favor the higher pressure. Furthermore, they showed that the economics of scale

played a significant role in terms of SLC. Energy optimization of the hydrogen liquefaction process with the SMR precooling concept at 25 bar, showed an SEC of 6 kWh/kg_{LH_2} and the cost optimization had an SEC of 6.2 kWh/kg_{LH_2} with an exergy efficiency of 43%. [20]

Krasae-in et al. [43] performed simulation and experiment on a 0.6 kg_{LH_2}/h hydrogen liquefaction test rig, using a MR precooling cycle. Initially, they managed to precool the 21 bar hydrogen feed from 25 °C to -158 °C, using a five-component refrigerant mixture in the test rig. The initial refrigerant mixture consisted of 1% neon, 10% nitrogen, 33% methane, 38% ethane, and 18% butane. By marginally increasing the mole fraction of nitrogen the precooling temperature was further reduced to -180 °C, resulting in an SEC of 1.76 kWh/kg_{LH_2}. They state that a further increase of highly volatile components is required to decrease the precooling temperature. And, they recommended designing precooling processes that could reach -200 °C, for future large-scale hydrogen liquefaction plants. The high pressure of the MR-cycle was set to 18 bar which was necessary in order to cool the hydrogen feed due to the throttling effect (Joule-Thomson effect). Also the 18 bar pressure was needed in order to prevent freeze out in the MR-cycle. It was explicitly mentioned that the hydrogen feed pressure must be greater than the supercritical pressure of 15 bar, in order to avoid condensation. They used a 21 bar hydrogen feed that is similar to the Ingolstadt plant, which was recommended. Also, it was mentioned that for liquid hydrogen storage, the pressure should be between 1.3 to 2 bar. The ortho-para conversion was not included in the test rig as the heat exchangers did not contain any catalyst. [43]

Krasae-in [21] performed optimization on a modified MR precooled hydrogen Joule-Brayton cycle. He used four Joule-Brayton cycles where all heat exchangers were integrated with the MR heat exchangers, and the largest heat exchanger had 12 streams. The novelty of this work was to take into consideration the ortho-para conversion between -193 °C and -253°C within the Joule-Brayton cycle, compared to ref. [43]. He suggested to precool hydrogen from 25 °C to -193 °C with a five-component refrigerant mixture, for a 100 tdp liquid hydrogen production capacity. The optimized result showed an SEC of 1.38 kWh/kg_{LH_2} and 4.24 kWh/kg_{LH_2} for the MR precooling cycle and Joule-Brayton cycle. He accounted for pressure drops within the heat exchangers and stated that the pressure drop was not significant for the total power consumption. A conceptualized flowsheet of an MR precooled, two hydrogen Joule-Brayton cycle based on the latter paper is depicted in figure 3.9. [21]

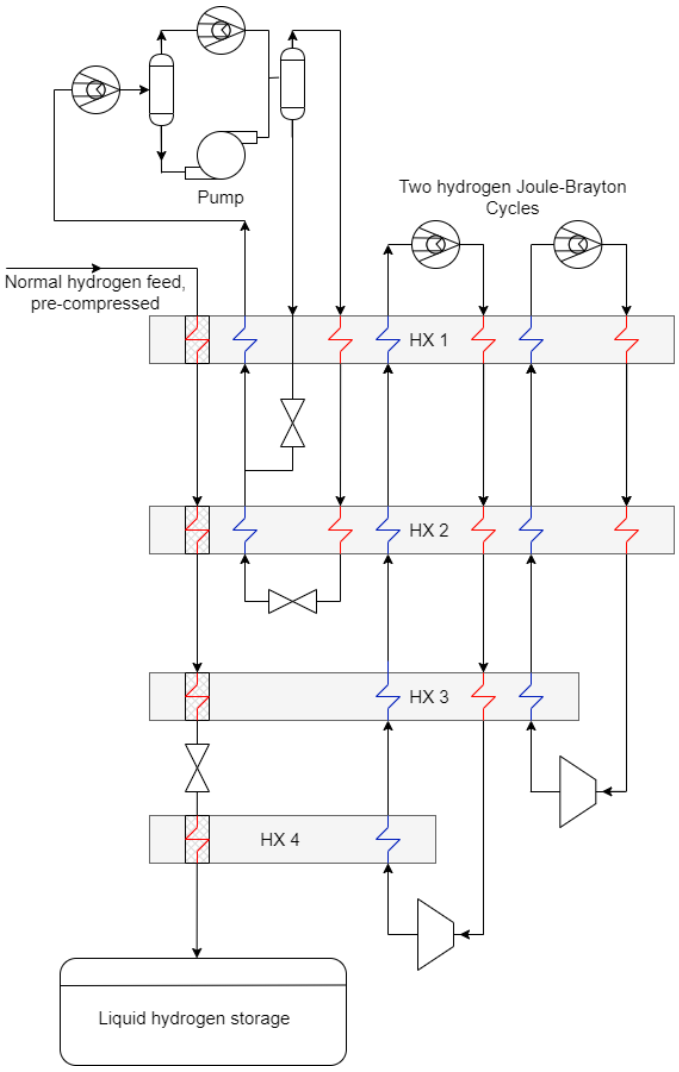

Figure 3.9: *A conceptualized flowsheet of the MR precooled, two hydrogen Joule-Brayton cycle, based on ref. [21].*

Asadina et al. [22] studied the performance of a combined MR precooled hydrogen/helium Joule-Brayton cycle, utilizing six Joule-Brayton cycles. The liquefaction process had a hydrogen feed of 100 tdp, 21 bar, ambient temperature 25 °C which was precooled down to -198.2 °C. Ortho-para conversion was included between -198.2 °C and -253°C. The precooling section consists of a main MR and an auxiliary MR cycle, and a 11 component refrigerant mixture and pure hydrogen, respectively. Unlike Krasae-in [21], Asadina et al. [22] utilized an auxiliary precooler with pure hydrogen, the precooling section was not integrated with the Joule-Brayton cycles, and they had fewer temperature levels in the cryogenic section, although there were two more JB-cycles. Furthermore, the optimization was conducted by trial and error, suggesting that there is room for improvement. Table 3.3 shows performance indicators collected from the

aforementioned research reviewed above, accompanied by the refrigerant composition in table 3.2. [22]

Table 3.2: *Refrigerant mixture for the precooling cycles of the reviewed conceptualized hydrogen liquefiers presented above.*

Ref.	Berstad et al. [23]	Cardella et al. [20]	Krasae-in et al. [43]	Krasae-in [21]	Asadina et al. [22]	Unit
Refrigerant component						
Hydrogen	-	-	-	4	0.02	%mole
Neon	-	-	1	-	-	%mole
Nitrogen	Yes	Unknown	10	18	6.42	%mole
Methane	Yes	Unknown	33	24	10.21	%mole
Ethane	Yes	Unknown	38	28	19.25	%mole
Propane	Yes	Unknown	-	-	5.32	%mole
n-Butane	Yes	Unknown	18	26	2.35	%mole
n-pentane	-	-	-	-	29.85	%mole
propene	-	-	-	-	12.73	%mole
ref-14	-	-	-	-	9.86	%mole
i-butane	-	-	-	-	2.43	%mole
ammoina	-	-	-	-	1.58	%mole

Table 3.3: *Performance indicators for the reviewed conceptualized hydrogen liquefiers above.*

Ref.	Berstad et al. [23]	Cardella et al. [20]	Krasae-in et al. [43]	Krasae-in [21]	Asadina et al. [22]	Unit
Hydrogen feed						
Mass flow	125	100	0.6 kg/h	100	100	[tdp]
Pressure	20	25	21	21	21	[bar]
Temperature	298	303	298	298	298	[K]
Precooling temperature	114	-	115	80	74.8	[K]
Liquid hydrogen						
Pressure	1.5	2	2	1.3	1.3	[bar]
Temperature	21.47	22.8	22	20	20.8	[K]
pH_2 fraction	97	98	25	95	95	[%
Isentropic efficiency						
Compressors	85	0.78-0.86	85*	90	80	[%]
Expanders	85	0.78-0.88	85*	90	80	[%]
MTA						
Plate-fin HX	-	0.5-2	-	3-10	1-2	[K]
Intercoolers	10	5	-	5	0	[K]
Exergy efficiency						
Precooling cycle	42.5	-	-	-	-	[%]
Liquefaction cycle	38.4	-	-	-	-	[%]
Total	-	43	-	-	39.5	[%]
Energy recovery	-	80	-	-	yes	[%]
SEC						
Precooling cycle	0.786	-	1.76	1.38	1.588 [4]	$[\frac{kWh}{kg}]$
Liquefaction cycle	6.304	-	-	4.24	6.107	$[\frac{kWh}{kg}]$
Total	7.09	6.2	-	5.91	7.695	$[\frac{kWh}{kg}]$

Methodology

This chapter will explain the methodology used to create the refrigeration models, simulations, and optimizations for the hydrogen liquefaction process. Aspen HYSYS and Matlab have played a crucial role in order to model, simulate and optimize the refrigeration cycles. And, the reference fluid property software Refprop, was necessary to create an estimated equilibrium hydrogen model, in order to account for continuous ortho-para hydrogen conversion within the heat exchangers.

In order to reduce the complexity of the thesis, small segments of discussion will be present in the methodology chapter.

4 The equilibrium hydrogen model

This section will describe how the estimated equilibrium hydrogen model was created, and implemented into Aspen HYSYS. Along with an explanation of how the hydrogen equilibrium model was validated.

4.1 Creating the thermodynamic model for equilibrium hydrogen

Aspen HYSYS does not include thermodynamic properties for equilibrium hydrogen. In order to take into consideration continuous ortho-para hydrogen conversion, a manual temperature-enthalpy (T-h) and temperature-entropy (T-s) property table for equilibrium hydrogen had to be calculated and implemented into HYSYS. In order to create an estimated equilibrium hydrogen, a model for the parahydrogen concentration at the temperature range, from 298 K to 20 K, was required. The parahydrogen concentration model presented by Valenti et al. [27] was used to describe the expected concentration of parahydrogen, at a given temperature. The model is based on the Fermi-Dirac statistical weights for J-th quantum level, g_J, which is applicable for hydrogen, and is calculated with equation 4.1. The equation is dependent on the nuclear spin of the proton, i, and the statistical weight of an electron level, g_e.

$$g_J = \begin{cases} g_e(2i+1)i(2J+1), J_{even}(para) \\ g_e(2i+1)(i+1)(2J+1), J_{odd}(ortho) \end{cases} \tag{4.1}$$

The J-th quantum energy state is calculated with equation 4.2 and is dependent on Planck's constant, k, and the molecular hydrogen moment of inertia, I.

$$E_{J_n} = J_n(J_n+1)\frac{h^2}{8\pi^2 I} \tag{4.2}$$

The ratio for the average number of parahydrogen molecules, β, is dependent on the Boltzmann constant, k, and the aforementioned equations, and is calculated with equation 4.3, where the variable temperature (T) was set to define the range from 298 K to 20 K.

$$\beta(T) = \frac{\sum_{J=even} g_j e^{-\frac{E_J}{kT}}}{\sum_{J=odd} g_j e^{-\frac{E_J}{kT}}} \tag{4.3}$$

Equation 4.5 and 4.4 describes the concentration of ortho- and parahydrogen, respectively, at the given temperature ($\beta(T)$). The result is depicted previously in figure 2.4.

$$x_{pH2} = \frac{\beta(T)}{1+\beta(T)} \tag{4.4}$$

$$x_{oH2} = 1 - x_{pH2} \tag{4.5}$$

The numerical input for equation 4.1 through 4.3 is presented in the list below.

J_{even} = 0,2,4...
J_{odd} = 1,3,5...
i = $\frac{1}{2}$
g_e = 1
h = $6.62606896e^{34}[Js]$
k = $1.3806504e^{23}[\frac{J}{K}]$
I = $4.67e^{-48}[\frac{kg}{m^2}]$

The enthalpy and entropy for normal- and parahydrogen were obtained in the property software Refprop, from the National Institute of Standards and Technology (NIST). In order to

obtain the correct enthalpy and entropy for normal- and para-hydrogen, the default reference state within Refprop had to be modified. For saturated liquid, at normal boiling point, the enthalpy and entropy were set to 702.98 kJ/kg and 0.018269 $kJ/kg \cdot K$, as suggested by Jacob Leachman [28]. The numerical enthalpy and entropy values obtained in Refprop for normal- and parahydrogen at 21 bar is presented in appendix A. In order to create an estimated equilibrium hydrogen enthalpy and entropy profile, equation 4.4 was combined with the T-h and T-s data for normal hydrogen (25% pH_2), and parahydrogen (100% pH_2), obtained in Refprop. This resulted in equation 4.6 and 4.7 for enthalpy and entropy. The method for calculating an estimated equilibrium hydrogen model was indicated by Eckroll [44]. Subscript, i, denotes the given numerical values at temperature, T, and subscript, 0, is the value at 298 K.

$$h_{eH_{2_i}} = h_{nH_{2_i}} + (h_{pH_{2_i}} - h_{nH_{2_i}})\left(\frac{x_{pH_{2_i}} - x_{pH_{2_0}}}{1 - x_{pH_{2_i}}}\right) \tag{4.6}$$

$$s_{eH_{2_i}} = s_{nH_{2_i}} + (s_{pH_{2_i}} - s_{nH_{2_i}})\left(\frac{x_{pH_{2_i}} - x_{pH_{2_0}}}{1 - x_{pH_{2_i}}}\right) \tag{4.7}$$

h = Mass specific enthalpy $[\frac{kJ}{kg}]$
s = Mass specific entropy $[\frac{kJ}{kgK}]$
x_{pH_2} = Parahydrogen concentration

The numerical results for the estimated equilibrium hydrogen calculations, from equations 4.6 and 4.7, are presented in appendix B for enthalpy and entropy. They are illustrated in figure 4.1 and 4.2, along with normal- and parahydrogen obtained in Refprop.

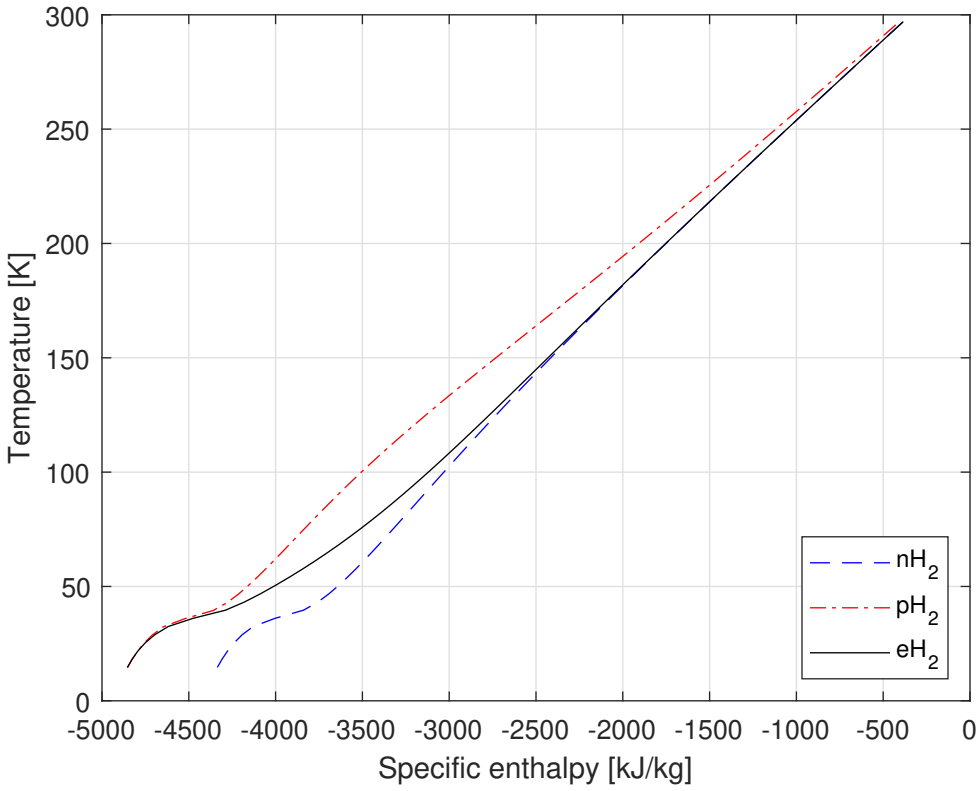

Figure 4.1: *Enthalpy profile for normal-, para- and the estimated equilibrium hydrogen model.*

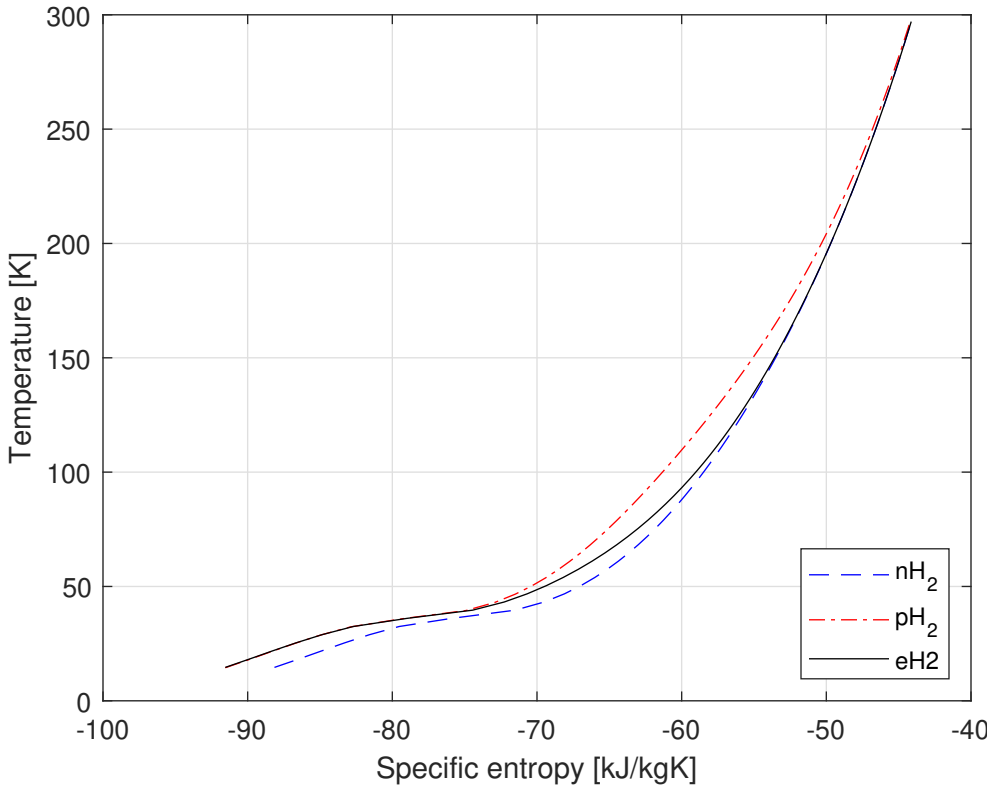

Figure 4.2: *Entropy profile for normal-, para- and the estimated equilibrium hydrogen model.*

In order to implement enthalpy and entropy for equilibrium hydrogen into Aspen HYSYS, the Modified Benedict Weber Ruben (MBWR) equation of state (EOS) was modified by adding the numerical values calculated with equation 4.6 and 4.7 to the tabular option, for the selected EOS. By utilizing the built-in regression tool, the constants used for HYSYS enthalpy and entropy calculation were modified so that a model accounting for continuous ortho-para hydrogen conversion was obtained for the required temperature span. The regressed model was divided into two temperature levels, one for the precooling temperature range (298K-80K), and one for the cryogenic temperature range (120K-20K). Dividing the model into two temperature levels was done in order to have a closer match between the input values and the regressed model, due to the non-linearity at lower temperatures. The polynomials in equation 4.8 and 4.9 were used for the regression, which was dependent on the equations accuracy for the model fitting. The constants obtained from the different regressions are presented in table 4.1.

$$X_{eH_2} = a + bT + cT^2 + dT^3 + ... + jT^9 \tag{4.8}$$

$$X_{eH_2} = a + bT + cT^2 + d \cdot ln(T^3 - e) \tag{4.9}$$

Table 4.1: *The constants obtained by regressing the calculated enthalpy and entropy for the estimated equilibrium hydrogen, within Aspen HYSYS.*

Temperature range	**298-80 K**		**120-20 K**			
X_{eH_2}	Enthalpy	Entropy	Enthalpy		Entropy	
Phase	Vapour	Vapour	Vapour	Liquid	Vapour	Liquid
Equation	4.8	4.9	4.8	4.8	4.9	4.8
a	-1.22·e^{4}	-3.21·e^{2}	-6.44·e^{3}	-1.36·e^{5}	-3.21·e^{2}	-4.63·e^{1}
b	1.37·e^{2}	-2.91·e^{-1}	-4.83·e^{2}	3.76·e^{4}	-2.91·e^{-1}	-7.19·e^{0}
c	-1.71·e^{0}	4.24·e^{-4}	2.41·e^{1}	-4.77·e^{3}	4.24·e^{-4}	-3.74·e^{0}
d	1.64·e^{-2}	1.65·e^{1}	-5.38·e^{-1}	3.37·e^{2}	1.65·e^{1}	6.03·e^{-1}
e	-1.07·e^{-4}	0.00·e^{0}	6.80·e^{-3}	-1.45·e^{1}	0.00·e^{0}	-4.08·e^{-2}
f	4.90·e^{-7}	-	-5.23·e^{-5}	3.92·e^{-1}	-	1.52·e^{-3}
g	-1.55·e^{-9}	-	2.49·e^{-7}	-6.57·e^{-3}	-	-3.37·e^{-5}
h	3.19·e^{-12}	-	-7.17·e^{-10}	6.43·e^{-5}	-	4.37·e^{-7}
i	-3.85·e^{-15}	-	1.15·e^{-12}	-3.16·e^{-7}	-	-3.08·e^{-9}
j	2.05·e^{-18}	-	-7.78·e^{-16}	4.94·e^{-10}	-	9.12·e^{-12}

4.2 Validation of the equilibrium hydrogen model

The method for obtaining enthalpy and entropy for normal- and para-hydrogen in Refprop resulted incoherence with the numerical values for the heat of conversion found in literature [45], as depicted in figure 4.3.

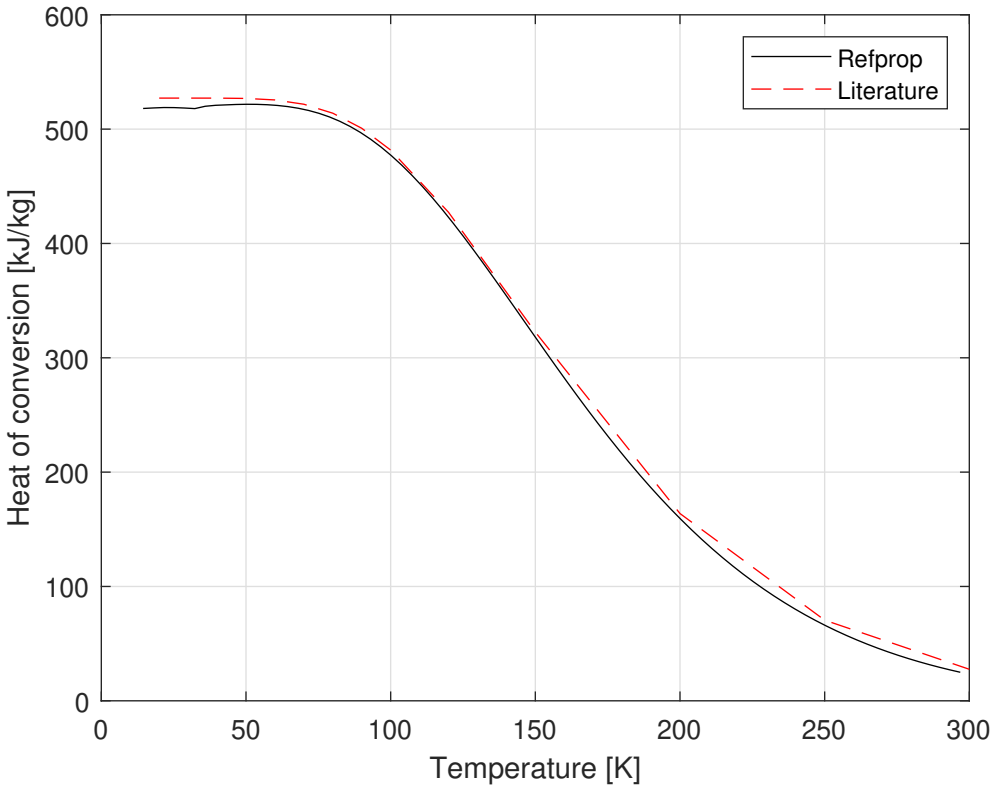

Figure 4.3: *The figure shows the similarity for the normal to para heat of conversion obtained in the literature [45] relative to the difference between enthalpy for normal- and parahydrogen obtained in Refprop.*

By investigating figure 4.4 and 4.5, the slope of the regressed precooling and calculated equilibrium hydrogen model for enthalpy and entropy is more or less identical, which is caused by a relatively linear curve for the calculated model. However, the non-linearity increases at lower temperatures which will increase the deviation of the regressed cryogenic model relative to the calculated model. Initially, a weighted regressed model was applied to ensure smaller deviation at the lowest temperatures in order to achieve coherence between the gaseous and liquid equilibrium models. This is not revealed for the non-weighted model in the figures, due to a sudden temperature increase and decrease at the gas/liquid interface. This would be apparent if the resolution of the plotted values was very high. If a temperature spike occurs as the heat balance is calculated, within the heat exchanger while optimizing in HYSYS, there could be an optimized result that would be deemed not valid due to the temperature crossing of the composite curves. The weighted model created some deviation in the 45-80 K temperature range relative to the non-weighted- and calculated-equilibrium model.

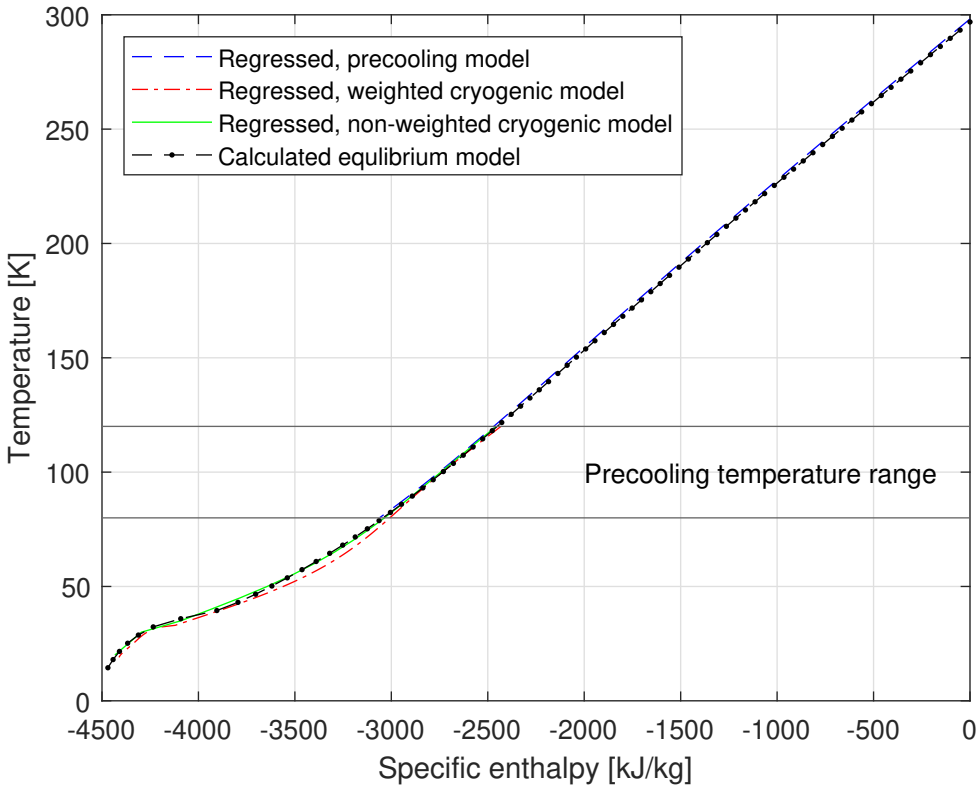

Figure 4.4: *Shows the difference between the calculated and regressed equilibrium hydrogen model for specific enthalpy.*

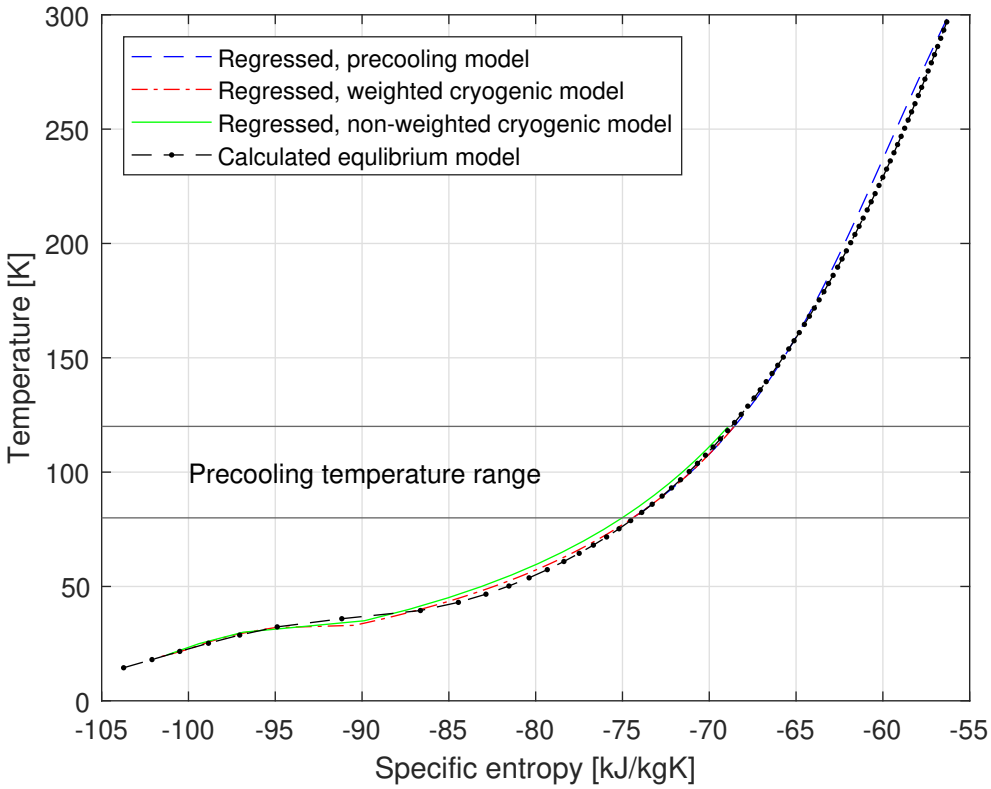

Figure 4.5: *Shows the difference between the calculated and regressed equilibrium hydrogen model for specific entropy.*

Figure 4.6 depicts the specific exergy of equilibrium- and normal-hydrogen (21 bar) at temperature, T, with 300 K specified as the dead state (T_0). In between 300 K to 150 K the two lines should ideally be matched, due to the limited difference in parahydrogen content. This is most likely due to the discrepancy between the regressed- and calculated-model for the entropy of equilibrium hydrogen, as depicted in figure 4.5 for the same temperature range. By comparing the specific exergy in figure 4.6 to the specific exergy obtained by Valenti et al. [27], the specific exergy is similar, but there are relatively small deviations throughout the temperature span. Theses deviations might be due to the accuracy of the model fitting, or that the method for obtaining the equilibrium model is different. As the method for obtaining the equilibrium model in this thesis differentiate from e.g. Valenti et al. [27], it is assumed that the method for obtaining the estimated equilibrium hydrogen model is close to valid.

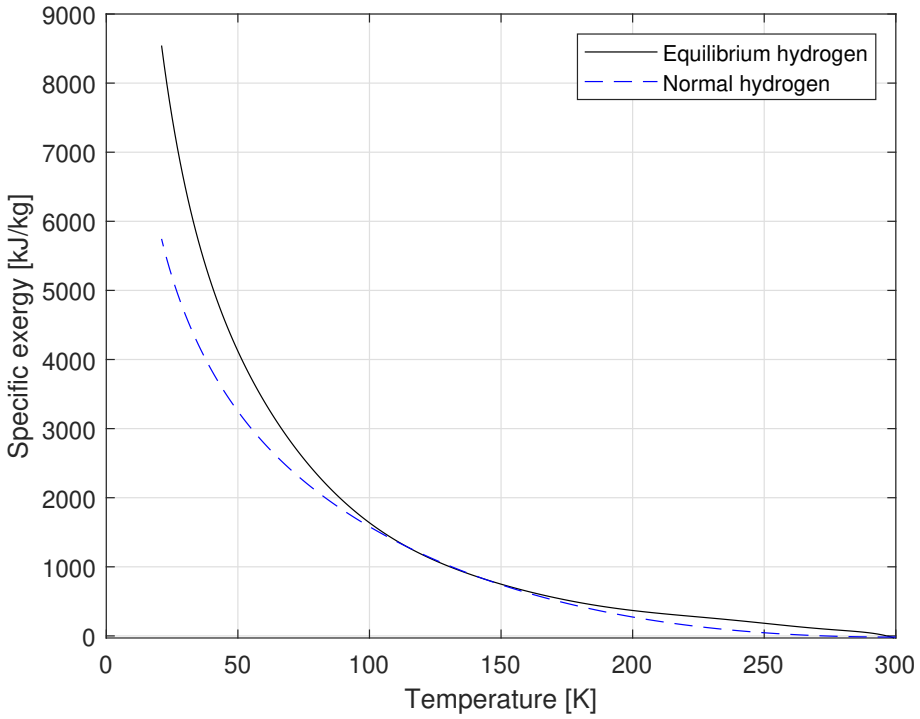

Figure 4.6: *The specific exergy for normal- and equilibrium hydrogen at $p = 21$ bar, $T_o = 300$ K. The equilibrium hydrogen exergy is based on the model created for the purpose of this thesis.*

The model depicted in figure 4.7 was used to validate the equilibrium hydrogen model relative to the reference case [23]. The stream properties in figure 4.7 were set equal to the results obtained by Berstad et al. [23], except the temperature output from the catalyst filled heat exchanger side, denoted T in the figure. The MBWR EOS was used for the non-filled catalysts sides of the heat exchanger, and the estimated equilibrium hydrogen model (modified MBWR EOS) was used to simulate the catalyst-filled heat exchanger side. The validation was conducted by calculating the heat balance with the estimated equilibrium hydrogen model for each heat exchanger and compare the temperatures output to the reference case.

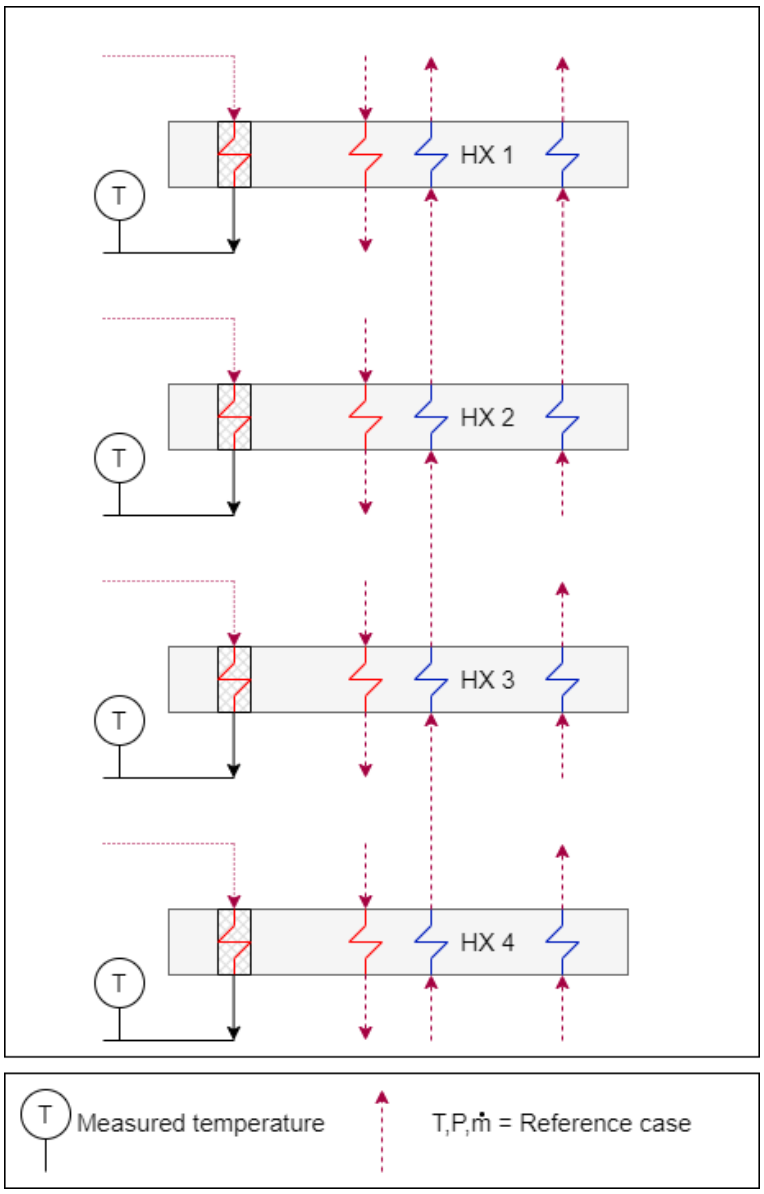

Figure 4.7: *Model used for validating the equilibrium hydrogen model.*

Due to the difficulty of obtaining a even closer match between the calculated and regressed hydrogen equilibrium model, it was assumed to be a reasonable estimation, due to the "relatively" small deviation between the reference case temperature and the ones calculated with the equilibrium models. In addition, there might have been other heat exchanger parameters used in the reference case differentiating from the validation model, which could have affected the heat balance calculations. The input and output temperature of the heat exchangers for the reference case, weighted, and non-weighted regression is presented in table 4.2.

Table 4.2: *Comparison between the temperature input and output for the catalyst filled side of the heat exchanger, in the cryogenic cooling cycle.*

	Ref. case [23]	**Non-weighted**	**Weighted**
Temperature	[K]	[K]	[K]
HX $1_{T,input}$	117.9	117.9	117.9
HX $1_{T,output}$ & HX $2_{T,input}$	106.0	106.3	107.1
HX $2_{T,output}$ & HX $3_{T,input}$	72.5	71.1	68.6
HX $3_{T,output}$ & HX $4_{T,input}$	46.0	46.5	45.4
HX $4_{T,output}$	30.0	27.9	30.7

5 Process description

Initially, this thesis selected the SMR and DMR concept as option for the precooling cycles, and a hydrogen Claude cycle for the cryocooling in order to investigate how the precooling temperature affects the total exergy efficiency and SEC of a hydrogen liquefier. The precooling temperature at the interface of the precooling- and hydrogen Claude-cycles has been optimized for each temperature in between 80 K and 120 K, with a 10 K step interval. This resulted in five different precooling temperatures, where the precooling- and hydrogen Claude-cycle have been optimized separate from each other. The precooling outlet stream is set to have equal properties to the inlet of the corresponding cryogenic hydrogen Claude cycle.

The properties for the hydrogen feed, liquid hydrogen product, and the ambient condition used in the hydrogen liquefaction simulation are summarized in table 5.1.

Table 5.1: *A general property table for the hydrogen feed, $H_{2,feed}$, saturated liquid hydrogen product, LH_2, and the ambient condition used in the hydrogen liquefaction simulation.*

	Temperature [K]	**Pressure [bar]**	**Flow rate [$\frac{kg}{s}$]**
$H_{2,feed}$ (FO1)	298.00	21.0	1.157
LH_2 (F11)	21.15	1.3	1.157
Ambient	298.00	1.0	-

5.1 Process modeling

Multiple configurations for the SMR- and DMR-precooling-cycles were initially modeled and optimized in order to find the assumed optimal configuration for the precooling temperature range (80-120 K). For the DMR precooling cycle, several configurations were modeled and optimized. However, the optimized results showed reduced performance relative to the SMR cycles investigated, when butane was excluded from the refrigerant mixture in the subcooling cycle due to the possibility of freeze-out. The additional optimization variables required for the DMR might be one of the reasons for the unexpected performance. By optimizing with the same refrigerant constituents in both precooling- and subcooling-cycle, the optimized exergy efficiency showed a slight improvement relative to the SMR cycles. Including butane in the subcooling cycle defeats the purpose of utilizing the DMR process in the hydrogen liquefaction process, as butane is assumed to have a high probability of freezing at lower temperatures. The Kleemenko SMR concept refrigeration cycle seemed to achieve the benefits in terms of reducing

the freeze-out possibility, if a certain degree of phase separation was added for lower precooling temperatures, and, a relatively high exergy efficiency.

A common addition to the precooling cycles is to utilize a phase separator in between the compression train, after intercooler, in order to pressurize the potential refrigerant liquid with a pump. However, several initial optimization results indicated no flow of liquid at this stage and is therefore neglected in the final optimization procedure. The methodology for selecting the SMR precooling cycle configurations will be further explained in the following subsections. However, only the final precooling configurations will be illustrated and presented in order to reduce the complexity of this thesis

The ortho-para conversion of the hydrogen feed has been considered for all heat exchangers except the heat exchanger before to the saturated liquid hydrogen product, which will be explained further in the hydrogen Claude cycle methodology. Ortho-para conversion is commonly not included for higher temperature heat exchangers due to purification issues related to the hydrogen feed, and the exothermic ortho-para conversion effect is minor at higher temperatures. The hydrogen feed is assumed to be 100% hydrogen, hence no further purification is required. The precooling temperature range is spanning from 80 K to 120 K, resulting in a 49% to 33% parahydrogen content leaving the precooler, which is seemingly significant. Due to the aforementioned reasons it was justified to account for ortho-para conversion at higher temperatures. In order to simplify the modeling and optimization, this thesis has not accounted for the boil-off and displacement gases in the liquid hydrogen storage tank. The parahydrogen concentration is approximated to be 97% at the hydrogen Claude cycle outlet.

The general assumptions made for modeling of the refrigeration cycle is listed below:

- The MTA at the intercoolers outlet stream is set to 5°C, relative to the ambient.
- Counter flow heat exchangers are used in all cases.
- The stream temperature of the warm composite at the heat exchanger outlet is set equal to each other. The stream temperature of the cold composite is set equal out of the heat exchangers.
- The isentropic efficiency for: expanders = 85%; centrifugal compressors = 80%; reciprocating compressors = 85%.
- In each precooling cycle, the pressure ratio is equal for all compressors.

- A reasonable pressure ratio is assumed to be approximately 2-3.
- Neglected pressure drop in heat exchangers, intercoolers, separators, and mixers.
- Adiabatic condition for all components except the intercoolers.
- The hydrogen feed is assumed to be pre-compressed prior to the precooling cycle.
- The hydrogen feed is assumed to be 100% hydrogen, and no additional purification is required.
- Kinetic- and potential energies/exergy is neglected.
- The heat exchanger intervals were set to 10.
- Peng-Robinson EOS is used for the mixed refrigerant, and the MBWR EOS was used to simulate the normal hydrogen refrigerant
- The MBWR was used as a basis to create the equilibrium hydrogen model used in the hydrogen feed.

For each compressor an intercooler is installed to reduce the required work for the consecutive compressor, and to reject heat from the system in order to obtain the refrigeration effect. The pressure ratio (PR) for the compressors is calculated with equation 5.1, which was supplied by the supervisors.

$$PR = \left(\frac{P_H}{P_L}\right)^{\frac{1}{n_c}} \tag{5.1}$$

PR = Pressure ratio
P_H = Higher pressure level [bar]
P_L = Lower pressure level [bar]
n_c = Number of compressors

5.1.1 Case 1: SMR cycle, one phase separator

Figure 5.1 represents the initial model used as a basis for the different SMR cycle configurations which is based on the basic Kleemenko process. The reason for choosing the Kleemenko model over the PRICO was to reduce the probability of refrigerant freeze-out as no

scientific methodology for freezing point estimations has been obtained for multi-component mixtures. After comparing several optimized configurations the model in figure 5.1 was found to be the process achieving the highest overall efficiency for the whole precooling temperature range. However, it was only used for the 110 K and 120 K precooling temperatures, as it was assumed to have adequate component separation to limit the freeze-out probability at these precooling temperatures, and the freeze-out probability was assumed to be higher for lower precooling temperatures.

The SMR refrigeration cycle depicted in figure 5.1 compresses the refrigerant mixture and rejects the heat to the surroundings with multistage compression and intercooling, from stream R01 through R05. The high pressure (HP) refrigerant mixture enter the phase separator as a two-phased flow, separating the least from the most volatile components. The liquid refrigerant composition (L01) is cooled by the cold composite in HX 1 before throttled over valve 1 (JT 1) into a lower pressure (LP) at L03. The gaseous refrigerant composition leaving separator 1 rejects heat to the cold composite at the consecutive temperature levels and is throttled over JT 2 into LP at R09. R09 acts as the cooling load for the warm composite in HX 2 and is consecutively mixed with stream L03 in mixer 1 at equal pressures, lastly stream R11 is cooling the warm composites of HX 1 completing the cycle.

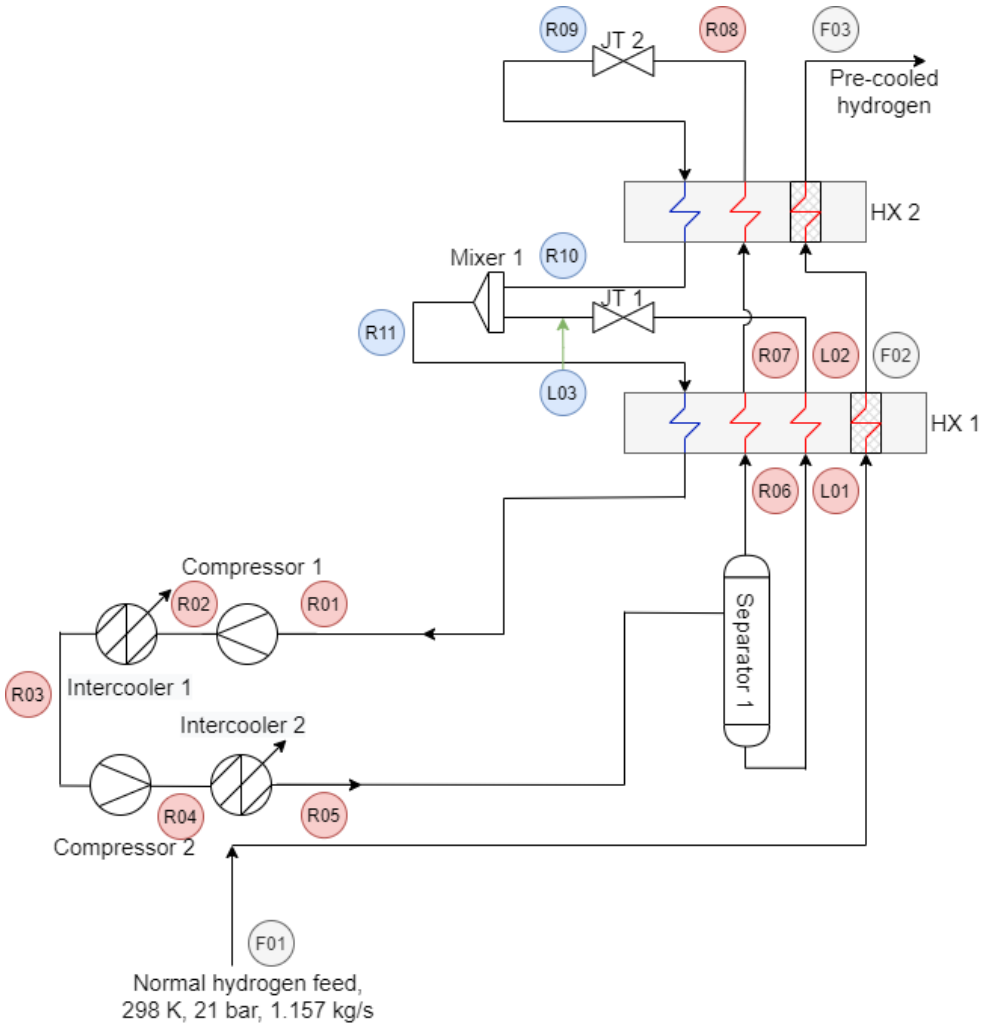

Figure 5.1: *Case 1: SMR cycle with one separator.*

5.1.2 Case 2: SMR cycle, two phase separators

Figure 5.2 represents case 2 and is an iteration based on the configuration used in case 1. Case 2 was obtained by optimizing several configurations with additional heat exchangers and separators relative to case 1. By adding more than two separators the optimization became more challenging due to the high degree of separation. This resulted in a non-feasible solution interrupting the optimization procedure, as there was not sufficient refrigerant flow rate at the last temperature level to calculate the heat balance in HX 4, for lower precooling temperatures (approximately 80-100 K). In order to assess this problem, a lower optimization limit was selected for the hydrogen or neon mass flow rate to ensure sufficient flow in HX 4. Another solution could be to constrain the lower temperature optimization boundary into separator 2 (R08) to ensure limited phase separation. However, this would also be dependent on the high-pressure limit. Optimization results from the three-stage phase separator configuration, showed less efficiency than two-stage phase separation although this was assumed to be due to the constrained limits to ensure sufficient flow in HX 4. Three-stage phase separation was discarded as the PSO optimization process is highly time-consuming, and multiple optimization iterations were required to find a lower flow rate limit adequate to continuously run the optimization, and to ensure that the final result was not bounded by the constraints. Based on the preliminary optimizations, case 2 was found to be the optimal configuration for the precooling temperatures between 80-100 K, taking into account that this model has lower possibility for refrigerant freeze out.

The SMR refrigeration cycle depicted in figure 5.2 follows the same principle as explained in the second paragraph in the previous section for case 1. The main difference is the additional phase separator (separator 2) which ensures a higher degree of separation, reducing the possibility of refrigerant freeze-out risk at the lowest temperature level (R11/R12).

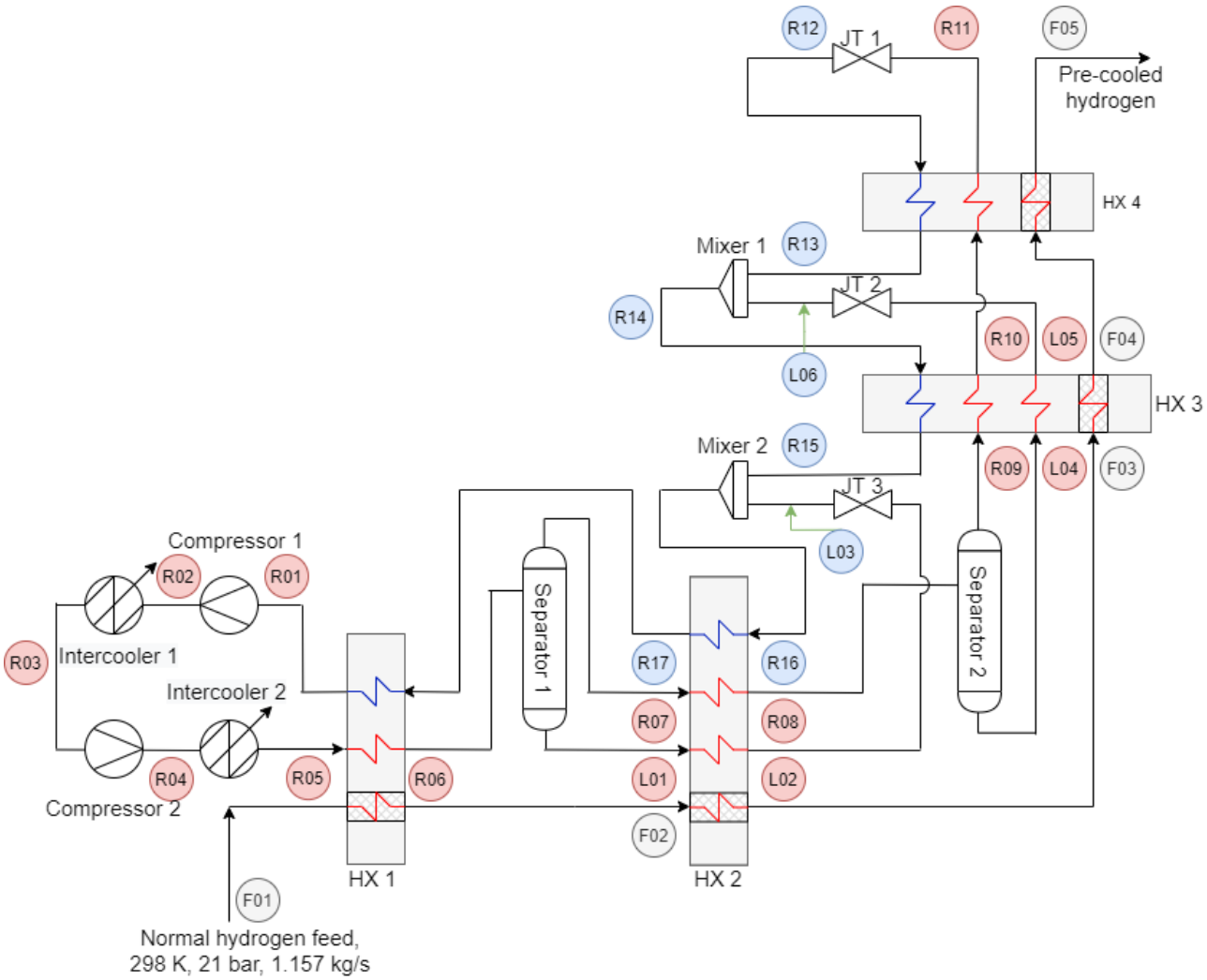

Figure 5.2: *Case 2: SMR cycle with two separator.*

5.1.3 Hydrogen Claude cycle

The hydrogen Claude cycle adopted for the cryogenic refrigeration cycle was based on the hydrogen Claude cycle utilized by Berstad et al. [23]. The configuration difference between the reference case and the one depicted in figure 5.3 is that the latter has not included: liquid hydrogen storage boil-off and displacement gases; dense phase expansion before the throttling valve (JT 1.1); no phase separator after the throttling valve (JT 1.1) which is used to keep the cold side of HX 10 flooded with liquid hydrogen; not accounting for pressure drops over the components. The main reason for excluding some of these components were due to the difficulty of modeling and optimizing with recycling units in HYSYS.

Starting from the low-pressure stream C01 in figure 5.3, the hydrogen refrigerant undergoes two multistage compression (reciprocating compressors) and intercooling, to a medium pressure level (C05), and a high-pressure level (C10). Stream C10 is cooled in HX 5 to a temperature that is approximately equal to the precooled hydrogen feed (F03/5). In HX 6 the warm composite rejects heat to the cold composite. In the consecutive temperature levels, the high-pressure refrigeration stream is split at several stages and expanded to the medium pressure levels (turbine expander), this is done to provide different cooling loads at each temperature levels due to the difference between normal- and equilibrium hydrogen heat capacity. At F09 the hydrogen feed temperature is fixed at 30 K then throttled (JT1.2) into a two-phase region, rejecting the remaining heat to the throttled two-phase refrigerant (R26) in HX 10. Stream R27 absorbs heat from the high-pressure refrigerant and the hydrogen feed as it is directed towards the low pressure side of the compression train. At F11 the hydrogen product is fully saturated.

From stream R09 to the liquid hydrogen product (R11) in figure 5.3, the EOS was changed from the equilibrium hydrogen model to MBWR EOS representing normal hydrogen. This was done because the throttling valve (JT 1.2) cannot be assumed to contain catalyst providing the ortho-para conversion. Therefore, the saturated liquid hydrogen has a estimated parahydrogen content at 97%, which is related to the estimated parahydrogen content at 30 K (R09).

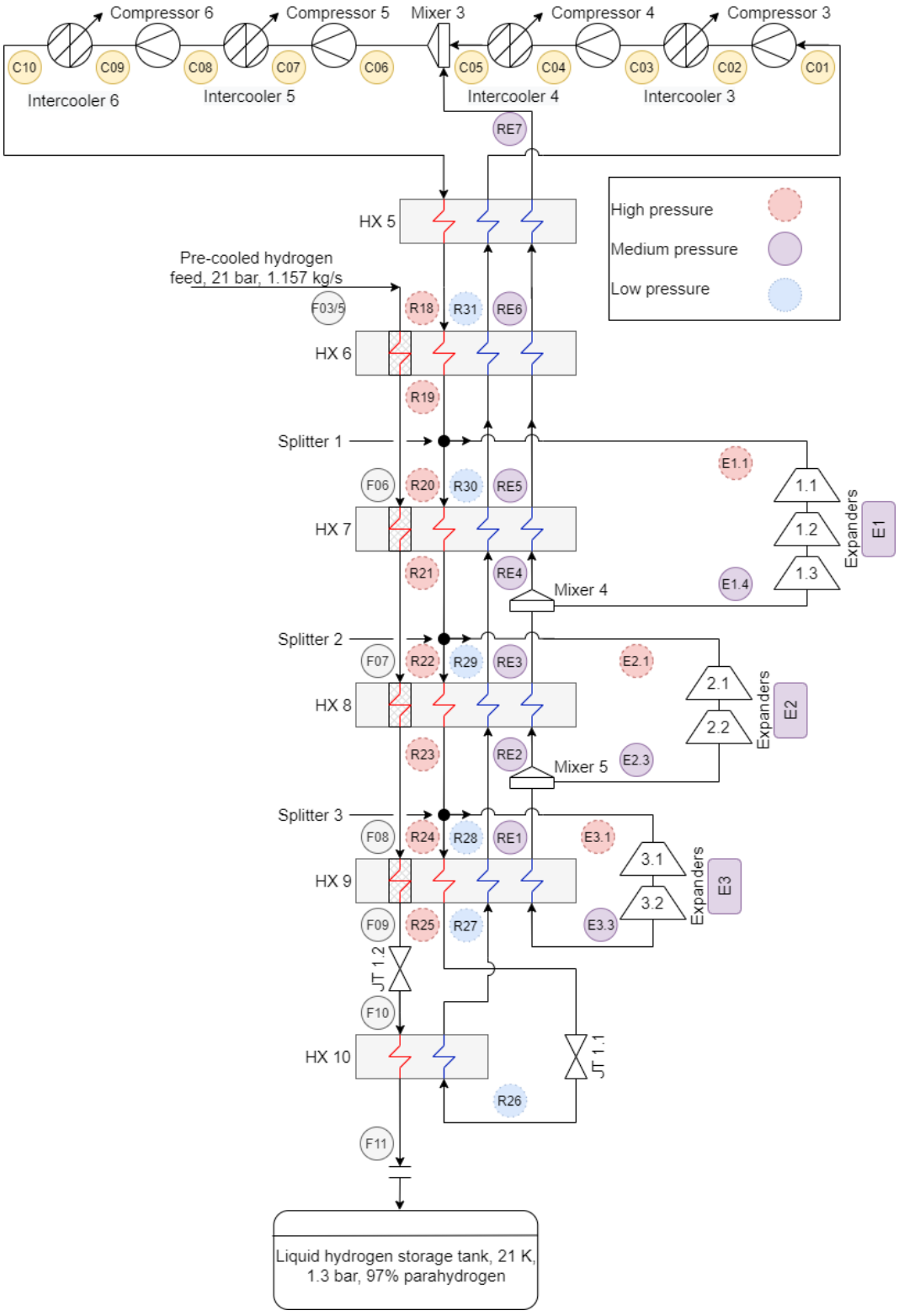

Figure 5.3: *The hydrogen Claude cycle configuration used for optimization.*

5.2 Process optimization

In order to optimize the refrigerant mixture composition in HYSYS, a stream for each selected component has to be defined and combined with the other refrigerant component streams, using a mixer as depicted in figure 5.4. The refrigerant composition in the steam leaving the mixer can be combined with a balance block that reads the molar- composition and flow rate. The output of the balance block is then selected to mirror the parameters on to the refrigerant stream (R01). By selecting the individual molar flow rate as optimization variables the MR composition is optimized.

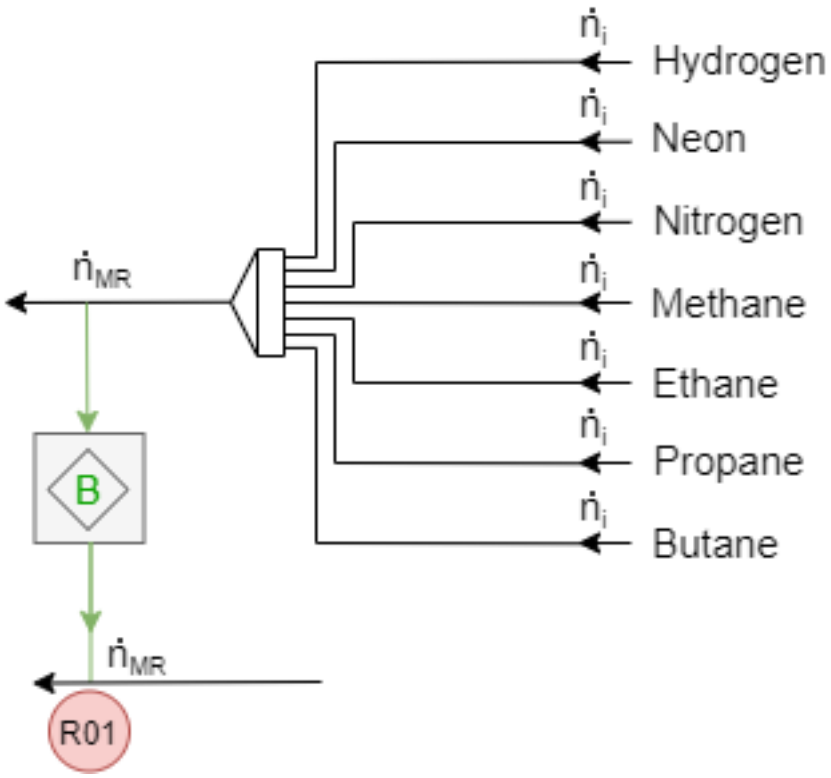

Figure 5.4: *The concept for optimizing a refrigerant mixture in Aspen HYSYS.*

For the optimization of the precoolings- and the hydrogen Claude-cycles, two optimization algorithms were used, the original HYSYS optimizer with the BOX scheme, which will be referred to as the BOX optimizer, and, the particle swarm optimizer (PSO) algorithm which is a global optimizer add-on for Matlab.

The PSO algorithm was selected for the main optimization procedure in this thesis. As the PSO is a Matlab add-on, the optimization algorithm is pre-defined, but it requires a written code in order to communicate with HYSYS, which was provided by the supervisors of the thesis.

A set of PSO parameters had to be determined, and the parameters are presented in table 5.2. In addition, the initial starting point, and upper- and lower boundaries must be selected. The objective function for the optimizations was to minimize the compressor work requirement in the refrigeration cycles. For the heat exchangers, the optimization constraints for MTA were set to equal 2 K, except for heat exchanger 10, which has an optimization constraint at 0.5 K. In addition, the vapor fraction at the inlet of the compressors and turbine expanders was to to equal 1 in order to ensure no liquid at the inlet.

Table 5.2: *The parameters used for the PSO algorithm. (n = number of variables)*

Parameters	**Value**
Swarm size	$n \cdot 10$
Function tolerance	$1.0 \cdot e^{-6}$
Max iteration	160
Max stall iteration	20

In order for the PSO to start converging towards an assumed global optimized point, the PSO algorithm must first find a solution that obeys the constraints. As the range of the determined higher boundaries (HB) and lower boundaries (LB) was set relatively wide, it was difficult for the PSO to find a starting point. This was solved by utilizing the BOX optimizer as it has been found from the author's past experience to find a solution relatively quick. The BOX optimizer is a local optimizer, and the result is highly dependent on the initial starting point and will mostly converge quickly, but at a point far from the global optimum. The results obtained from the BOX optimizer was then used as initial starting points for the corresponding optimization variables in the PSO algorithm. Generally, if the optimization results were constrained by, or close to the boundaries, the optimization procedure was conducted again adjusting the higher- and lower boundaries accordingly. The precooling optimization variables for case 1 and 2 are presented in table 5.3, along with the HB and LB utilized for the PSO optimizer. It is worth noting that the algorithm used to establish communication between Matlab and HYSYS requires the temperature and pressure to be specified as $[^{\circ}C]$ and $[kPa]$.

Table 5.3: *Optimization variables for case 1 and 2, for each precooling temperature.*
[1] *Case 1.*
[2] *Case 2.*

Precooling temperature		**80 K**[2]		**90 K**[2]		**100 K**[2]		**110 K**[1]		**120 K**[1]	
Variable	**Unit**	**LB**	**HB**	**LB**	**HB**	**LB**	**HB**	**LB**	**HB**	**LB**	**HB**
P_L	$[kPa]$	100	1000	100	1000	100	1000	100	900	100	900
P_H	$[kPa]$	1000	3500	1000	3500	1000	3500	1000	2700	1000	2700
T_{F02}	$[°C]$	-10	25	-10	25	-10	25	-90	0	-90	0
T_{F03}	$[°C]$	-120	-50	-120	-50	-120	-50	-	-	-	-
T_{F04}	$[°C]$	-170	-80	-160	-80	-150	-80	-	-	-	-
$\dot{m}_{H_2}$	$[\frac{kg}{s}]$	0	3	0	3	0	3	-	-	-	-
$\dot{m}_{Ne}$	$[\frac{kg}{s}]$	0.3	3	0.3	3	0.2	3	-	-	-	-
$\dot{m}_{N_2}$	$[\frac{kg}{s}]$	0	10	0	10	0	10	0	25	0	25
$\dot{m}_{CH_4}$	$[\frac{kg}{s}]$	0	15	0	15	0	15	1	10	1	10
$\dot{m}_{C_2H_6}$	$[\frac{kg}{s}]$	1	15	1	15	1	15	0	12	0	12
$\dot{m}_{C_3H_8}$	$[\frac{kg}{s}]$	0	5	0	5	0	5	0	10	0	10
$\dot{m}_{C_4H_{10}}$	$[\frac{kg}{s}]$	5	25	5	25	5	25	4	15	4	15

Table 5.4 presents the optimization variables used for the hydrogen Claude cycle. After multiple optimization iterations, the lower pressure was mostly constrained at 100 kPa, therefor the lower pressure optimization variable was excluded for the final optimization in order to reduce the number of variables. Due to the utilization of reciprocating compressors in the hydrogen Claude cycle, HYSYS required the flow rate to be specified as molar flow rate.

Precooling temperature		**80 K**[2]		**90 K**[2]		**100 K**[2]		**110 K**[1]		**120 K**[1]	
Variable	**Unit**	**LB**	**HB**	**LB**	**HB**	**LB**	**HB**	**LB**	**HB**	**LB**	**HB**
P_H	[kPa]	1000	2000	1000	3500	1500	3500	1500	3500	1000	3000
P_M	[kPa]	200	900	100	1500	100	1500	100	1500	100	1000
$\dot{n}_{C01}$	$[\frac{mol}{s}]$	0.1	2	0.1	2	0.1	2	0.1	2	0.1	2
T_{C01}	$[°C]$	22	26	0	26	0	26	0	26	0	26
T_{F06}	$[°C]$	-210	-175	-210	-175	-210	-170	-210	-153	-210	-153
T_{F07}	$[°C]$	-225	-190	-215	-185	-215	-178	-215	-158	-215	-158
T_{F08}	$[°C]$	-235	-200	-235	-205	-225	-185	-225	-165	-225	-165
T_{R11}	$[°C]$	-245	-215	-245	-210	-240	-193	-240	-210	-240	-210
T_{R12}	$[°C]$	-240	-205	-235	-185	-235	-193	-235	-205	-235	-205
T_{R13}	$[°C]$	-220	-183	-210	-178	-210	-178	-210	-150	-210	-150
T_{R14}	$[°C]$	-220	-175	-220	-175	-220	-173	-220	-150	-220	-150
Splitter 1		0.05	0.5	0.1	0.5	0.1	0.5	0.1	0.5	0.1	0.5
Splitter 2		0.1	0.7	0.15	0.5	0.15	0.4	0.15	0.4	0.1	0.6
Splitter 3		0.4	0.95	0.5	0.95	0.5	0.95	0.5	0.95	0.5	0.95

Table 5.4: *Optimization variables for the hydrogen Claude cycle, for each precooling temperature.*

5.3 Exergy analysis

By applying equation 3.6 for the total exergy loss (Δex) to the component boundaries, results in the equations presented in table 5.5, along with the exergy efficiency (η_{ex}) for compressors and expanders. The total exergy loss were calculated by summing up the individual exergy loss for each component (i) utilizing equation 5.2.

$$\Delta ex_{tot} = \sum_i \Delta ex_i \tag{5.2}$$

Table 5.5: *Equation used for the exergy analysis for each component in the refrigeration cycles*

Compressor		
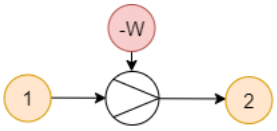	$\Delta ex = \dot{n}_1(ex_1 - ex_2) - (-\dot{W})$	(5.3)
	$\eta_{ex} = \dfrac{\dot{n}_1(ex_1 - ex_2)}{-\dot{W}}$	(5.4)
Expander		
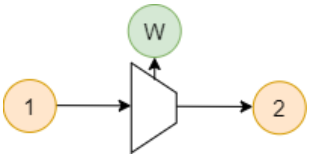	$\Delta ex = \dot{n}_1(ex_1 - ex_2) - (\dot{W})$	(5.5)
	$\eta_{ex} = \dfrac{\dot{W}}{\dot{n}_1(ex_1 - ex_2)}$	(5.6)
Intercooler		
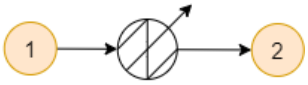	$\Delta ex = \dot{n}_1(ex_1 - ex_2)$	(5.7)
Throttling Valve		
	$\Delta ex = \dot{n}_1(ex_1 - ex_2)$	(5.8)
Phase separator		
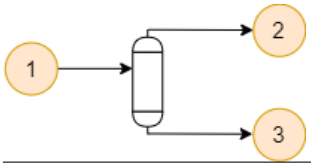	$\Delta ex = \dot{n}_1 ex_1 - (\dot{n}_2 ex_2 + \dot{n}_3 ex_3)$	(5.9)
Mixer		
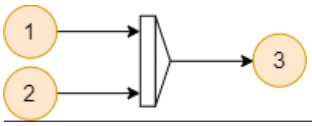	$\Delta ex = \dot{n}_1 ex_1 + \dot{n}_2 ex_2 - \dot{n}_3 ex_3$	(5.10)
Heat exchanger		
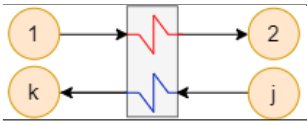	$\Delta ex = (\dot{n}_1 ex_1 + ...\dot{n}_j ex_j) - (\dot{n}_2 ex_2 + ...\dot{n}_k ex_k)$	(5.11)

The standard chemical exergy used for chemical exergy calculation was obtained from ref. [41] and is presented in table 5.6.

Table 5.6: *Standard chemical exergy, $\bar{e}^0$. [41]*

Component	$\bar{e}^0$ $[\frac{kJ}{kmol}]$
Hydrogen	$236.10 \cdot 10^5$
Neon	$2716.00 \cdot 10^4$
Nitrogen	$720.00 \cdot 10^0$
Methane	$831.65 \cdot 10^5$
Ethane	$1495.84 \cdot 10^6$
Propane	$2154.00 \cdot 10^6$
Butane	$2805.80 \cdot 10^6$

The SEC for the precooling and Claude cycle was calculated by applying equation 5.12 to the system boundaries.

$$SEC_{\text{SMR or Claude}} = \frac{-W_{tot,(\text{SMR or Claude})}}{\dot{m}_{F01} \cdot 3600} \tag{5.12}$$

The overall exergy efficiency (η_{ex}) for the precooling is calculated with equation 5.13.

$$\eta_{ex,SMR} = \frac{\dot{W}_{rev,SMR}}{-\dot{W}_{tot,SMR}} = \frac{\dot{n}_{F01}(ex_{FO3/5} - ex_{FO1})}{-\dot{W}_{tot,SMR}} \tag{5.13}$$

The exergy efficiency for the hydrogen Claude cycle was calculated with equation 5.14. This equation was used due to the change in EOS at stream F09.

$$\eta_{ex,Claude} = \frac{\dot{W}_{rev,Claude}}{-\dot{W}_{tot,Claude}} = \frac{\dot{n}_{F01}\Big((ex_{FO9} - ex_{FO3/5}) + (ex_{F11} - ex_{F09})\Big)}{-\dot{W}_{tot,Claude}} \tag{5.14}$$

Results & Discussion

This chapter includes the optimized results and assessments of the optimization procedure for the precooling- and hydrogen Claude-cycle, which will be discussed in the two following subsections. Consecutively, an exergy analysis which suggest potential improvements for the optimal precooling temperature configuration, will be presented.

6 SMR precooling cycles

Figure 6.1 depicts the optimized precooling cycle SEC for the whole precooling temperature range, for case 1 and 2. The results in figure 6.1 can be compared to some extent. However, comparing different cycles and optimization results can be challenging due to the difficulty of finding an absolute optimal point in a highly non-linear optimization search field. This is assumed to be indicated to some extent by comparing the line-profile for each case. Case 1 has less optimization-variables and -constraints compared to case 2. This might be one of the reasons for the slight fluctuation in the SEC-profile for case 2, relative to case 1. The reason for selecting the presented result data points, in figure 6.1, are discussed in the next subsection.

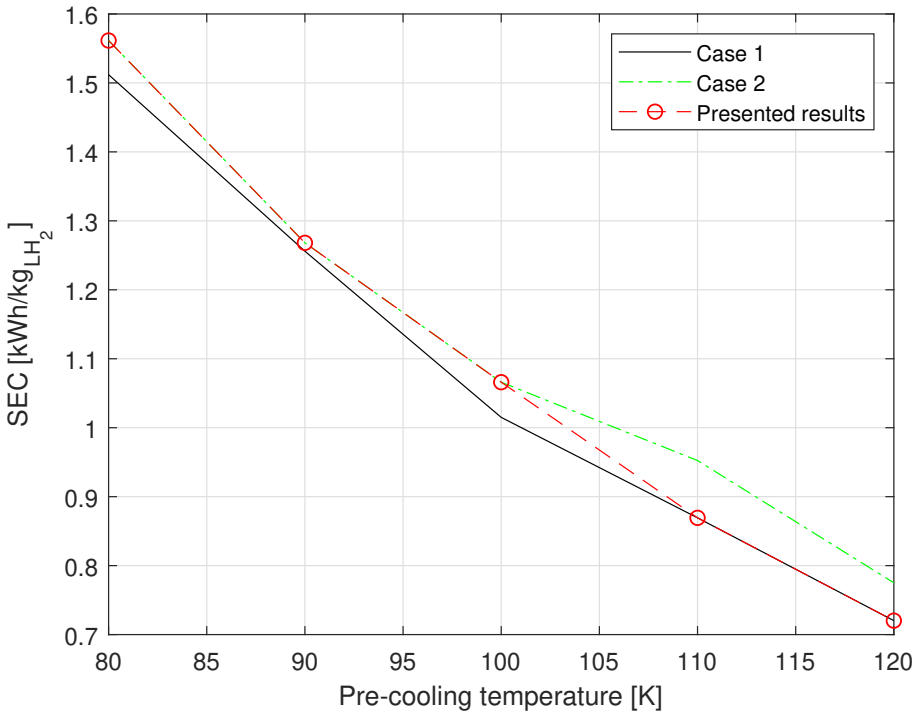

Figure 6.1: *SEC for the whole precooling temperature range for, case 1 and 2, and an indication of the presented results.*

.

6.1 Solid-liquid equilibrium: Refrigerant mixture

As stated in the literature review, the general rule for designing a refrigeration cycle is that the freezing point for each refrigerant component should be lower than the lowest temperature in the refrigeration cycle, in order to prevent the possibility of refrigerant freeze-out. However, this would limit the possibility of using most of the high boilers in the 80 K and 90 K precooling temperatures. This will decrease the total precooling exergy efficiency due to the refrigerant properties related to the high boilers. By including a certain degree of phase separation, this statement can to some extent be fulfilled.

From table 6.1 it can be seen that there is no butane present at the lowest temperatures in the case 2 precooling cycles, hence no risk of butane freeze-out. The quantity of ethane in R12 is relatively small and is neglected in terms of freezing probability. However, there are significant amounts of methane, which could be at risk of freezing in the 80 K- and 90 K-precooling cycles as the stream R12 temperatures, is below methane's freezing point. For the 90 K precooling

temperature, the minimum temperature, T_{min}, for stream R12 in table 6.2, is about 4-5 K below methane's freezing point. This is deemed acceptable, as some freezing point depression is assumed to occur. For the 80 K precooling temperature, the gap between the freezing point for methane relative to, T_{min}, is about 15 K. This increases the freeze-out probability. In addition, the 100 K precooling temperature shows no sign of freeze-out risk, based on comparing the individual component freezing points, and T_{min} in stream R12.

In terms of the approximately 14%mole butane for 110 K and 120 K, in table 6.1, it seems reasonable to argue that butane is at risk of freezing. However, butane has been found to be commonly utilized in LNG SMR cycles which has a cold end temperature at approximately 110 K. Also, in the reviewed literature on SMR precooled liquid hydrogen concepts, butane has been commonly used as a refrigerant component at these temperatures. Therefore it is assumed that utilizing case 1 for 110 K and 120 K is acceptable, in order to have a sufficiently low probability of refrigerant freeze-out.

Table 6.1: *Shows the molar fraction for the optimized refrigerant mixtures in the lowest temperature stream, for the SMR precooling cycles.*

Precooling temperature	**80 K**[2]	**90 K**[2]	**100 K**[2]	**110 K**[1]	**120 K**[1]
Stream	**R12**	**R12**	**R12**	**R09**	**R09**
Hydrogen	0.093	0.022	0.000	-	-
Neon	0.103	0.111	0.058	-	-
Nitrogen	0.396	0.359	0.334	0.102	0.107
Methane	0.397	0.486	0.573	0.369	0.336
Ethane	0.012	0.022	0.035	0.339	0.416
Propane	-	-	-	0.047	0.002
n-Butane	0.000	0.000	0.000	0.142	0.139

An estimated freezing point calculations have been conducted and can be seen in table 6.2, along with T_{min} which is related to each refrigerant composition. Also, the table presents the temperature difference, ΔT, between the estimated freezing point and T_{min}. The estimated freezing points have been calculated based on summarizing the individual mole fractions and freezing points, utilizing equation 3.8. This indicates that none of the precooling temperatures are affected by refrigerant freeze-out, as all ΔT are at a positive value. These are rough assumptions and estimations as previously stated in the literature review, and future analysis must be performed for a thorough freeze-out risk assessment.

Table 6.2: *The lowest temperature (T_{min}) experienced by the different refrigerant composition in each case, an estimated freezing point, and the temperature difference (ΔT) between T_{min} and the estimated freezing points.*

Precooling temperature	**120K**[1]		**110K**[1]		**100K**[2]		
Stream	**R09**	**R11**	**R09**	**R11**	**R12**	**R14**	**R16**
T_{min} [K]	116.9	217.9	106.2	221.5	107.2	167.3	236.1
Estimated freezing point [K]	94.1	100.1	94.1	101.4	84.2	89.0	96.3
ΔT [K]	22.8	117.8	12.1	120.1	23.0	78.3	139.8
Precooling temperature	**90K**[2]			**80K**[2]			
Stream	**R12**	**R14**	**R16**	**R12**	**R14**	**R16**	
T_{min} [K]	86.0	135.9	173.6	75.9	121.6	164.0	
Estimated freezing point [K]	72.0	88.0	94.9	66.1	85.6	94.1	
ΔT [K]	14.0	47.9	78.7	9.9	36.1	69.8	

6.2 Optimization results

From the results shown in table 6.3, it can be observed that the SEC is decreasing with higher precooling temperatures, as expected. One reason for the slight non-linearity between the precooling temperature SEC and exergy efficiency might be attributed to the effect of ortho-para hydrogen conversion, as it becomes more predominant at lower temperatures. Or, that lower precooling temperatures require more N_2, Ne and/or H_2 to produce sufficient throttling effect. In addition, exergy losses increase at lower temperatures, as seen in table 6.4. On the other hand, the reversible work does also increase. The largest deviation for the MTA is related to HX 1, in the 100 K precooling temperature. Although an MTA of 4.84 K is relatively large compared to the target of 2 K, the possible improvement related to the exergy loss is less significant, as the total exergy loss related to HX 1 is 2.25% of the total irreversibilities. Also, a small deviation of 0.28 K relative to 2 K, can be observed for HX 3 at 80 K, although the performance increase is assumed to be negligible if improved. Overall, the optimization results obtained for the precooling cycle seem to be in coherence with the reviewed literature. Although comparing different precooling cycles, especially from literature is difficult, due to the difference in refrigerant cycle configuration, accounting for ortho-para hydrogen conversion in the precooling cycle, and multiple-optimizations and -input parameters, etc.

Table 6.3: *Performance indicators for the SMR precooling cycles.*

Precooling temperature	**80 K**[2]	**90 K**[2]	**100 K**[2]	**110 K**[1]	**120 K**[1]	**Unit**
Compressor Work ($-\dot{W}$)	6506.2	5283.8	4441.0	3622.1	3001.0	$[\frac{kJ}{s}]$
Reversible work ($\dot{W}_{rev}$)	2696.6	2260.0	1903.0	1609.0	1365.7	$[\frac{kJ}{s}]$
Exergy efficiency (η_{ex})	41.45	42.77	42.85	44.42	45.51	$[\%]$
SEC	1.56	1.27	1.07	0.87	0.72	$[\frac{kWh}{kg_{H_2}}]$
MTA						
HX 1	2.00	2.01	4.84	1.99	2.00	$[K]$
HX 2	2.00	2.00	2.00	2.00	2.00	$[K]$
HX 3	2.28	2.04	2.00	-	-	$[K]$
HX 4	2.00	2.00	2.01	-	-	$[K]$
LMTD						
HX 1	7.67	7.85	10.97	5.76	3.71	$[K]$
HX 2	3.89	3.40	3.11	3.32	3.09	$[K]$
HX 3	5.13	3.73	3.05	-	-	$[K]$
HX 4	2.80	3.13	3.92	-	-	$[K]$

Although the PSO optimizer is considered to be a global optimizer, the optimization process is subjected to several issues which can result in a deviation between the optimized and ideal solution, these are: initial starting point values, number of variables, selection of variables, lower- and higher-boundary range, particle swarm size, sufficient number of iterations, maximum stall iterations, tolerance level, and number of constraints.

Using the BOX optimizer to find a rough starting point for the PSO seems to be a reasonable method as multiple PSO optimizations have been performed with minor result-deviation, between the iterations. Also, the results show an expected gradient between the SEC for the consecutive precooling temperature, especially for case 1, as illustrated in figure 6.1. Even though the higher- and lower-boundaries for the PSO optimizer were adjusted, if the final results were indicated to be limited or close to the optimization boundaries, the boundary limits might affect the final result due to the mechanics of the PSO algorithm. The PSO optimizer seems to obtain consistent results for a relatively small number of variables.

The number of variables are mostly dependent on the configuration, generally increasing with more equipment, exponentially creating a highly non-linear optimization search field. For case 1, neon and hydrogen were not included as optimization variables for the 110 K and 120

K precooling temperatures, as the initial optimization results only showed trace amounts in the order of 10^{-4}kg. Further reduction of variables for the whole precooling temperature span could be: either to use neon or hydrogen as the low boiler, remove propane as preliminary- and final-optimizations showed zero flow rate. Reduction of optimization variables might be more important with an increased number of variables, such as for case 2 relative to case 1. This is possibly indicated by: the slight fluctuation in SEC for case 2 as is illustrated in figure 6.1, the difference between the resulting MTA in table 6.3 and the 2 K optimization constraint, as case 1 have an approximately perfect match relative to case 2.

Generally, the particle swarm size was selected based on the number of variables. A larger swarm size and number of iterations can improve the optimization results. Optimization with increased particle swarm size and number of iterations relative to the parameters presented in the method section was conducted, but with little to no improvements. As swarm size and number of iterations increase the computational time, the initial parameters were retained. A typical optimization convergence for this thesis is depicted in figure 6.2.

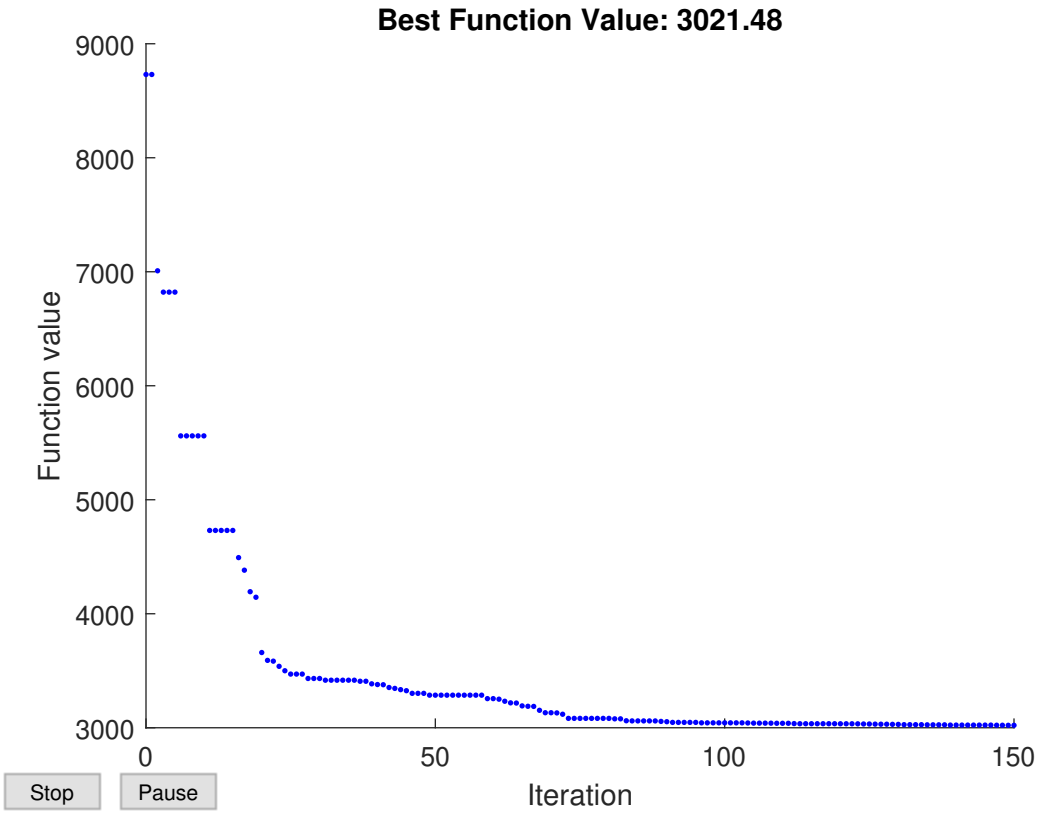

Figure 6.2: *A general optimization procedure converging to a optimal result for the PSO optimizer.*

The PSO optimization process has not been found to be limited by the maximum stall iterations, and is mostly stopped by the number of iterations. Most likely there is a better result beyond the 150 iterations, but the decrease in energy consumption beyond this point is assumed to be limited. Based on the final result the tolerance level is found to be acceptable, as none of the MTA constraints is $< 1.99K$.

The exergy losses for the SMR precooling cycles are presented in table 6.4. By observing how the component's exergy losses are evolving throughout the precooling temperature span, it seems like the exergy losses change in a relatively linear fashion between the individual components which is believed to indicate relatively good optimization results. Some discrepancy in the exergy loss evolution is seen at the interface between case 1 and 2, which is natural since these are two different configurations.

Table 6.4: *The exergy losses for each component of the SMR precooling cycle.*

	Exergy loss $[\frac{kJ}{s}]$				
Precooling temperature	**80 K**[2]	**90 K**[2]	**100 K**[2]	**110 K**[1]	**120 K**[1]
Compressor 1	548.1	464.1	401.5	315.7	270.7
Compressor 2	516.8	437.8	379.7	294.5	252.9
Intercooler 1	384.3	258.8	165.9	186.9	130.9
Intercooler 2	609.5	431.1	343.6	373.1	280.6
HX 1	28.5	37.9	51.2	180.1	71.8
HX 2	507.9	365.6	290.7	506.9	452.3
HX 3	342.8	253.3	207.4	-	-
HX 4	209.8	231.7	268.1	-	-
Separator 1	0.00	0.00	0.00	0.00	0.00
Separator 2	0.00	0.00	0.00	-	-
Mixer 1	11.0	7.6	4.9	2.4	27.1
Mixer 2	129.1	147.0	161.2	-	-
JT 1	290.4	189.4	91.6	38.9	27.5
JT 2	157.8	141.6	123.3	114.6	121.5
JT 3	73.9	57.8	49.5	-	-
Sum	3809.6	3023.9	2538.0	2013.2	1635.2

7 Hydrogen Claude cycle

7.1 Optimization results

The optimized results for the hydrogen Claude cycle are presented in table 7.1. The compressor work, reversible work, and SEC are increasing with a broader temperature span, as expected. However, a more or less linear relationship was expected for the SEC, but it is fluctuating, hence also the other parameters depicted in figure 7.1. This is believed to be due to an insufficient optimization procedure, where the number of iteration and particle swarm size might be the reason for the assumed discrepancy. Ideally, it is believed that the individual exergy losses should increase in a more or less linear fashion, similar to the individual exergy loss evolution seen in table 6.4, for the precooling cycle. Deviations related to a insufficient optimization procedure might have been apparent if the precooling temperature resolution was higher.

Table 7.1: *Performance indicators for the hydrogen Claude cycle.*

Precooling temperature	**80 K**	**90 K**	**100 K**	**110 K**	**120 K**	**Unit**
Compressor work ($-\dot{W}$)	23069.2	23980.7	25725.6	26490.7	28104.8	$[\frac{kJ}{s}]$
Expansion work ($\dot{W}$)	1921.2	2099.0	2257.0	2421.5	2750.7	$[\frac{kJ}{s}]$
Reversible work ($\dot{W}_{rev}$)	7347.7	7794.6	8183.7	8471.4	8697.2	$[\frac{kJ}{s}]$
Exergy efficiency (η_{ex})	34.74	35.62	34.87	35.20	34.30	[%]
SEC	5.54	5.76	6.18	6.36	6.75	$[\frac{kWh}{kg_{LH_2}}]$
MTA						
HX 5	1.99	2.02	2.00	2.13	2.01	$[K]$
HX 6	4.87	5.08	5.20	2.35	4.78	$[K]$
HX 7	3.20	4.97	3.84	2.30	2.02	$[K]$
HX 8	2.00	2.01	2.08	2.08	2.04	$[K]$
HX 9	2.00	2.00	2.00	2.02	2.01	$[K]$
HX 10	0.55	0.54	0.91	0.91	0.91	$[K]$
LMTD						
HX 5	2.75	2.75	2.85	2.85	3.06	$[K]$
HX 6	5.11	5.24	5.42	2.85	4.95	$[K]$
HX 7	4.40	5.56	4.81	3.97	2.32	$[K]$
HX 8	2.29	2.43	2.98	2.42	2.37	$[K]$
HX 9	2.54	2.56	2.63	2.66	2.70	$[K]$
HX 10	0.91	0.91	0.92	0.92	0.92	$[K]$

One reason might be indicated by the temperature deviation of MTA (HX 6 and 7) from the 2 K optimization constraints, as seen in table 7.1. As the optimal solutions are assumed to be an MTA equal to 2 K, the optimization procedure was conducted again, with increased optimization iterations and particle swarm size, in order to correct these deviations, but the deviation prevailed. There might be several other reasons, e.g.: the method for selecting the optimization variables, a relatively high number of optimization-variables and -constraints, the variable heat capacity of equilibrium hydrogen in the cryogenic region.

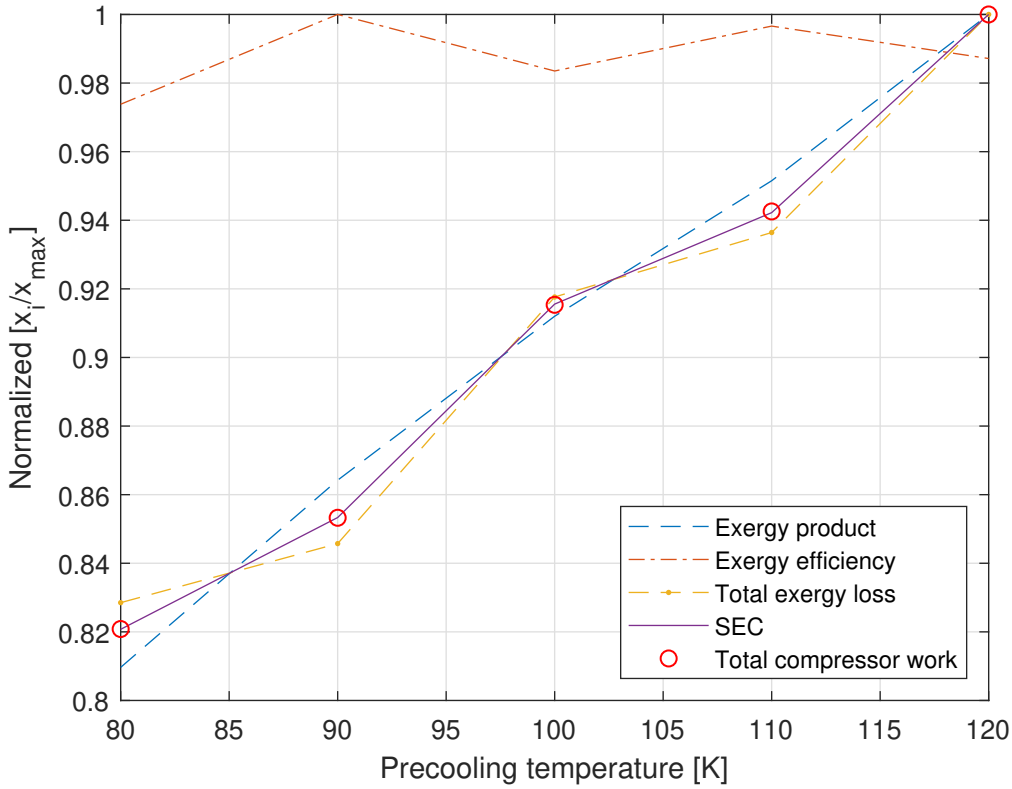

Figure 7.1: *Indication of the variation of exergy- product, -efficiency, and -loss; and SEC and compressor work, for the hydrogen Claude cycle. The values is normalized (each value is divided on its highest value)*

After inspecting the different optimization models in HYSYS it became apparent that the 110 K precooling temperature had a slightly different setup for the optimization variables. The temperatures for the hot streams into HX 6 were selected to be equal to each other (110K), while the cold side streams out of HX 6 were set equal for the other precooled temperatures. This might explain why the MTA is closer to 2 K for the 110 K temperature, and the fluctuating exergy losses in between 100 K and 120 K. After comparing the equilibrium hydrogen model heat capacity to the exergy efficiency fluctuation, it became apparent that it seems to be a correlation between these fluctuations, as depicted in figure 7.2.

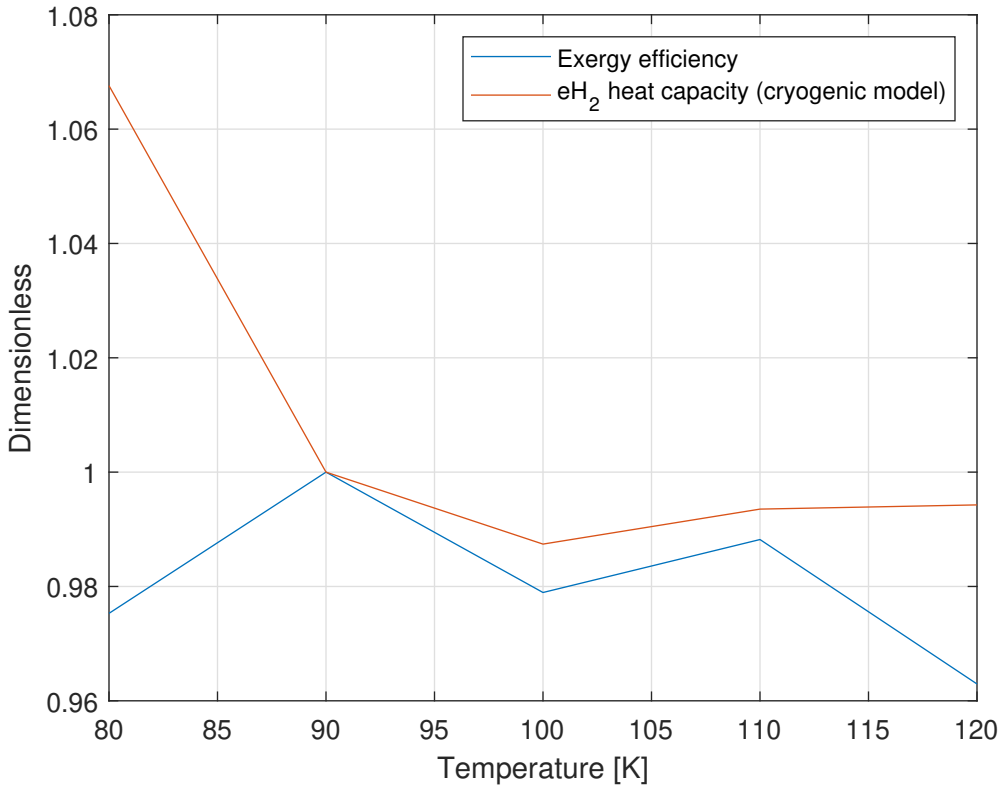

Figure 7.2: *Shows the correlation between the exergy efficiency fluctuations and the fluctuating equilibrium hydrogen heat capacity in the precooling temperature range.*

It might be worth noting that the adopted hydrogen Claude cycle configuration was originally used to cool the feed hydrogen from 117.9 K to saturated liquid, in the reference case. This might indicate that the Claude cycle configuration is better tailored to cool the latter temperature span, and that the hydrogen Claude cycle configuration should be tailored to the heat capacity profile in order to achieve optimum performance, for each precooled temperature.

By comparing the optimized results for the precooling cycle in context to the hydrogen Claude-cycle, the optimal precooling temperature in the MR precooled hydrogen Claude cycle can be obtained, which will be presented in the next section.

Table 7.2: *Exergy losses within the hydrogen Claude cycle, for each precooling temperature.*

	Exergy loss $[\frac{kJ}{s}]$				
Precooling temperature	**80 K**	**90 K**	**100 K**	**110 K**	**120 K**
Compressor 3	56.9	52.2	72.2	54.7	172.2
Compressor 4	56.9	52.2	72.3	54.7	172.4
Compressor 5	1288.4	1336.6	1394.3	1435.5	1491.4
Compressor 6	1292.6	1340.7	1399.9	1440.0	1498.1
Intercooler 3	47.1	38.7	59.9	33.1	191.3
Intercooler 4	53.5	44.7	68.9	39.1	224.9
Intercooler 5	1444.9	1552.6	1740.6	1906.9	1508.7
Intercooler 6	1518.9	1630.8	1822.1	1996.8	1590.2
HX 5	879.4	833.4	757.6	793.0	704.8
HX 6	241.2	132.5	167.8	38.8	271.6
HX 7	255.5	380.1	333.2	394.6	372.6
HX 8	1126.5	1268.4	835.7	717.8	778.7
HX 9	1887.9	1517.3	2487.6	2505.8	3419.0
HX 10	93.3	93.3	93.5	93.5	93.5
Mixer 3	0.0	0.0	0.1	0.1	0.1
Mixer 4	97.2	211.4	146.9	131.2	7.4
Mixer 5	0.7	2.3	29.3	0.0	2.1
Splitter 1	0.0	0.0	0.0	0.0	0.0
Splitter 2	0.0	0.0	0.0	0.0	0.0
Splitter 3	0.0	0.0	0.0	0.0	0.0
JT 1.1	314.5	307.7	423.3	385.2	827.0
JT 1.2	764.5	764.5	764.5	764.5	764.5
Expander 1.1	88.7	180.1	200.9	121.4	257.6
Expander 1.2	88.3	179.4	199.8	121.2	256.1
Expander 1.3	88.0	178.9	199.2	121.0	255.9
Expander 2.1	549.3	398.0	373.0	512.8	414.8
Expander 2.2	545.9	395.9	370.1	510.6	410.9
Expander 3.1	511.2	599.2	639.5	713.3	489.4
Expander 3.2	509.0	596.6	632.9	712.5	481.7
sum	13800.4	14087.2	15284.9	15597.8	16656.9

8 Exergy analysis: The optimal configuration

By combining the resulting SEC for the optimized precooling- and hydrogen Claude-cycle, and recovering the turbine work, results in an optimal precooling temperature located at 90 K, as presented in table 8.1. As previously indicated there are some uncertainties regarding the absolute optimized point for each result, also the resolution of the optimized precooling temperature range could potentially hide a solution lower than 6.52 kWh/kg_{LH_2}, but it is assumed to be concentrated around 90 K. By looking at the reversible work, a slight variation can be observed. Ideally, they should be equal, suggesting heat capacity discrepancy within the precooled temperature range.

Table 8.1: *Performance indicators for the total hydrogen liquefaction process.*
[3] *Expander work recovery.*

Precooling temperature	**80 K**	**90 K**	**100 K**	**110 K**	**120 K**	**Unit**
Total work requirement $(-\dot{W})^{[3]}$	27654.2	27165.5	27909.6	27691.3	28355.0	$[\frac{kJ}{s}]$
Total reversible work $(\dot{W}_{rev})$	10044.3	10054.6	10086.7	10080.4	10062.9	$[\frac{kJ}{s}]$
Total exergy efficiency $(\eta_{ex})^{[3]}$	36.32	37.0	36.1	36.4	35.5	[%]
Total exergy loss $(\Delta ex_{loss})^{[3]}$	17610.0	17111.1	17822.9	17611.0	18292.1	$[\frac{kJ}{s}]$
Total SEC [3]	6.65	6.52	6.70	6.65	6.81	$[\frac{kWh}{kg_{LH_2}}]$

In figure 8.1 the discrepancy between the specific heat capacity for the precooling- and cryocooling-equilibrium hydrogen model can be observed. This discrepancy should ideally not exist, but is a result the model-fitting between the two calculated- and regressed equilibrium hydrogen models. By optimizing the 90 K precooled hydrogen Claude cycle with a continuous equilibrium hydrogen model (from ambient to approximately 20 K) the results showed a significant improvement of SEC for the hydrogen Claude cycle. However, the exothermic ortho-para hydrogen conversion effect showed less temperature increase at the lower temperatures. Some compromises had to be made in order to have a fairly decent representation of the regressed equilibrium hydrogen model, due to the strong non-linearity of the enthalpy- and entropy-equilibrium hydrogen profile, at lower temperatures.

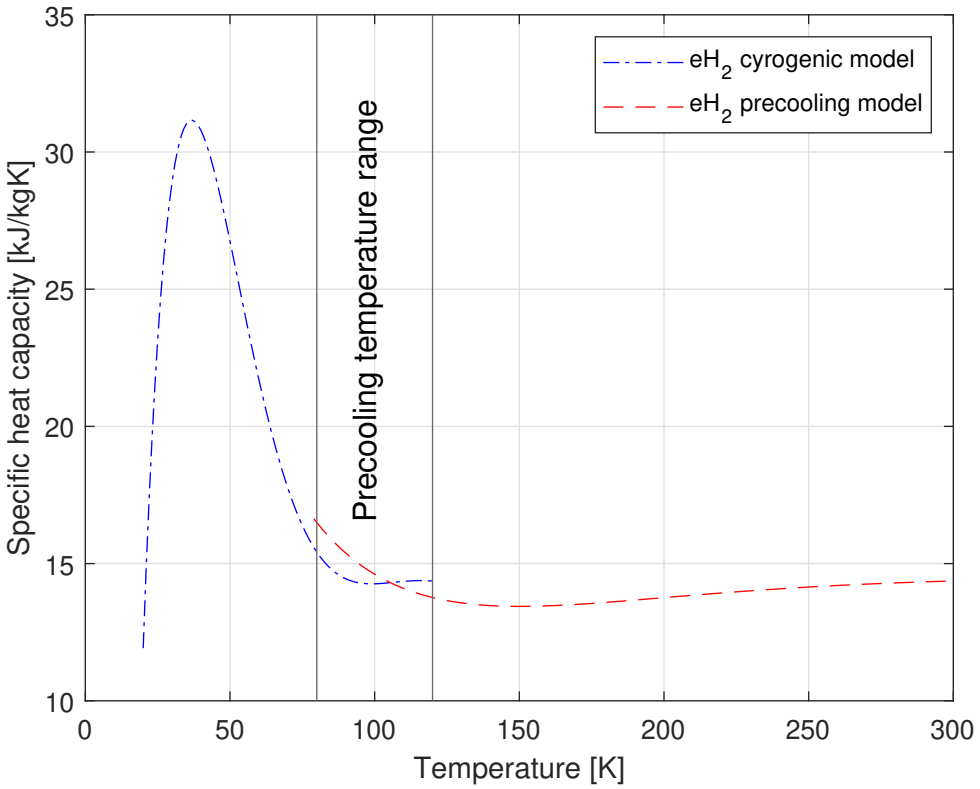

Figure 8.1: *Specific heat capacity at 21 bar for the regressed equilibrium hydrogen models.*

The fluctuating exergy efficiencies become more apparent when the expander work is recovered in the compressors, as indicated by the SEC profiles depicted in figure 8.2. By analyzing the specific exergy losses for each component, discrepancies in the refrigeration cycle configurations and optimization results can be revealed. Therefore an exergy analysis for the precooling- and hydrogen Claude-cycle is performed, in order to assess for improvements and further work. Assuming that the results in table 8.1 are the ideal optimized results, for each precooling temperature, exergy analysis is going to be presented for the 90 K precooling cycle configurations, in the following subsection.

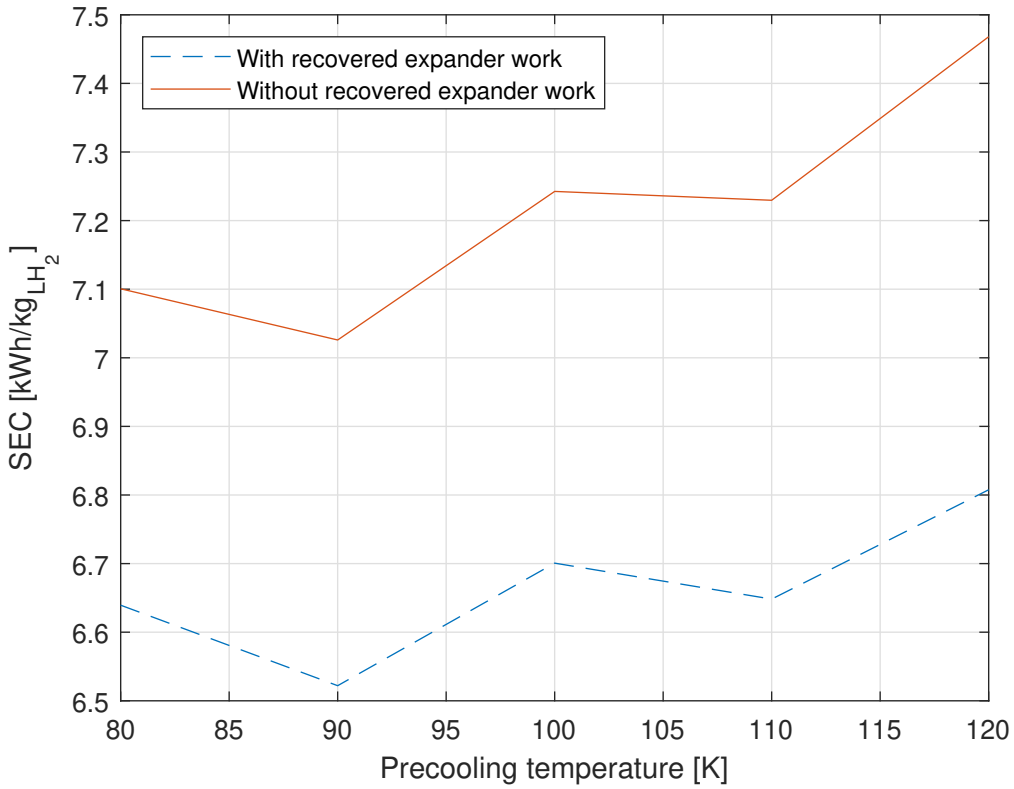

Figure 8.2: *SEC for the total hydrogen liquefaction process, and SEC when the expander turbine work is recovered in the compressors.*

8.1 90 K SMR precooling cycle

The total exergy losses in the 90 K SMR precooling cycle are at 3023.9 kJ/s. The total exergy losses for each component group are depicted in figure 8.3. This shows that the majority of losses are found in the heat exchangers, intercoolers, and compressors. The individual stream properties and exergy losses in the 90 K SMR precooling cycle are presented in table 8.3 and 8.2, along with the exergy loss percentage attributed to each component. The two tables will be discussed interchangeably for the component exergy analysis, which is systematically presented below.

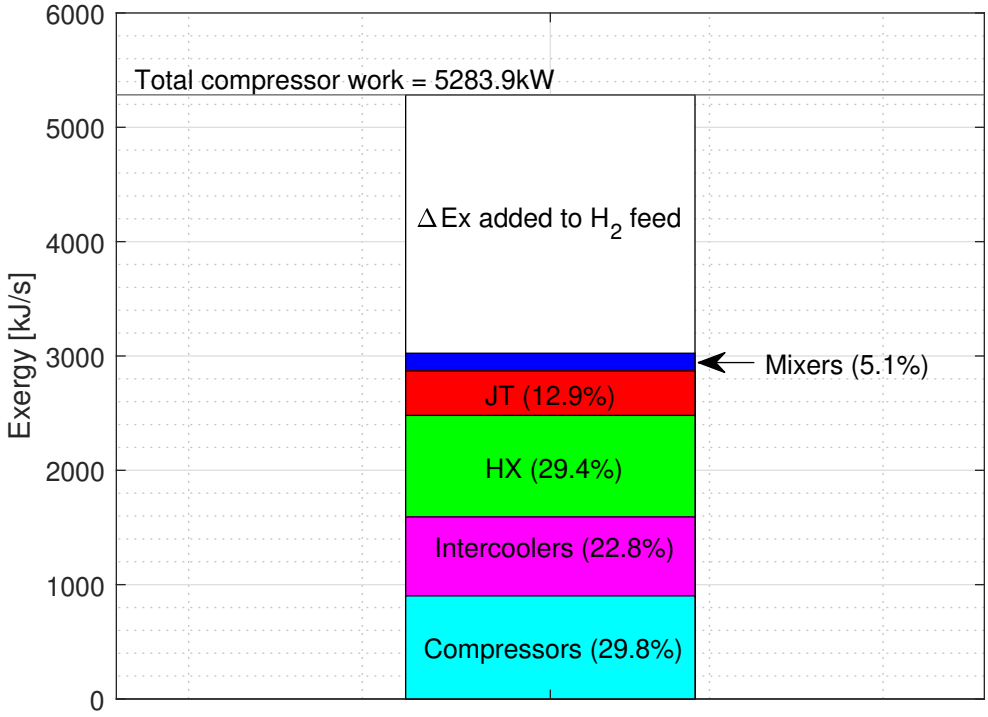

Figure 8.3: *Exergy losses for the component groups in the optimized 90 K SMR precooling cycle.*

Table 8.2: *Exergy losses for each component of the optimized 90 K SMR precooling cycle.*

Component	**Exergy loss** $[\frac{kJ}{s}]$	**Exergy loss [%]**
Compressor 1	464.1	15.35
Compressor 2	437.8	14.48
Intercooler 1	258.8	8.56
Intercooler 2	431.1	14.26
HX 1	37.9	1.25
HX 2	365.6	12.09
HX 3	253.3	8.38
HX 4	231.7	7.66
JT 1	189.4	6.26
JT 2	141.6	4.68
JT 3	57.8	1.91
Seperator 1	0.0	0.00
Seperator 2	0.0	0.00
Mixer 1	7.6	0.25
Mixer 2	147.0	4.86
Sum	3023.9	100.00

The exergy losses in compressor 1 and 2 are the largest single component contributor to the total exergy losses attributed in the SMR precooling cycle, at 29.8%. The exergy efficiency for compressors 1 and 2 is 82.8% and 83.0%, respectively. A slight decrease in exergy loss is observed for the second compressor, this is mostly related to the increased refrigerant pressure into compressor 2 relative to compressor 1, due to the equal pressure ratio at PR = 2.266, and the temperature variation between the input streams (F01 and F03) is more or less equal. The exergy loss in a compressor is strongly dependent on the isentropic efficiency and pressure ratio, as is depicted in figure 8.4. Reducing the pressure ratio and increasing the isentropic efficiencies would result in reduced exergy losses. The isentropic efficiency improvement is considered a design and manufacturing issue, but utilizing the correct isentropic efficiency will affect the total exergy efficiency to a certain degree. The pressure ratio can be reduced by adding several compressors. Although the cost assessment is not evaluated in this thesis, the associated cost might not be cost-efficient.

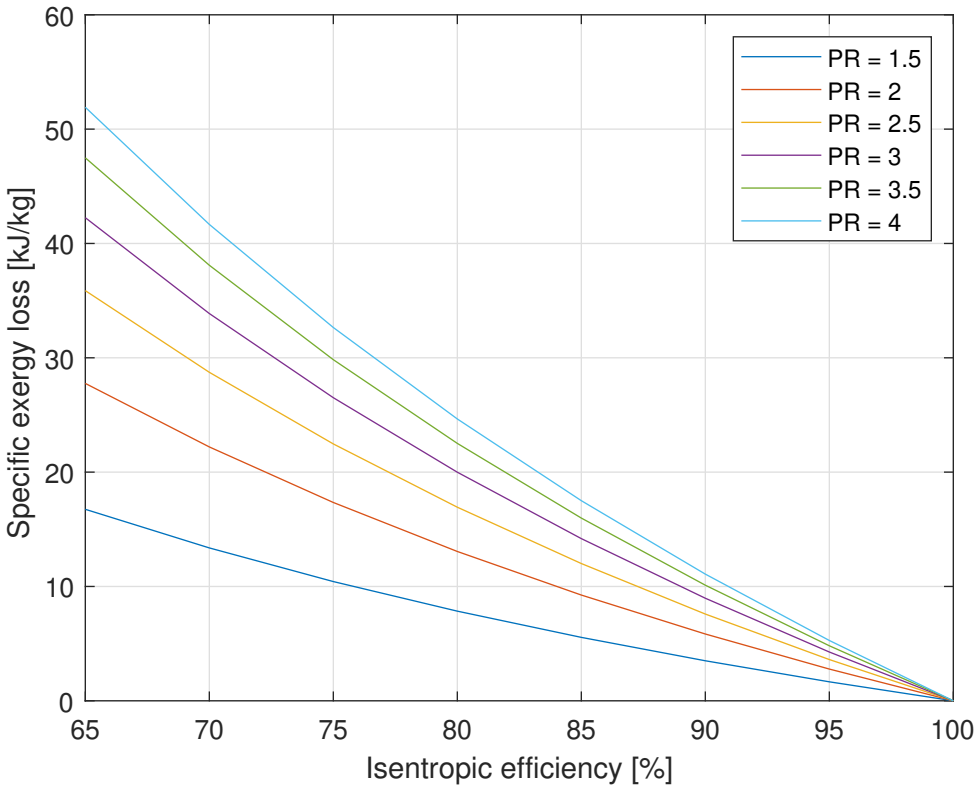

Figure 8.4: *Specific exergy loss for mixed refrigerant compression as function of isentropic efficiencies, with different pressure ratios.*

The combined intercooler exergy loss is attributed to 22.8% of the total exergy loss. The exergy loss is increasing from intercooler 1 to 2. It seems to be mainly two reasons for the difference in exergy loss: the refrigerant is cooled to the two-phase region, and the input pressure is increased between the two. As depicted in figure 8.5, the specific exergy losses do not seem to be heavily affected by pressure. However, as the temperature is gliding through the two-phase region, the specific exergy loss rate increase as is indicated by the change in slope gradient for 9 bar, 25 bar, and 33 bar, at 310 K, 320 K, and 330 K, respectively. The two-phase cooling seems to be the main reason for increased exergy losses, where the input-temperature and -pressure is the indirect reason for the increased exergy loss in intercooler 2.

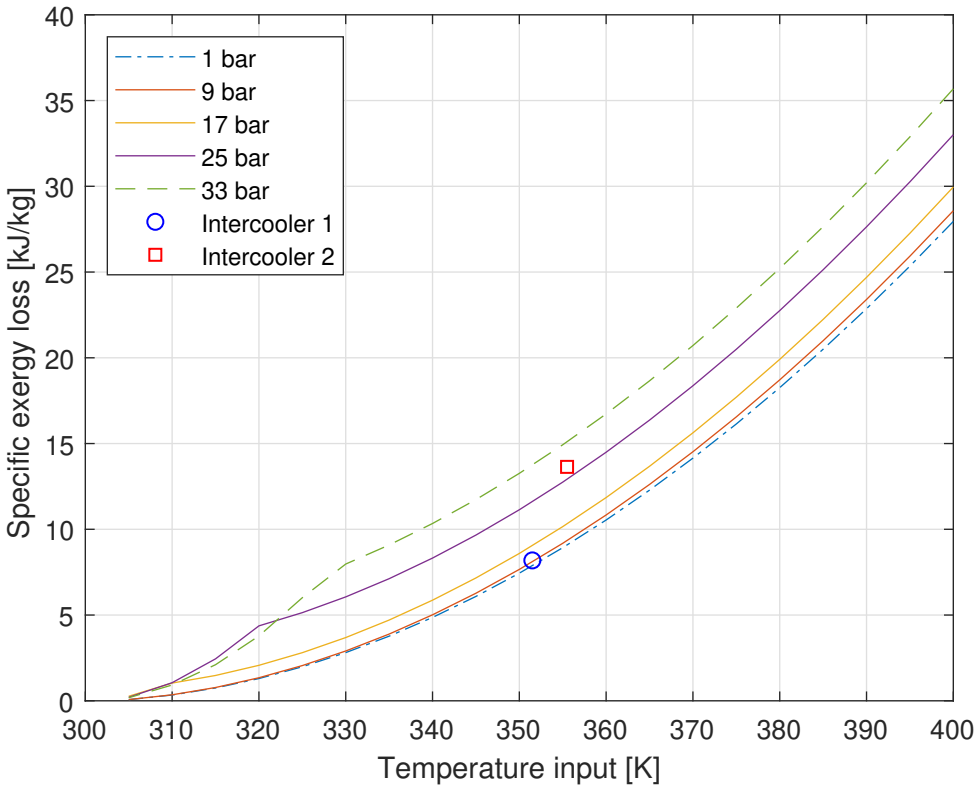

Figure 8.5: *Specific exergy loss attributed to mixed refrigerant intercoolers at different pressures, with varying input temperatures.*

The total exergy loss attributed to the SMR heat exchangers is 29.4% of the total exergy losses. The lowest irreversibilities can be seen in HX 1. Although the heat flow of HX 1 and HX 4 is about equal, and the LMTD is significantly higher for HX 1. The losses in HX 4 are about 6 times higher indicating that the exergy losses are more predominant at low temperature, and a close match between the composite curves in figure 8.6, is especially important at lower temperatures. The highest losses can be found in heat exchanger 2, but the heat flow is significantly higher than for the other heat exchangers. In total, the matching of the composite curves is seemingly close to optimal, but there are discrepancies between the temperatures at the interface of HX 2/HX 3 and HX 3/HX 4. This might be due to the temperature difference between two mixing streams, in between the heat exchangers. Another reason might be as the refrigerant composition changes at different temperature levels, it is difficult to obtain an ideal refrigerant composition/heat capacity, matching the hydrogen feed over the whole temperature span. This can result in temperature differences at the heat exchanger interface, caused by insufficient matching of the composite curve in the previous heat exchanger.

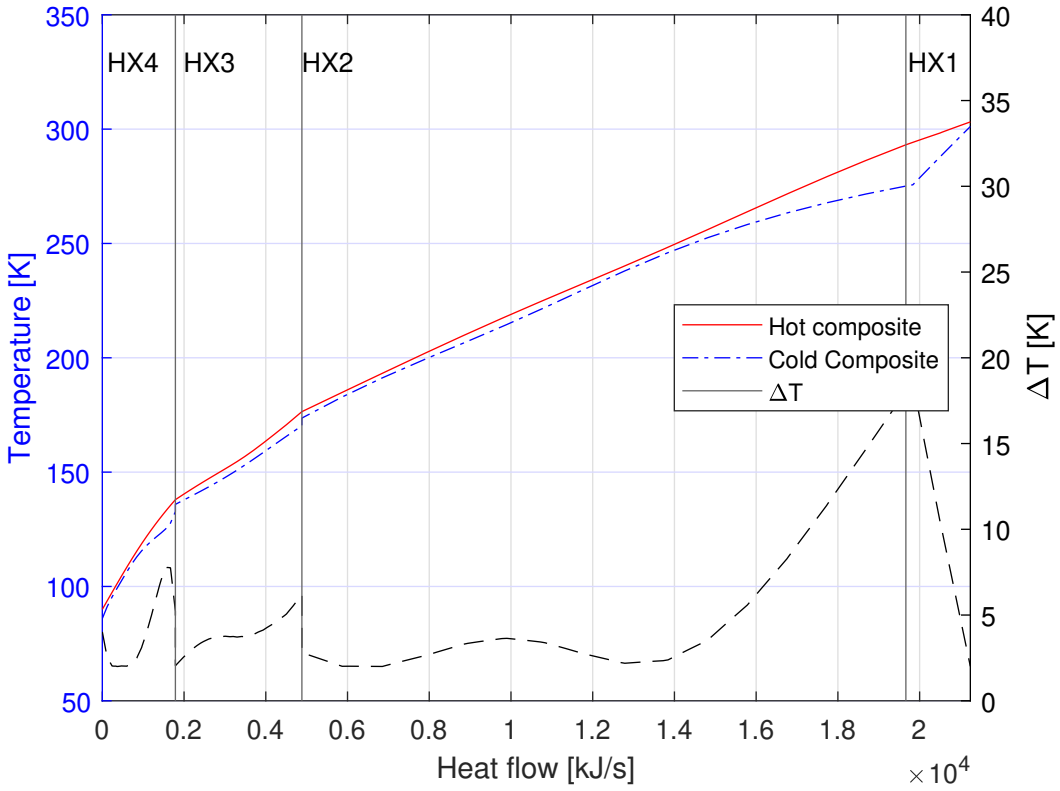

Figure 8.6: *Composite curves within the heat exchangers for the optimized 90 K SMR precooling cycle.*

12.9% of the total exergy losses are attributed to the three throttling valves. The inversion curves for the different refrigerant compositions varies as depicted in figure 8.7. The optimal stream input temperature is assumed to be at a the positive slope ($\mu_{JT} > 0$) close to $\mu_{JT} = 0$, for the individual refrigerant composition. Stream L02, at the JT 3 input, is at a negative slope, resulting in temperature increase over the throttling valve, this could be argued to be detrimental in a refrigeration cycle. Mainly, butane is assumed to be the main contributor to the temperature increase at this temperature level, due to butane's individual inversion temperature. An additional separator after intercooler 2 could be the solution in order to contain more of the butane at higher temperatures. However, a configuration with an additional separator and throttling valve was initially optimized, due to this reason. This resulted in two throttling valves with increasing temperatures, which had a negative impact on the SEC, relative to case 2. Due to multiple optimization iterations resulting in butane being a significant refrigerant contributor, it is assumed to be an important refrigerant component in order to achieve higher exergy efficiencies. The specific exergy loss over JT 1 seems to be excessively high, and is seemingly due to the presence of hydrogen and neon. The relatively high temperature decrease in JT 1 might be due to the need for hydrogen and neon, in order to compensate for the temperature increase related to the quantity of butane in stream L02. And, methane and

ethane in stream R11, as they are beyond their individual inversion curves ($\mu_{JT} < 0$). As the perfect separation of refrigerant components based on their condensation temperature is not possible due to solubility, achieving an ideal refrigeration mixture seems to be difficult, or not achievable as each component can have contradicting throttling effect relative to each other, dependent on the temperature and pressure at the throttling valve inlet. This might be one of the reasons for adopting MFC cycles, as it is possible to segregate or group the refrigerant components based on their inversion temperatures.

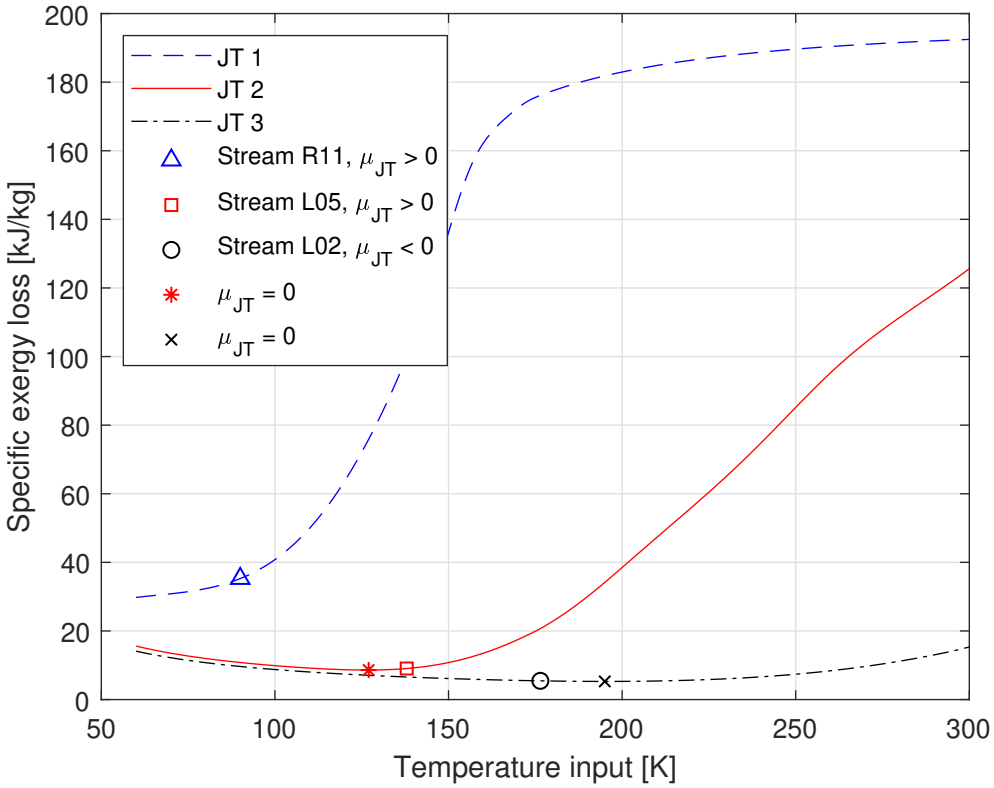

Figure 8.7: *Specific exergy loss as a function of temperature in to the throttling valves, for the different compositions, in the optimized 90 K SMR precooling cycle. The triangle, square, and circle indicates the specific exergy losses over the throttling valves for the optimized result.*

Phase separation of refrigerant mixtures does not produce any exergy loss, however, mixing of different refrigerant composition and stream temperatures does, which attributes to 5.1% of the total exergy loss. The exergy losses attributed mixing of different temperature stream are assumed to be minor for small temperature differences, at least for pure or identical molar component fractions. The majority seems to be caused by the chemical exergy losses, as different refrigerant compositions are mixed.

The improvable exergy losses in the SMR precooling cycle seem to be attributed to the

degree of phase separation. A reduced degree of separation, is indicated to improve the exergy efficiency, but has a high probability of refrigerant freeze-out. To find an optimal valid exergy efficiency and SEC, a thorough estimation of mixed refrigerant freeze-out probability is required, in order to create a good precooling cycle configuration.

Table 8.3: *Stream properties for the optimized SMR 90 K precooling cycle.*

Stream	**Temperature** $[K]$	**Pressure** $[bar]$	**Mass flow** $[\frac{kg}{s}]$	**Vapor fraction**
R01	301.1	5.3	31.615	1.000
R02	351.5	12.1	31.615	1.000
R03	303.2	12.1	31.615	1.000
R04	355.6	27.4	31.615	1.000
R05	303.2	27.4	31.615	0.846
R06	293.2	27.4	31.615	0.786
R07	293.2	27.4	21.015	1.000
R08	176.5	27.4	21.015	0.318
R09	176.5	27.4	5.370	1.000
R10	138.0	27.4	5.370	0.480
R11	90.0	27.4	5.370	0.097
R12	86.0	5.3	5.370	0.177
R13	132.7	5.3	5.370	0.956
R14	135.9	5.3	21.015	0.330
R15	170.3	5.3	21.015	0.587
R16	173.6	5.3	31.615	0.457
R17	275.1	5.3	31.615	0.993
L01	293.2	27.4	10.600	0.000
L02	176.5	27.4	10.600	0.000
L03	177.5	5.3	10.600	0.008
L04	176.5	27.4	15.645	0.000
L05	138.0	27.4	15.645	0.000
L06	135.6	5.3	15.645	0.046
F01	298.0	21.0	1.157	1.000
F02	293.2	21.0	1.157	1.000
F03	176.5	21.0	1.157	1.000
F04	138.0	21.0	1.157	1.000
F05	90.0	21.0	1.157	1.000

8.2 90 K precooled hydrogen Claude cycle

The overall exergy loss attributed to the 90 K precooled hydrogen Claude cycle account for 14087.2 kJ/s, which is approximately 80% of the total losses, in the hydrogen liquefaction process. The exergy losses from each component group are depicted in figure 8.8, where the majority of exergy losses is attributed to the heat exchangers, compressors, intercoolers, and turbines. The individual stream properties and exergy losses are presented in table 8.5 and 8.4, respectively, along with the exergy loss percentage attributed to each component. The two tables will be discussed interchangeably in the exergy analysis presented below.

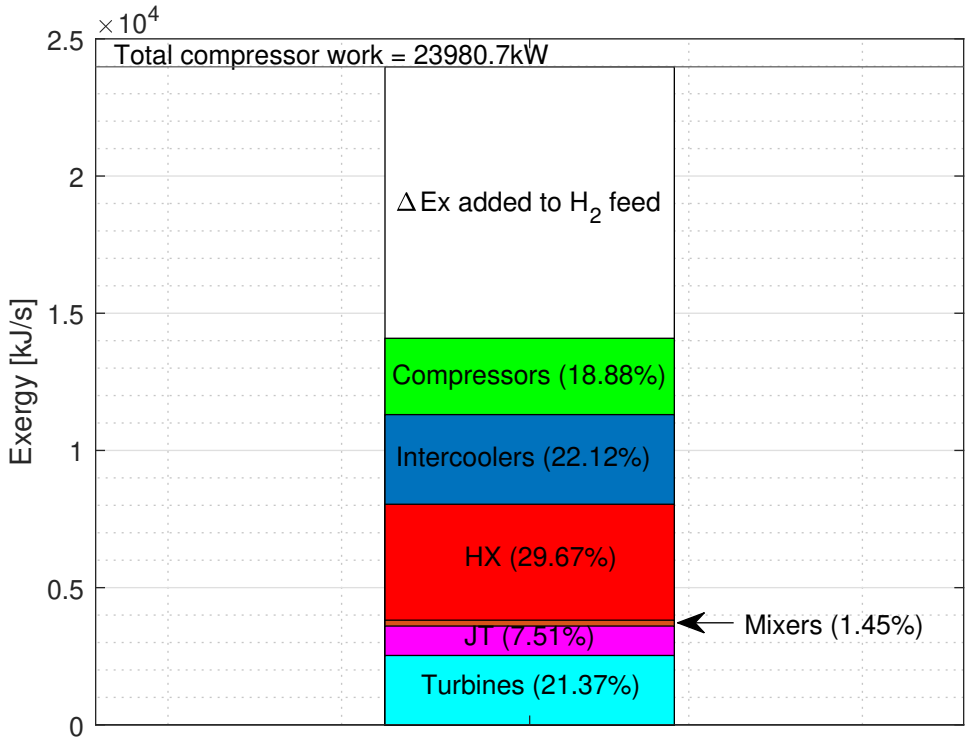

Figure 8.8: *Exergy losses for the component groups in the optimized 90 K precooled hydrogen Claude cycle.*

Table 8.4: *Exergy losses for each component of the optimized 90 K hydrogen Claude cycle.*

Component	**Exergy loss** $[\frac{kJ}{s}]$	**Exergy loss [%]**
Compressor 3	52.2	0.35
Compressor 4	52.2	0.35
Compressor 5	1336.6	9.07
Compressor 6	1340.7	9.10
Intercooler 3	38.7	0.26
Intercooler 4	44.7	0.30
Intercooler 5	1552.6	10.54
Intercooler 6	1630.8	11.07
HX 5	833.4	5.66
HX 6	132.5	0.90
HX 7	380.1	2.58
HX 8	1268.4	8.61
HX 9	1517.3	10.30
HX 10	93.3	0.63
Mixer 3	0.0	0.00
Mixer 4	211.4	1.43
Mixer 5	2.3	0.02
Splitter 1	0.0	0.00
Splitter 2	0.0	0.00
Splitter 3	0.0	0.00
JT 1.1	307.7	2.09
JT 1.2	764.5	5.43
Expander 1.1	180.1	1.22
Expander 1.2	179.4	1.22
Expander 1.3	178.9	1.21
Expander 2.1	398.0	2.70
Expander 2.2	395.9	2.69
Expander 3.1	599.2	4.07
Expander 3.2	596.6	4.05
Sum	14087.2	100

The compressors in the hydrogen Claude cycle are responsible for 18.88% of the exergy losses. The losses are significantly higher for compressor 5 and 6, than compressor 3 and

4, which is mostly related to the difference in refrigerant flow rate. However, the pressure ratio and input pressure will also affect the specific exergy losses as depicted in Figure 8.9, although the difference in input pressure is more or less negligible at lower pressures. As compressor 5 and 6 account for approximately 9% of the total losses, each, adding more compressors or shift compressor 4 over to the medium to the high-pressure side of mixer 1, could potentially decrease the total exergy losses over the compression train. By adding more compressors individually, the total exergy losses would increase due to the isentropic efficiency. With additional intercoolers, the total required compressor work would decrease due to less compression at higher temperatures, hence reduced losses. Also, the exergy loss for the intercoolers could be reduced to some extent, due to the non-linearity of the specific exergy losses, as depicted in figure 8.10.

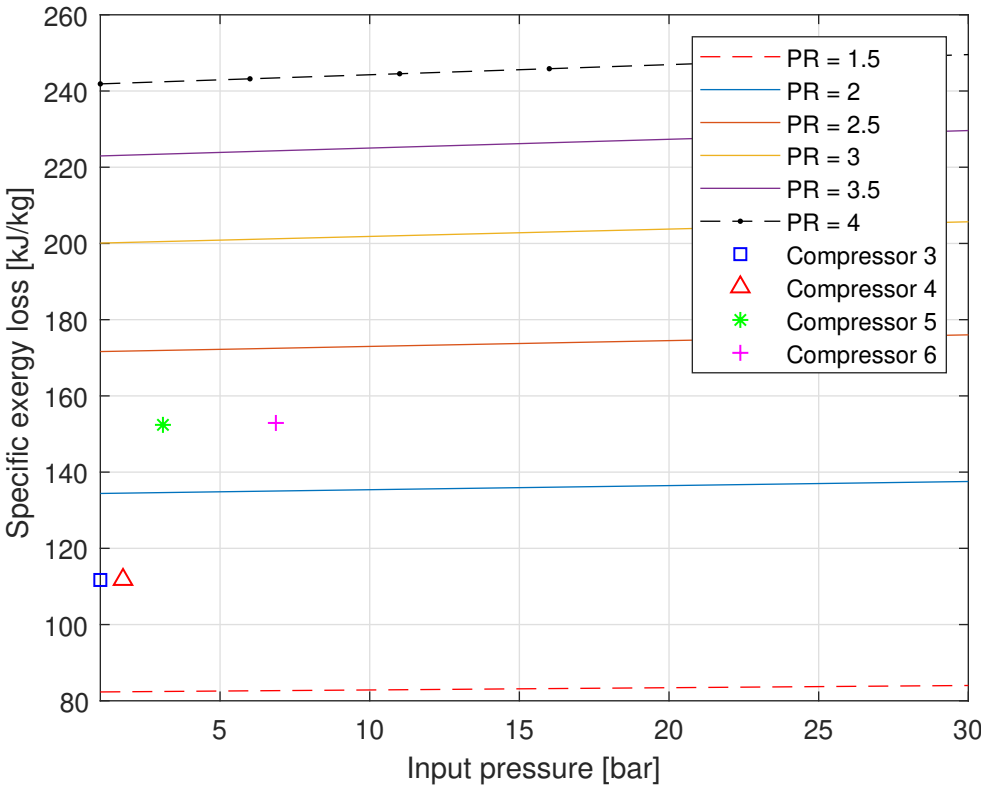

Figure 8.9: *Specific exergy losses for normal hydrogen compression as a function of input pressure, at different pressure ratios. Isentropic efficiency 85%.*

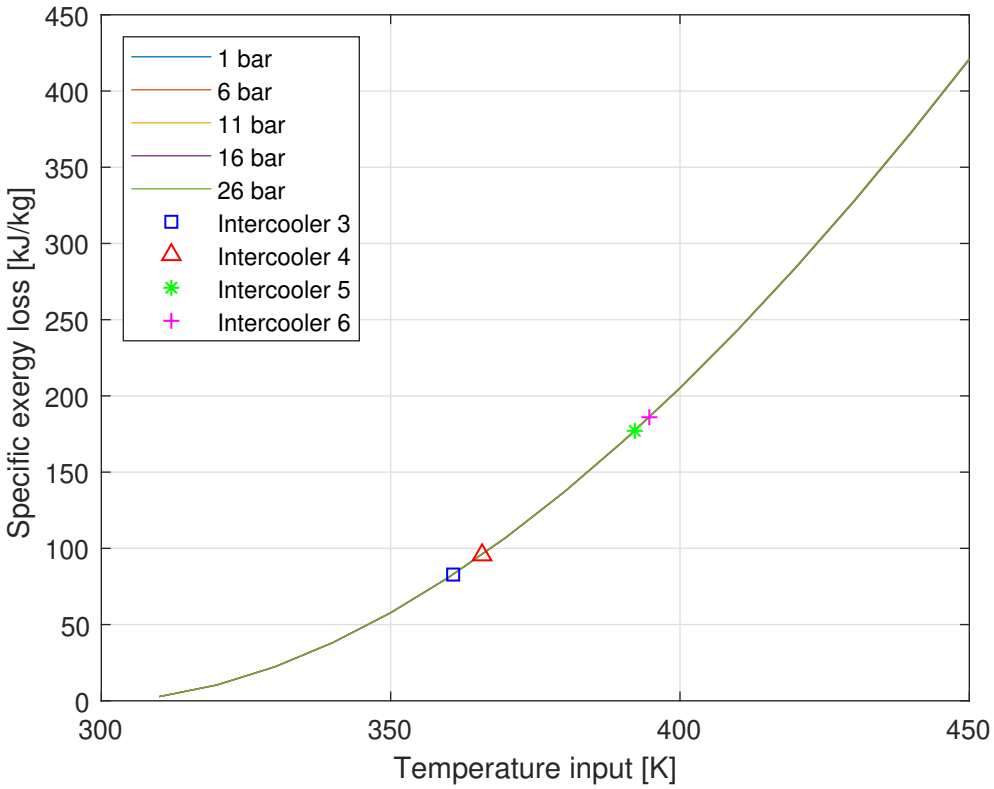

Figure 8.10: *Specific exergy losses for normal hydrogen intercooling as a function of input temperature, at different pressures.*

Figure 8.11 shows the hot- and cold-composite curve for all heat exchangers in the Claude cycle. From the figure, it is apparent that the majority ($\approx 83\%$) of the heat flow is attributed to HX 5, which is used to cool the high-pressure refrigerant stream to approximately match the precooling hydrogen feed. It is assumed that portions of the HX 5 exergy loss could be improved, if the precooling- and hydrogen Claude-cycle were integrated, as is commonly done in other research and existing plants. Also, it is expected that an integrated system could have a positive impact on other losses, in the precooling- and hydrogen Claude-cycle.

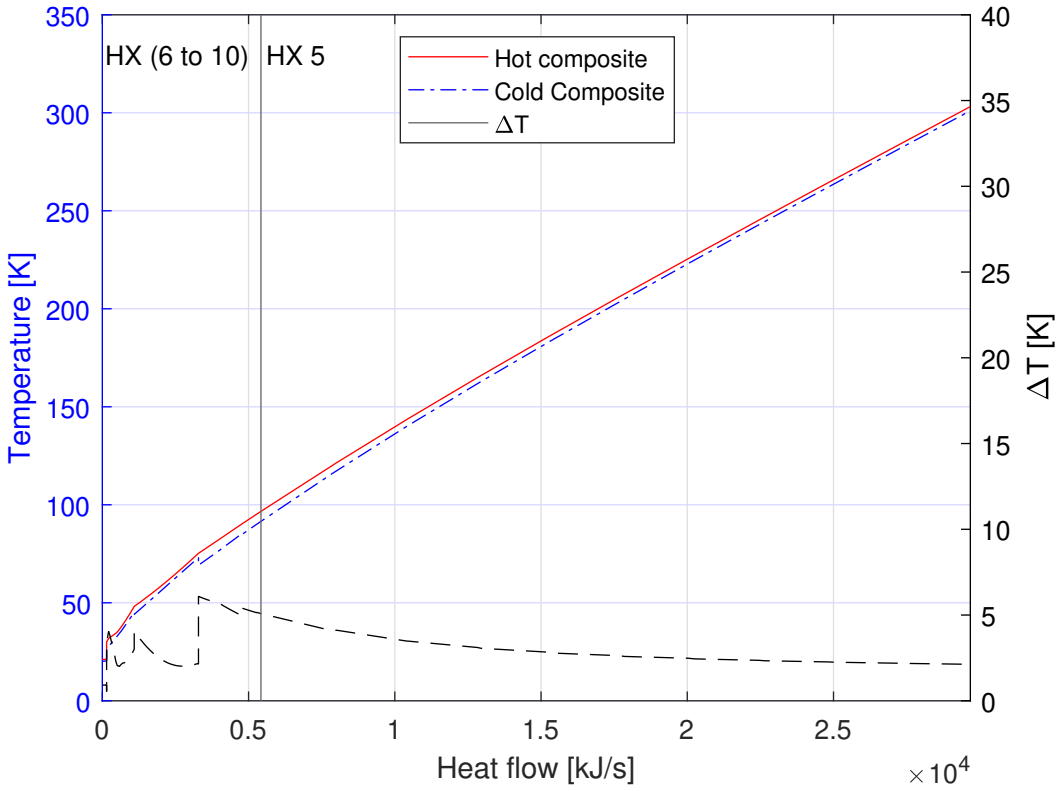

Figure 8.11: *Composite curves within the heat exchangers for the optimized 90 K precooled hydrogen Claude cycle.*

In total, heat exchanger 5 to 10 account for ≈ 29% of the total exergy losses in the Claude cycle. HX 8 and HX 9 alone account for ≈ 19%, where 10% is attributed to HX 9. The high exergy losses in HX 9 is assumed to be partially due to reaching saturated liquid at 32.9 K, and the variable equilibrium hydrogen heat capacity over the HX 9 temperature level, compared to the temperature span from HX 6 to HX 8 where the heat capacity increases more or less linearly in comparison. Some temperature discrepancy at the heat exchanger interfaces can be observed in figure 8.12, especially at HX 7/8, which is due to the temperature difference of the streams entering mixer 4.

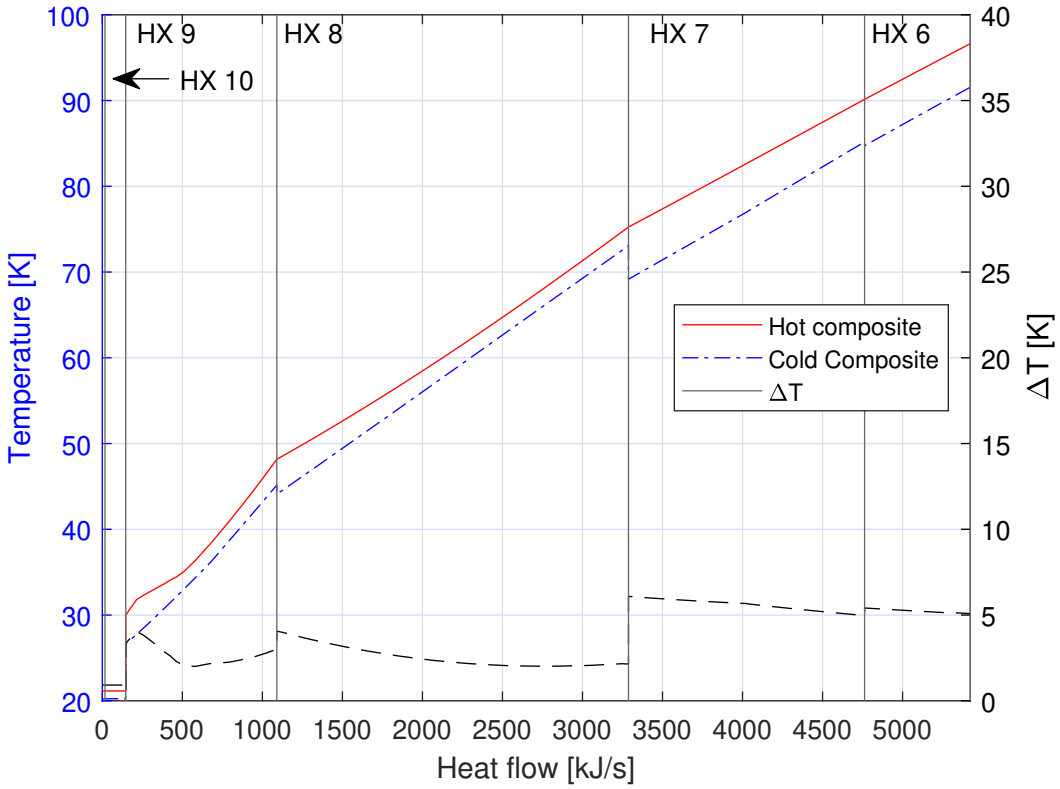

Figure 8.12: *Composite curves within heat exchangers 6 to 10, for the optimized 90 K precooled hydrogen Claude cycle.*

The temperature difference in mixer 4, can to some extent be seen in relation to the pressure reduction over the E1 expander train. All of the expanders are working in between a medium- and high-pressure-level. Obtaining an ideal medium pressure that would satisfy the cooling duty requirement for each temperature level, and reduce the temperature difference between the mixing streams, might be difficult with this Claude cycle configuration. By analyzing figure 8.13, a solution could be to split the compression train at an intermediate pressure, at ≈ 6.5 bar, in between the medium- to high-pressure-side, in order to reduce the pressure difference over the E1 expansion train. This could approximately equalize the stream temperatures entering mixer 4, and presumably lower the exergy losses over the E1 expanders, mixer 4, and HX 7. Extracting some of the refrigerant mass flow at an intermediate pressure would also reduce the compression work and intercooling duty at higher pressures, hence lower exergy losses. An idea could be to acquire each expansion train to its own pressure level, which could have a positive effect on the total exergy efficiency. However, changes in the configuration would most likely affect other parts of the cycle.

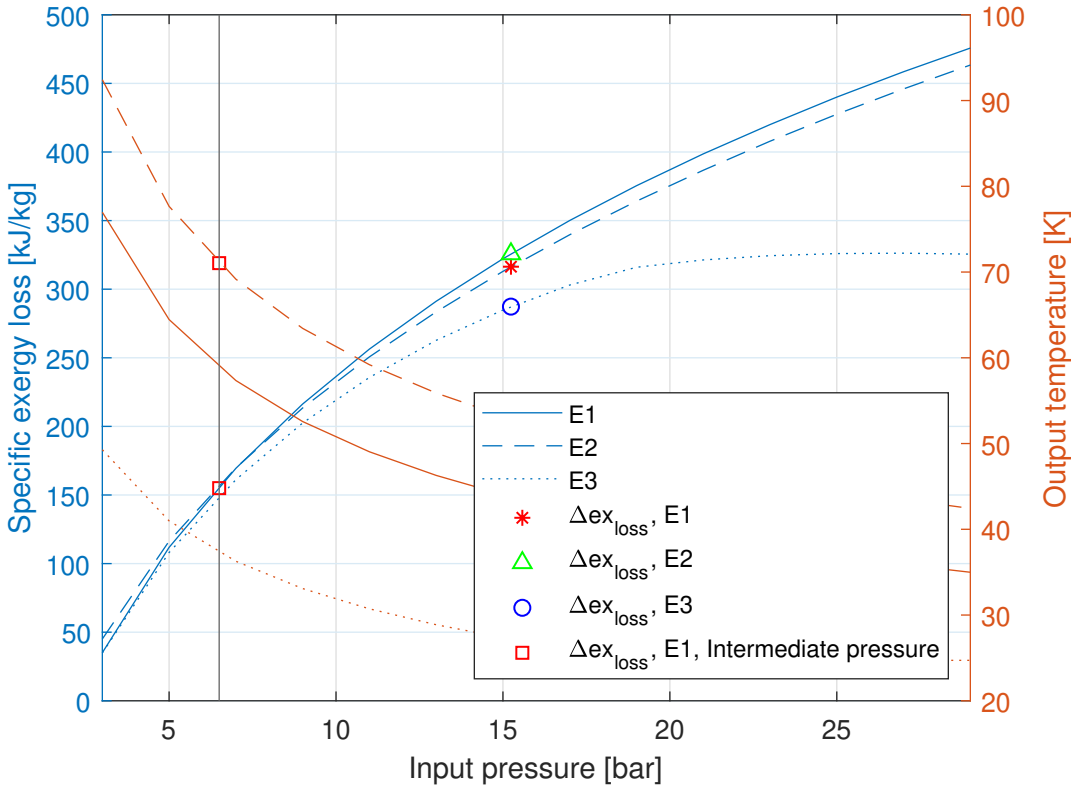

Figure 8.13: *Specific exergy losses and temperature decrease over the hydrogen expanders as a function of input pressure with output pressure of 3.092 bar. (with 100% turbine energy recovery) The squares indicates the possible reduction in specific exergy loss and temperature output, if E1 operated at a ≈ 6.5 bar to 3.092 bar pressure level.*

The exergy losses attributed to the turbine expander train E1, E2, and E3, account for 3.65%, 5.39%, and 8.11%, respectfully, where the difference in exergy losses is mostly related to the refrigerant mass flow. However, by looking at figure 8.14, some of the specific exergy losses are related to the input temperature and the number of expanders in series. As most of the exergy losses are in the E3 expander train, shifting one of the expanders in E1 to E3 could potentially decrease the total exergy losses attributed to the expanders.

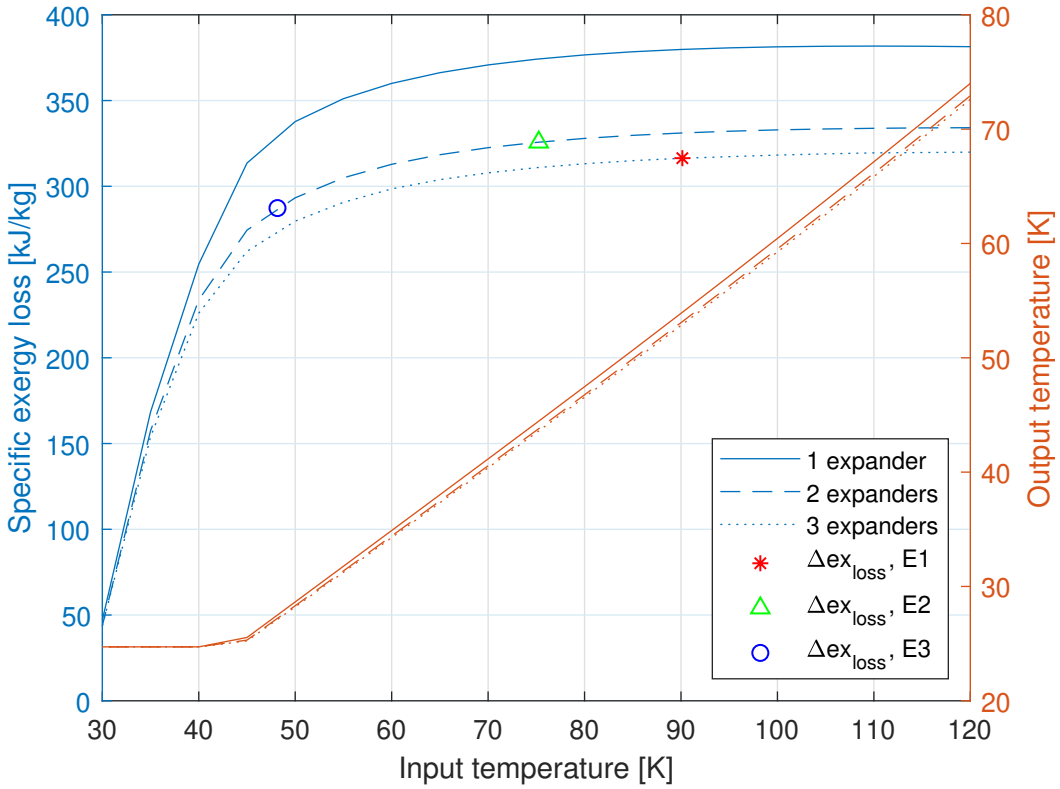

Figure 8.14: *Specific exergy losses and temperature decrease of normal hydrogen expansion from 15.24 bar to 3.092 bar as a function of input temperature, with 1, 2 and 3 turbo expanders in series. (with 100% turbine energy recovery)*

JT 1.1 and JT 1.2 accounts for 2.09% and 5.43% of the total exergy losses. The specific exergy losses depicted in figure 8.15 show similar losses. The temperature into the two throttling valves is equal but has a slight deviation between the vapor fraction exiting the valves, which is caused by the difference between the two pressure levels. Utilizing a dense phase expander, could reduce the specific exergy losses from approximately 660 kJ/kg to 100 kJ/kg, if the turbine work is recovered, as indicated by the vertical lines in figure 8.15. With dense phase expanders, the vapor fraction can be reduced from approximately 0.3 to 0.2, the exact value is dependent on the input pressure.

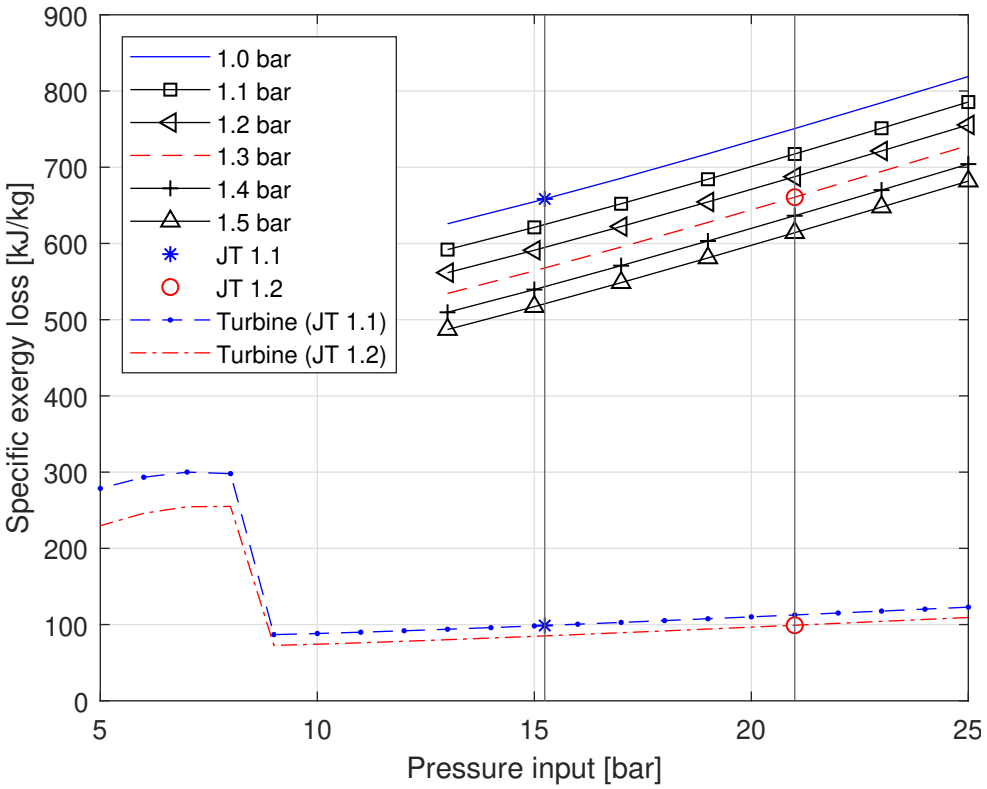

Figure 8.15: *Specific exergy losses for throttling hydrogen as a function of input pressure, at different outlet pressure. And the potential exergy loss if the JT valves was replaced by dense phase expander.*

Table 8.5: *Stream properties for the optimized 90 K precooled hydrogen Claude cycle.*

Stream	Temperature $[K]$	Pressure $[bar]$	Mass flow $[\frac{kg}{s}]$	Vapor fraction
R18	96.6	15.2	8.768	1.000
R19	90.1	15.2	8.768	1.000
R20	90.1	15.2	7.066	1.000
R21	75.3	15.2	7.066	1.000
R22	75.3	15.2	4.629	1.000
R23	48.2	15.2	4.629	1.000
R24	48.2	15.2	0.467	1.000
R25	30.0	15.2	0.467	0.000
R26	20.2	1.0	0.467	0.307
R27	20.6	1.0	0.467	1.000
R28	35.9	1.0	0.467	1.000
R29	72.5	1.0	0.467	1.000
R30	76.8	1.0	0.467	1.000
R31	91.6	1.0	0.467	1.000
RE1	45.2	3.1	4.162	1.000
RE2	44.7	3.1	6.599	1.000
RE3	73.1	3.1	6.599	1.000
RE4	69.0	3.1	8.300	1.000
RE5	85.2	3.1	8.300	1.000
RE6	91.6	3.1	8.300	1.000
RE7	301.1	3.1	8.300	1.000
E1.1	90.1	15.2	1.701	1.000
E1.2	75.7	9.0	1.701	1.000
E1.3	63.4	5.3	1.701	1.000
E1.4	52.9	3.1	1.701	1.000
E2.1	75.3	15.2	2.437	1.000
E2.2	57.5	6.9	2.437	1.000
E2.3	43.8	3.1	2.437	1.000
E3.1	48.2	15.2	4.162	1.000
E3.2	36.2	6.9	4.162	1.000
E3.3	27.2	3.1	4.162	1.000

Stream	**Temperature** $[K]$	**Pressure** $[bar]$	**Mass flow** $[\frac{kg}{s}]$	**Vapor fraction**
C01	299.0	1.0	0.467	1.000
C02	360.8	1.8	0.467	1.000
C03	303.2	1.8	0.467	1.000
C04	365.8	3.1	0.467	1.000
C05	303.2	3.1	0.467	1.000
C06	301.2	3.1	8.768	1.000
C07	392.2	6.9	8.768	1.000
C08	303.2	6.9	8.768	1.000
C09	394.7	15.2	8.768	1.000
C10	303.2	15.2	8.768	1.000
F03/5	90.0	21.0	1.157	1.000
F06	90.1	21.0	1.157	1.000
F07	75.3	21.0	1.157	1.000
F08	48.2	21.0	1.157	1.000
F09	30.0	21.0	1.157	0.000
F10	21.2	1.3	1.157	0.287
F11	21.2	1.3	1.157	0.000

8.3 The effect of equilibrium hydrogen estimation

Optimization of the 90 K precooled hydrogen Claude cycle was performed with the continuous hydrogen equilibrium model, depicted as specific heat capacity in figure 8.16. The figure compares the continuous equilibrium hydrogen model to the two-stage model utilized as the results.

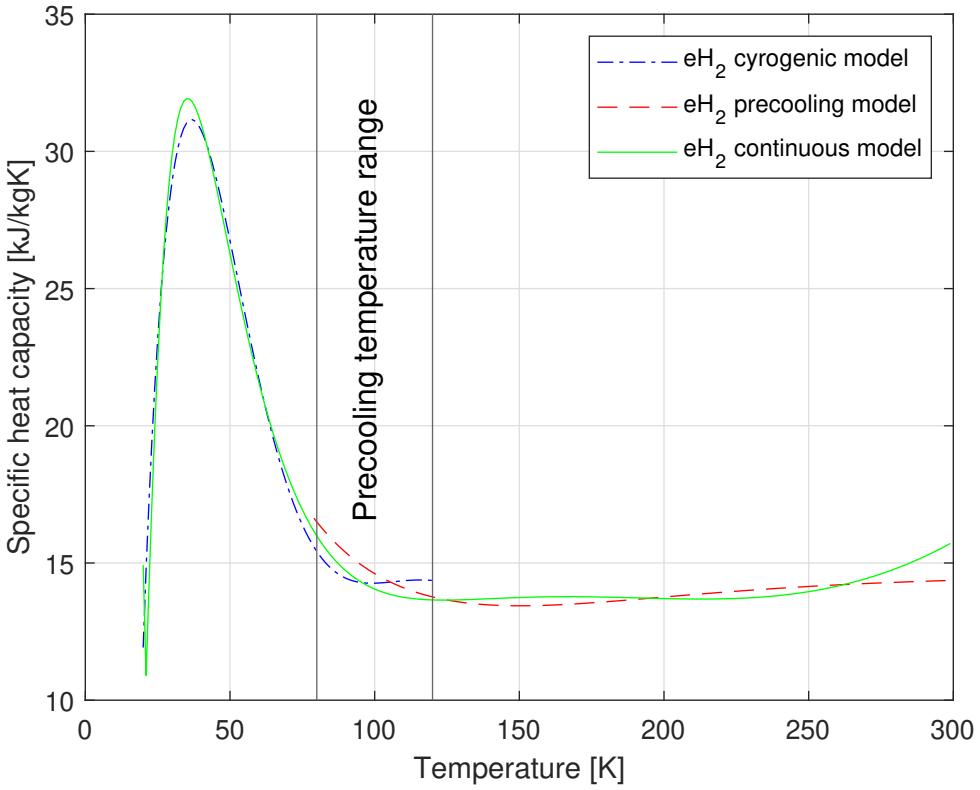

Figure 8.16: *Show the difference in specific heat capacity between a continuous equilibrium hydrogen model, and the two models utilized in as the results.*

The accuracy of the model-fitting for specific-enthalpy and -entropy for the continuous model is depicted in figure 8.17 and 8.18, along with the calculated and utilized regressed cryogenic equilibrium hydrogen model. Although the deviation and slope gradient between the cryogenic and continuous model is assumed to be relatively small, the impact on the process efficiency is found to be high. The optimized SEC for the continuous equilibrium model was 5.08 kWh/kg_{LH_2} which is significant. Compared to the 90 K Claude cycle (cryogenic model) result, at 5.76 kWh/kg_{LH_2}. The MTA in all heat exchangers (HX 6 to HX 9) resulted to be more or less equal to 2 K for the continuous model. But it is worth noting that testing the continuous equilibrium hydrogen model in the validation model/configuration, in figure 4.7, showed reduced exothermic (T≈7 K lower) effect of the ortho-para hydrogen conversion

compared to the utilized cryogenic equilibrium model.

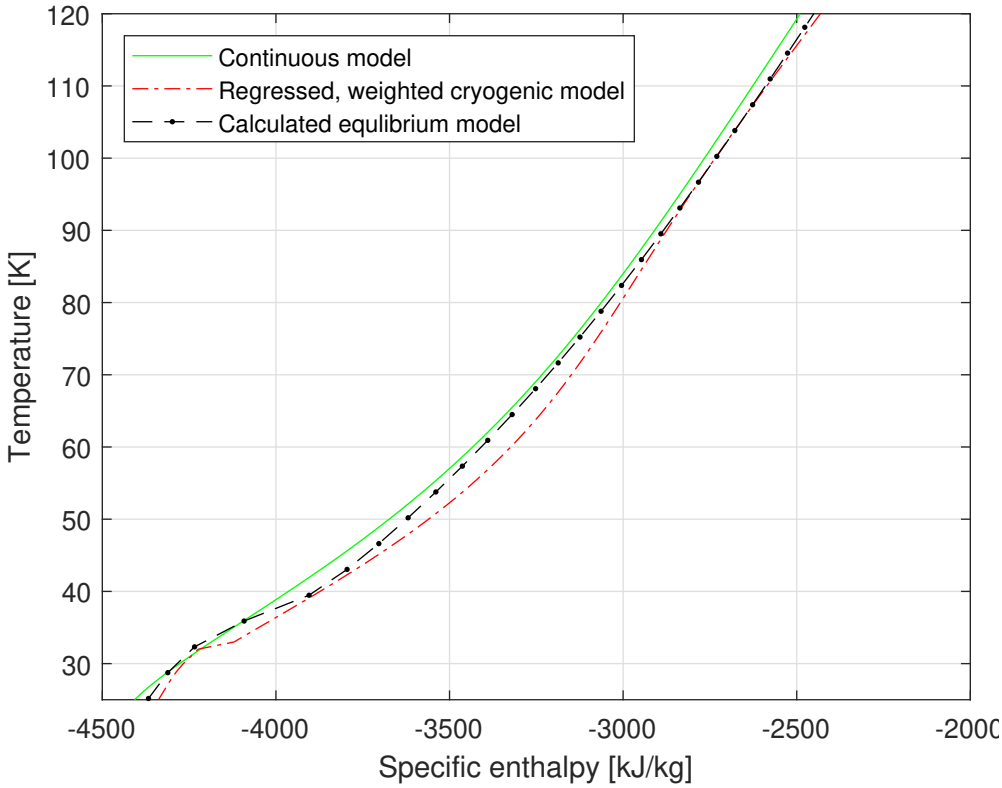

Figure 8.17: *Show the difference between a continuous equilibrium hydrogen model and the two utilized models.*

A solution to solve the inaccuracy of the model-fitting could be to create several regressed equilibrium hydrogen models, each dedicated to the higher- and lower optimization boundary temperature span in each heat exchanger, as the accuracy of regression is improved if the temperature span is shorter.

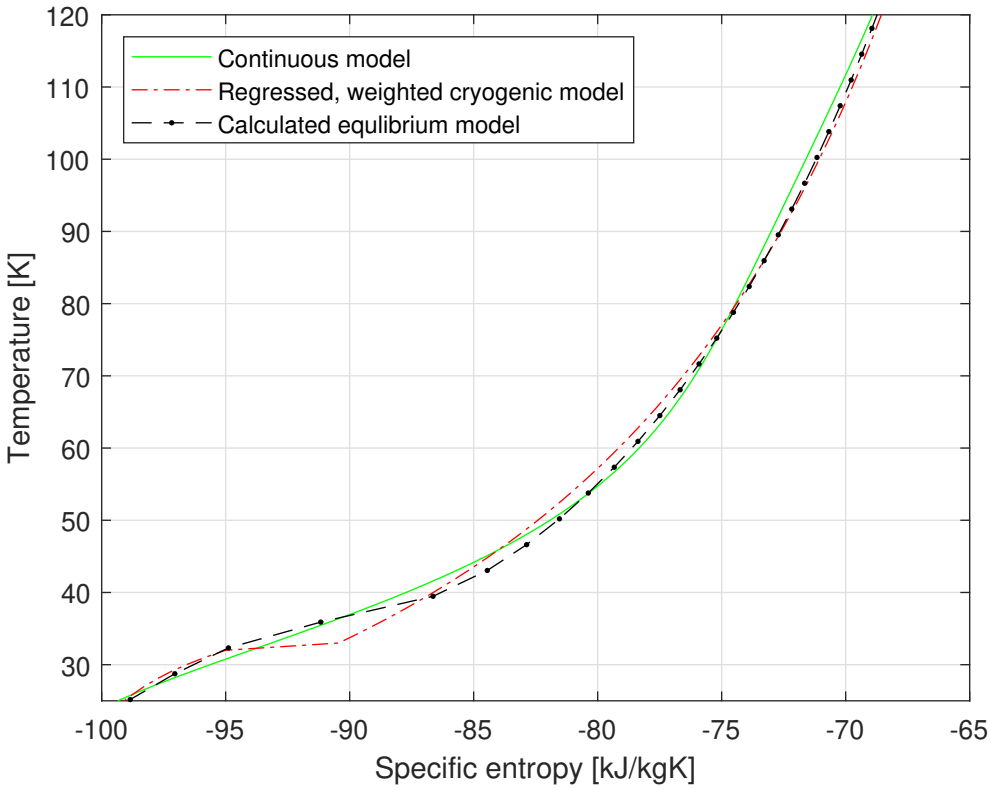

Figure 8.18: *Show the difference between a continuous equilibrium hydrogen model and the two utilized models.*

Although improved results are indicated, this only suggests that the accuracy of the estimated equilibrium hydrogen model and model-fitting is of crucial importance, in order to simulate decent efficiency prediction for the hydrogen liquefaction process. Also, as previously stated comparing different optimization results must be taken with caution due to the result's potential to deviate from an ideal optimized solution.

Conclusion

Precooling is an important part of an efficient hydrogen liquefaction process. State-of-the-art research has improved the SEC and exergy efficiency for conceptualized MR precooled hydrogen liquefaction processes by a factor over 2, relative to commercialized plants with liquid nitrogen vaporization precooling.

The optimized results found in this thesis has indicated that the optimal MR precooling temperature in a hydrogen Claude liquefaction process is located around 90 K. The results showed an optimized 90 K MR precooling cycle SEC and exergy efficiency at 1.27 kWh/kg_{LH_2} and 42.77%, respectively. For the 90 K hydrogen Claude cycle, an SEC and exergy efficiency was found at 5.76 kWh/kg_{LH_2} and 35.62%. The total process equates to 6.52 kWh/kg_{LH_2} and 37.00%, if 100% of the turbine work is recycled in the compressors.

There are found indications that the 90 K SMR precooler is subjected to some freeze-out possibility. However, the temperature gap between the individual refrigerant freezing points, and the MR cycle lowest temperature is assumed to be acceptable. Utilizing a method for estimating the freezing point of a multi-component refrigerant mixture, could potentially improve the efficiency as the SMR precooler has been found to be slightly more efficient for a lower degree of separation. Analyzing the specific exergy losses attributed to the SMR cycle has indicated that there are few optimization improvements for the case 2 configuration. Hence, possible efficiency improvements seem to be related to the design and manufacturing of compressors, intercoolers, and heat exchangers as these have the largest contribution to the exergy losses.

80% of the total exergy losses are found in the hydrogen Claude cycle. The exergy analysis indicates that there are several refrigerant cycle configuration modifications that could improve the efficiency of the process. However, the accuracy of the regressed equilibrium hydrogen model has been found to have a significant impact on the optimized process efficiency, hence the validity of the suggested improvements. For the future of hydrogen liquefaction simulation and optimization, standardization of an equilibrium hydrogen model is important in order have a decent prediction of the exothermic effect of the ortho-para hydrogen conversion, and to validate and compare result to different research.

9 Further Work

In order to validate the viability of the estimated freeze-out probability related to the SMR precooling cycles, a scientific method for freezing point estimation should be emphasized in further work.

By utilizing the current equilibrium hydrogen model, there have been indicated several possible improvements for further work. With the current equipment count: one of the intercooled compressors at the low- to medium-pressure side should be switched over to the medium- to high-pressure side, in order to reduce the pressure ratio, hence decrease the specific exergy losses on the medium- to high-pressure side. Also, one of the expander in expander train E1 should be shifted to the E3 expander train. Integration of the precooling- and cryogenic cooling-cycle might have a positive effect on the exergy losses in the total liquefaction process. There seem to be a potential for a decrease in exergy losses related to if each expander train is attributed an individual input pressure. Dense phase expanders are indicated to have a significant positive effect on exergy loss reduction, and further investigation on dense phase expanders viability should be performed. Due to the low precooling temperature resolution, there is most likely an optimized solution in proximity to 90 K, which has slightly higher efficiency.

By increasing the number of compressors and intercoolers, the specific exergy losses can be decreases. However, this will lead to an increased number of equipment, and higher cost for an actual process. Cost is important in order to determine the viability of a project, therefore cost optimization related to the number and size of refrigeration cycle equipment should be assessed in further work.

The liquefaction process efficiency is found to be highly dependent on the estimated equilibrium hydrogen model accuracy, Therefore special attention should be attributed to the regression and model-fitting method in further work.

References

[1] European Commission. *A hydrogen strategy for a climate-neutral Europe*. Accessed: 05.13.2021. 2020.

[2] Hydrogen Council. *Hydrogen decarbonization pathways*. https://hydrogencouncil.com/wp-content/uploads/2021/01/Hydrogen-Council-Report_Decarbonization-Pathways_Part-1-Lifecycle-Assessment.pdf. Accessed: 02.01.2021. 2021.

[3] Office of energy efficiency & renewable energy. *Hydrogen Storage*. https://www.energy.gov/eere/fuelcells/hydrogen-storage. Accessed: 09.06.2021.

[4] *The Engineering ToolBox*. https://www.engineeringtoolbox.com/. Accessed: 05.14.2021.

[5] François Cardarelli. "Materials Handbook: A concise desktop rederence". In: *third edition* (2018). Accessed: 04.02.2021, pp. 1589–1598. DOI: https://doi.org/10.1007/978-3-319-38925-7. URL: https://link.springer.com/content/pdf/10.1007/978-3-319-38925-7.pdf.

[6] European Commission. *Hydrogen*. https://ec.europa.eu/energy/topics/energy-system-integration/hydrogen_en. Accessed: 02.01.2021. 2020.

[7] NVE. *Vannkraft*. https://www.nve.no/energiforsyning/kraftproduksjon/vannkraft/?ref=mainmenu. Accessed: 05.14.2021. 2021.

[8] Enova. *Etablering av vindkraft i Norge*. https://www.enova.no/upload_images/B4D72DED9E864DA6B38DA939AFAEA4A7.pdf. Accessed: 05.13.2021. 2013.

[9] NVE. *Vindkraft*. https://www.nve.no/energiforsyning/kraftproduksjon/vindkraft/?ref=mainmenu. Accessed: 05.13.2021. 2021.

[10] Christina Benjaminsen. *Dette må du vite om hydrogen*. https://www.sintef.no/siste-nytt/2019/dette-ma-du-vite-om-hydrogen/. Accessed: 05.14.2021. 2019.

[11] Equinor. *Fremtidens havvind er flytende*. https://www.equinor.com/no/what-we-do/floating-wind.html. Accessed: 05.13.2021. 2021.

[12] CNBC. *Denmark to trial green hydrogen production using offshore wind turbines*. https://www.cnbc.com/2021/01/20/denmark-to-trial-green-hydrogen-production-using-offshore-wind-power.html. Accessed: 05.14.2021. 2021.

[13] Energy Voice. *'World first' floating green hydrogen project coming to Aberdeen*. https://www.energyvoice.com/renewables-energy-transition/267583/world-first-floating-green-hydrogen-project-aberdeen/. Accessed: 05.14.2021. 2020.

[14] Iain Staffell et al. "The role of hydrogen and fuel cells in the global energy system". In: *Energy Environ. Sci.* 12 (2 2019). Accessed: 04.02.2021, pp. 463–491. DOI: 10.1039/C8EE01157E. URL: http://dx.doi.org/10.1039/C8EE01157E.

[15] Norled. *Norled velger Westcon i Ølen for bygging av verdens første hydrogen-ferje*. https://www.norled.no/nyheter/norled-velger-westcon-i-olen-for-bygging-av-verdens-forste-hydrogen-ferje/. Accessed: 05.14.2021. 2019.

[16] Airbus. *Airbus reveals new zero-emission concept aircraft*. https://www.airbus.com/newsroom/press-releases/en/2020/09/airbus-reveals-new-zeroemission-concept-aircraft.html. Accessed: 05.14.2021. 2020.

[17] Yuki Ishimoto et al. "Large-scale production and transport of hydrogen from Norway to Europe and Japan: Value chain analysis and comparison of liquid hydrogen and ammonia as energy carriers". In: *International Journal of Hydrogen Energy* 45.58 (2020). Accessed: 05.14.2021, pp. 32865–32883. ISSN: 0360-3199. DOI: https://doi.org/10.1016/j.ijhydene.2020.09.017. URL: https://www.sciencedirect.com/science/article/pii/S036031992033384X.

[18] Songwut Krasae-in, Jacob H. Stang, and Petter Neksa. "Development of large-scale hydrogen liquefaction processes from 1898 to 2009". In: *International Journal of Hydrogen Energy* 35.10 (2010). Accessed: 02.03.2021, pp. 4524–4533. ISSN: 0360-3199. DOI: https://doi.org/10.1016/j.ijhydene.2010.02.109. URL: https://www.sciencedirect.com/science/article/pii/S0360319910004118.

[19] Majid Aasadnia and Mehdi Mehrpooya. "Large-scale liquid hydrogen production methods and approaches: A review". In: *Applied Energy* 212 (2018). Accessed: 02.03.2021, pp. 57–83. ISSN: 0306-2619. DOI: https://doi.org/10.1016/j.apenergy.2017.12.033. URL: https://www.sciencedirect.com/science/article/pii/S0306261917317488.

[20] U. Cardella et al. "Process optimization for large-scale hydrogen liquefaction". In: *International Journal of Hydrogen Energy* 42.17 (2017). Accessed: 03.17.2021, pp. 12339–12354. ISSN: 0360-3199. DOI: https://doi.org/10.1016/j.ijhydene.2017.03.167. URL: https://www.sciencedirect.com/science/article/pii/S0360319917311746.

[21] Songwut Krasae-in. "Optimal operation of a large-scale liquid hydrogen plant utilizing mixed fluid refrigeration system". In: *International Journal of Hydrogen Energy* 39.13 (2014). Accessed: 03.18.2021, pp. 7015–7029. ISSN: 0360-3199. DOI: https://doi.org/10.1016/j.ijhydene.2014.02.046. URL: https://www.sciencedirect.com/science/article/pii/S0360319914004066.

[22] Majid Asadnia and Mehdi Mehrpooya. "A novel hydrogen liquefaction process configuration with combined mixed refrigerant systems". In: *International Journal of Hydrogen Energy* 42.23 (2017). Accessed: 03.19.2021, pp. 15564–15585. ISSN: 0360-3199. DOI: https://doi.org/10.1016/j.ijhydene.2017.04.260. URL: https://www.sciencedirect.com/science/article/pii/S0360319917317469.

[23] David Berstad, Geir Skaugen, and Øivind Wilhelmsen. "Dissecting the exergy balance of a hydrogen liquefier: Analysis of a scaled-up claude hydrogen liquefier with mixed refrigerant pre-cooling". In: *International Journal of Hydrogen Energy* 46.11 (2021). Accessed: 01.28.2021, pp. 8014–8029. ISSN: 0360-3199. DOI: https://doi.org/10.1016/j.ijhydene.2020.09.188. URL: https://www.sciencedirect.com/science/article/pii/S0360319920336284.

[24] U. Cardella, L. Decker, and H. Klein. "Roadmap to economically viable hydrogen liquefaction". In: *International Journal of Hydrogen Energy* 42.19 (2017). Accessed: 05.15.2021, pp. 13329–13338. ISSN: 0360-3199. DOI: https://doi.org/10.1016/j.ijhydene.2017.01.068. URL: https://www.sciencedirect.com/science/article/pii/S0360319917302355.

[25] H. T Walnum et al. *Principles for the liquefaction of hydrogen with emphasis on precooling processes*. https://www.idealhy.eu/uploads/documents/IDEALHY_Cryogenics_2012_Precooling.pdf. Accessed: 04.04.2021. 2012.

[26] Adam Jones, Grant Johnson, and Costain Natural Resources. *A NEW PROCESS FOR IMPROVED LIQUEFACTION EFFICIENCY*. https://www.costain.com/media/13018/gpae_improved-liquifaction_sept-2013.pdf. Accessed: 05.24.2021. 2013.

[27] Gianluca Valenti, Ennio Macchi, and Samuele Brioschi. "The influence of the thermodynamic model of equilibrium-hydrogen on the simulation of its liquefaction". In: *International Journal of Hydrogen Energy* 37.14 (2012). Accessed: 03.09.2021, pp. 10779–10788. ISSN: 0360-3199. DOI: https://doi.org/10.1016/j.ijhydene.2012.04.050. URL: https://www.sciencedirect.com/science/article/pii/S0360319912009044.

[28] Jacob Leachman. *Why equilibrium hydrogen doesn't exist*. https://hydrogen.wsu.edu/2015/06/22/why-equilibrium-hydrogen-doesnt-exist/. Accessed: 03.09.2021. 2015.

[29] Olga Anatol'evna Boeva et al. "Low-temperature ortho–para hydrogen conversion catalyzed by gold nanoparticles: Particle size does not affect the rate". In: *International Journal of Hydrogen Energy* 42.36 (2017). Accessed: 04.02.2021, pp. 22897–22902. ISSN:

0360-3199. DOI: https://doi.org/10.1016/j.ijhydene.2017.07.187. URL: https://www.sciencedirect.com/science/article/pii/S0360319917330239.

[30] Aline Léon. "Hydrogen Technology". In: (2008). Accessed: 03.22.2021, pp. 81–128. ISSN: 978-3-540-79027-3. DOI: https://doi.org/10.1007/978-3-540-69925-5_3. URL: https://doi.org/10.1007/978-3-540-69925-5_3.

[31] G. Venkatarathnam and K. D. Timmerhaus. *Cryogenic mixed refrigerant processes.* . Springer 2008, pp 199-205.

[32] Federico Capra, Francesco Magli, and Manuele Gatti. "Biomethane liquefaction: A systematic comparative analysis of refrigeration technologies". In: *Applied Thermal Engineering* 158 (2019). Accessed: 04.02.2021, p. 113815. ISSN: 1359-4311. DOI: https://doi.org/10.1016/j.applthermaleng.2019.113815. URL: https://www.sciencedirect.com/science/article/pii/S1359431119302212.

[33] Bahram Ghorbani et al. "Cascade refrigeration systems in integrated cryogenic natural gas process (natural gas liquids (NGL), liquefied natural gas (LNG) and nitrogen rejection unit (NRU))". In: *Energy* 115 (2016). Accessed: 03.25.2021, pp. 88–106. ISSN: 0360-5442. DOI: https://doi.org/10.1016/j.energy.2016.09.005. URL: https://www.sciencedirect.com/science/article/pii/S0360544216312440.

[34] Guo-guang Ma et al. "A study on the use of dual mixed refrigerant in a cascade dual mixed refrigerant cycle". In: *Advances in Mechanical Engineering* 9 (June 2017). Accessed: 03.25.2021, p. 168781401771058. DOI: 10.1177/1687814017710582.

[35] T. Morosuk et al. "Evaluation of the PRICO liquefaction process using exergy-based methods". In: *Journal of Natural Gas Science and Engineering* 27 (2015). Accessed: 03.25.2021, pp. 23–31. ISSN: 1875-5100. DOI: https://doi.org/10.1016/j.jngse.2015.02.007. URL: https://www.sciencedirect.com/science/article/pii/S1875510015000657.

[36] Danahe Marmolejo-Correa and Truls Gundersen. "A comparison of exergy efficiency definitions with focus on low temperature processes". In: *Energy* 44.1 (2012). Accessed: 05.04.2021, pp. 477–489. ISSN: 0360-5442. DOI: https://doi.org/10.1016/j.energy.2012.06.001. URL: https://www.sciencedirect.com/science/article/pii/S0360544212004513.

[37] Mengyu Wang, Rajab Khalilpour, and Ali Abbas. "Thermodynamic and economic optimization of LNG mixed refrigerant processes". In: *Energy Conversion and Management* 88 (2014). Accessed: 03.24.2021, pp. 947–961. ISSN: 0196-8904. DOI: https:

//doi.org/10.1016/j.enconman.2014.09.007. URL: https://www.sciencedirect.com/science/article/pii/S0196890414007997.

[38] Inkyu Lee, Jinwoo Park, and Il Moon. "Key Issues and Challenges on the Liquefied Natural Gas (LNG) Value Chain: A Review from the Process Systems Engineering Point-of-View". In: *Industrial Engineering Chemistry Research* 57 (Dec. 2017). Accessed: 05.05.2021. DOI: 10.1021/acs.iecr.7b03899.

[39] Jisung Lee et al. "Design of high efficiency mixed refrigerant Joule–Thomson refrigerator for cooling HTS cable". In: *Cryogenics* 51.7 (2011). Accessed: 04.09.2021, pp. 408–414. ISSN: 0011-2275. DOI: https://doi.org/10.1016/j.cryogenics.2011.04.007. URL: https://www.sciencedirect.com/science/article/pii/S0011227511000956.

[40] G. Hwang and S. Jeong. *Estimation of freezing point of hydrocarbon and hydrofluorocarbon mixtures for mixed refrigerant JT cryocooler*. https://aip.scitation.org/doi/pdf/10.1063/1.3422466. Accessed: 04.09.2021. 2010.

[41] Michael J Moran et al. *Principles of engineering thermodynamics*. Wiley, eighth edition. 2015.

[42] M. Bracha et al. "Large-scale hydrogen liquefaction in Germany". In: *International Journal of Hydrogen Energy* 19.1 (1994). Accessed: 02.02.2021, pp. 53–59. ISSN: 0360-3199. DOI: https://doi.org/10.1016/0360-3199(94)90177-5. URL: https://www.sciencedirect.com/science/article/pii/0360319994901775.

[43] Songwut Krasae-in et al. "Simulation and experiment of a hydrogen liquefaction test rig using a multi-component refrigerant refrigeration system". In: *International Journal of Hydrogen Energy* 36.1 (2011). Accessed: 03.18.2021, pp. 907–919. ISSN: 0360-3199. DOI: https://doi.org/10.1016/j.ijhydene.2010.09.005. URL: https://www.sciencedirect.com/science/article/pii/S0360319910017921.

[44] Jørgen Eckroll. "Concepts for Large Scale Hydrogen Liquefaction Plants". In: (2017). Accessed: 06.06.2021. URL: https://ntnuopen.ntnu.no/ntnu-xmlui/bitstream/handle/11250/2454901/17110_FULLTEXT.pdf?sequence=1.

[45] G E McIntosh. *Applications of ortho-para hydrogen catalyst*. https://iopscience.iop.org/article/10.1088/1757-899X/101/1/012079/pdf. Accessed: 19.05.2021. 2015.

Appendix

A Enthalpy and entropy, nH_2 and pH_2

Table A.1: *Entropy and enthalpy for normal- and parahydrogen obtained in refprop.*

Enthalpy $[\frac{kJ}{kg}]$		**Entropy** $[\frac{kJ}{kgK}]$		**Temperature [K]**
nH_2	pH_2	nH_2	pH_2	
-4335.5	-4853.6	-88.1	-91.5	14.4
-4308.1	-4826.6	-86.5	-89.9	18.1
-4275.6	-4794.5	-84.9	-88.3	21.7
-4236.7	-4755.5	-83.3	-86.7	25.4
-4188.5	-4706.9	-81.6	-85.0	29.0
-4122.2	-4640.2	-79.5	-82.9	32.6
-3980.8	-4501.4	-75.9	-79.3	36.3
-3826.6	-4347.5	-71.5	-74.9	39.9
-3746.3	-4267.6	-69.5	-72.9	43.5
-3683.9	-4205.5	-68.1	-71.5	47.2
-3629.0	-4150.7	-67.0	-70.4	50.8
-3578.3	-4099.9	-66.0	-69.4	54.5
-3530.1	-4051.4	-65.1	-68.5	58.1
-3483.8	-4004.3	-64.4	-67.7	61.7
-3438.7	-3958.1	-63.7	-67.0	65.4
-3394.5	-3912.3	-63.0	-66.3	69.0
-3350.9	-3866.5	-62.4	-65.7	72.6
-3307.7	-3820.7	-61.8	-65.1	76.3
-3264.8	-3774.4	-61.3	-64.5	79.9
-3222.1	-3727.6	-60.7	-63.9	83.6
-3179.4	-3680.1	-60.2	-63.4	87.2
-3136.8	-3631.8	-59.8	-62.8	90.8
-3094.1	-3582.7	-59.3	-62.3	94.5
-3051.2	-3532.6	-58.9	-61.8	98.1

Enthalpy $[\frac{kJ}{kg}]$		**Entropy** $[\frac{kJ}{kgK}]$		**Temperature [K]**
nH_2	pH_2	nH_2	pH_2	
-3008.2	-3481.6	-58.4	-61.3	101.7
-2965.0	-3429.6	-58.0	-60.8	105.4
-2921.5	-3376.7	-57.6	-60.3	109.0
-2877.8	-3322.9	-57.2	-59.8	112.7
-2833.9	-3268.2	-56.8	-59.4	116.3
-2789.6	-3212.7	-56.5	-58.9	119.9
-2745.1	-3156.5	-56.1	-58.4	123.6
-2700.3	-3099.5	-55.8	-58.0	127.2
-2655.2	-3041.9	-55.4	-57.5	130.8
-2609.8	-2983.8	-55.1	-57.1	134.5
-2564.2	-2925.1	-54.7	-56.7	138.1
-2518.2	-2866.1	-54.4	-56.3	141.8
-2471.9	-2806.7	-54.1	-55.8	145.4
-2425.4	-2747.0	-53.8	-55.4	149.0
-2378.6	-2687.1	-53.5	-55.0	152.7
-2331.6	-2627.0	-53.2	-54.7	156.3
-2284.3	-2566.8	-52.9	-54.3	159.9
-2236.7	-2506.6	-52.6	-53.9	163.6
-2188.9	-2446.3	-52.3	-53.5	167.2
-2140.9	-2386.1	-52.0	-53.2	170.9
-2092.6	-2325.9	-51.7	-52.8	174.5
-2044.1	-2265.8	-51.5	-52.5	178.1
-1995.4	-2205.9	-51.2	-52.2	181.8
-1946.6	-2146.1	-50.9	-51.8	185.4
-1897.5	-2086.5	-50.7	-51.5	189.0
-1848.2	-2027.0	-50.4	-51.2	192.7
-1798.7	-1967.7	-50.2	-50.9	196.3
-1749.1	-1908.7	-49.9	-50.6	200.0
-1699.3	-1849.8	-49.7	-50.3	203.6
-1649.4	-1791.2	-49.4	-50.0	207.2
-1599.3	-1732.8	-49.2	-49.7	210.9

Enthalpy $[\frac{kJ}{kg}]$		**Entropy** $[\frac{kJ}{kgK}]$		**Temperature [K]**
nH_2	pH_2	nH_2	pH_2	
-1549.0	-1674.6	-48.9	-49.5	214.5
-1498.6	-1616.7	-48.7	-49.2	218.1
-1448.1	-1559.0	-48.5	-48.9	221.8
-1397.5	-1501.5	-48.3	-48.7	225.4
-1346.7	-1444.2	-48.0	-48.4	229.1
-1295.8	-1387.2	-47.8	-48.2	232.7
-1244.8	-1330.3	-47.6	-47.9	236.3
-1193.7	-1273.7	-47.4	-47.7	240.0
-1142.5	-1217.2	-47.2	-47.5	243.6
-1091.2	-1160.9	-47.0	-47.2	247.2
-1039.9	-1104.9	-46.8	-47.0	250.9
-988.4	-1049.0	-46.6	-46.8	254.5
-936.8	-993.3	-46.4	-46.6	258.2
-885.2	-937.7	-46.2	-46.4	261.8
-833.5	-882.3	-46.0	-46.1	265.4
-781.7	-827.1	-45.8	-45.9	269.1
-729.9	-772.0	-45.6	-45.7	272.7
-678.0	-717.0	-45.4	-45.5	276.3
-626.0	-662.2	-45.2	-45.3	280.0
-574.0	-607.4	-45.0	-45.1	283.6
-522.0	-552.8	-44.8	-44.9	287.3
-469.8	-498.4	-44.7	-44.8	290.9
-417.7	-444.0	-44.5	-44.6	294.5
-365.5	-389.7	-44.3	-44.4	298.2
-313.2	-335.5	-44.1	-44.2	301.8

B Enthalpy and entropy, eH_2

Table B.1: *Specific- enthalpy and entropy for equilibrium hydrogen at temperature T, calculated with equation 4.6 and 4.7 for enthalpy and entropy, respectfully.*

Enthalpy $[\frac{kJ}{kg}]$	**Entropy** $[\frac{kJ}{kgK}]$	**Temperature [K]**
eH_2	eH_2	
-4853.5	-91.5	14.4
-4826.7	-89.9	18.0
-4793.6	-88.3	21.6
-4751.2	-86.7	25.2
-4695.5	-84.9	28.7
-4618.5	-82.7	32.3
-4475.9	-79.0	35.9
-4288.7	-74.5	39.5
-4179.2	-72.3	43.0
-4087.7	-70.7	46.6
-4003.4	-69.4	50.2
-3923.5	-68.2	53.8
-3847.2	-67.1	57.3
-3774.0	-66.2	60.9
-3703.8	-65.3	64.5
-3636.3	-64.5	68.1
-3571.2	-63.7	71.6
-3508.5	-63.0	75.2
-3447.7	-62.3	78.8
-3388.8	-61.7	82.4
-3331.4	-61.1	85.9
-3275.4	-60.5	89.5
-3220.7	-60.0	93.1
-3167.1	-59.5	96.7
-3114.3	-59.0	100.2
-3062.4	-58.5	103.8
-3011.2	-58.0	107.4

Enthalpy $[\frac{kJ}{kg}]$	**Entropy** $[\frac{kJ}{kgK}]$	**Temperature [K]**
eH_2	eH_2	
-2960.6	-57.6	111.0
-2910.5	-57.2	114.5
-2860.9	-56.8	118.1
-2811.6	-56.4	121.7
-2762.7	-56.0	125.3
-2714.0	-55.6	128.8
-2665.5	-55.2	132.4
-2617.1	-54.9	136.0
-2568.9	-54.5	139.6
-2520.8	-54.2	143.1
-2472.7	-53.9	146.7
-2424.7	-53.5	150.3
-2376.6	-53.2	153.9
-2328.5	-52.9	157.4
-2280.4	-52.6	161.0
-2232.3	-52.3	164.6
-2184.0	-52.0	168.2
-2135.7	-51.8	171.7
-2087.4	-51.5	175.3
-2038.9	-51.2	178.9
-1990.3	-50.9	182.5
-1941.6	-50.7	186.0
-1892.8	-50.4	189.6
-1843.9	-50.2	193.2
-1794.9	-49.9	196.8
-1745.8	-49.7	200.3
-1696.5	-49.4	203.9
-1647.2	-49.2	207.5
-1597.7	-48.9	211.1
-1548.1	-48.7	214.6
-1498.5	-48.5	218.2

Enthalpy $[\frac{kJ}{kg}]$	**Entropy** $[\frac{kJ}{kgK}]$	**Temperature [K]**
eH_2	eH_2	
-1448.7	-48.3	221.8
-1398.8	-48.0	225.4
-1348.8	-47.8	228.9
-1298.7	-47.6	232.5
-1248.5	-47.4	236.1
-1198.2	-47.2	239.7
-1147.9	-47.0	243.2
-1097.4	-46.8	246.8
-1046.9	-46.6	250.4
-996.3	-46.4	254.0
-945.6	-46.2	257.5
-894.9	-46.0	261.1
-844.1	-45.8	264.7
-793.2	-45.6	268.3
-742.2	-45.4	271.8
-691.2	-45.2	275.4
-640.2	-45.0	279.0
-589.1	-44.8	282.6
-537.9	-44.7	286.1
-486.7	-44.5	289.7
-435.4	-44.3	293.3
-384.1	-44.1	296.9